FACULTY
OF MECHANICAL
ENGINEERING
CTU IN PRAGUE

Department of Automotive, Combustion Engine and Railway Engineering

Study of the physical parameters influence on the measurement of the head-form to bonnet impact

Studie vlivu fyzikálních parametrů na chybu měření nárazu hlavového impaktoru na kapotu vozidla

MASTER'S THESIS
2020

Bc. Jakub Ryška

Study program:	Mechanical Engineering
Branch of study:	Transportation, Aerospace and Handling Technology
Thesis Advisor:	Ing. Michal Vašíček, Ph.D.
Submitter:	Porsche Engineering Services s.r.o.

MASTER'S THESIS ASSIGNMENT

I. Personal and study details

Student's name: **Ryška Jakub** Personal ID number: **460015**

Faculty / Institute: **Faculty of Mechanical Engineering**

Department / Institute: **Department of Automotive, Combustion Engine and Railway Engineering**

Study program: **Mechanical Engineering**

Branch of study: **Transportation, Aerospace and Handling Technology**

II. Master's thesis details

Master's thesis title in English:

Study of the physical parameters influence on the measurement of the head-form to bonnet impact

Master's thesis title in Czech:

Studie vlivu fyzikálních parametrů na chybu měření nárazu hlavového impaktoru na kapotu vozidla

Guidelines:

1) Create a research of a valid standards for the tests of pedestrian head protection in the event of a car crash
2) Perform a sensitivity study of the FE parameters of the head-form model
3) Optimize the design of the original equipment for tests of the sensitivity of the head-form (box)
4) Build a computational model of a new box and optimize its behavior by means of simulations of the impact test with a head-form
5) Prepare measurements for the purpose of test and research of the physical parameters influence on the test result in cooperation with the testing laboratory.

Bibliography / sources:

Name and workplace of master's thesis supervisor:

Ing. Michal Vašíček, Ph.D., Department of Automotive, Combustion Engine and Railway Engineering, FME

Name and workplace of second master's thesis supervisor or consultant:

Date of master's thesis assignment: **29.04.2020** Deadline for master's thesis submission: **15.07.2020**

Assignment valid until: _____

Ing. Michal Vašíček, Ph.D.	doc. Ing. Oldřich Vítek, Ph.D.	prof. Ing. Michael Valášek, DrSc.
Supervisor's signature	Head of department's signature	Dean's signature

III. Assignment receipt

The student acknowledges that the master's thesis is an individual work. The student must produce his thesis without the assistance of others, with the exception of provided consultations. Within the master's thesis, the author must state the names of consultants and include a list of references.

Date of assignment receipt	Student's signature

Annotation Record

Author's name:	Jakub Ryška
Master thesis name:	Study of the physical parameters influence on the measurement of the head-form to bonnet impact
Master Thesis name in Czech:	Studie vlivu fyzikálních parametrů na chybu měření nárazu hlavového impaktoru na kapotu vozidla
Scope of Thesis:	123 pages 92 figures 11 tables
Academic year:	2019/2020
Department:	12120 Department of Automotive, Combustion Engine and Railway Engineering
Study program:	N2301 Mechanical Engineering
Thesis Advisor:	Ing. Michal Vašíček, Ph.D.
Key words:	passive safety, pedestrian protection, headform impactors. crash tests, FEM simulations, head injury criterion, BOX testing device, pedestrian protection throwing device
Klíčová slova:	pasivní bezpečnost, ochrana chodců, hlavové impaktory, crash testy, simulace pomocí MKP, kritérium poranění hlavy, BOX testovací zařízení, vrhací zařízení

Abstract

This Thesis discusses the problematics of the impact tests in relation to a category of pedestrian protection. The main reason behind the elaboration of this Thesis was a special phenomenon occurring during the tests with headform impactors in various laboratories.

The first part of this work describes in detail all issues related to the preparation, conduct and evaluation of tests. The second part contains the description of the performed and evaluated simulations of the certification drop test and also simulations of the test substituting the impact of the headform to the bonnet, for which a special test device was developed and manufactured. The last chapter describes the modernization procedure of the throwing device used in the laboratories of the *Department of Automotive, Combustion Engine and Railway Engineering*. New headform impactors were developed and subsequently manufactured as a part of this innovation. These headform impactors will be further used for internal experiments concerning the pedestrian protection.

This Thesis was prepared under the patronage of *Porsche Engineering Services s.r.o.*

Abstrakt

Tato diplomová práce se zabývá problematikou nárazových zkoušek spadající do kategorie ochrany chodců. Hlavním tématem pro vypracování byl zvláštní jev vyskytující se při testech s hlavovými impaktory v různých laboratořích.

V první části této práce jsou podrobně popsány všechny záležitosti týkající se přípravy, průběhu a vyhodnocení zkoušek. Ve druhé části jsou provedeny a vyhodnoceny simulace nárazové certifikační zkoušky a simulace náhrady nárazu impaktoru na kapotu vozidla, pro kterou bylo vyvinuto a vyrobeno speciální zkušební zařízení. V poslední kapitole je sepsán postup modernizace vrhacího zařízení v laboratořích *Ústavu automobilů, spalovacích motorů a kolejových vozidel*. V rámci této renovace byly vyvinuty a následně vyrobeny nové hlavové impaktory, které se budou používat pro interní nárazové zkoušky.

Tato diplomová práce byla vypracována pod záštitou *Porsche Engineering Services s.r.o.*

Author statement for postgraduate Thesis

I declare that the presented work was developed independently and that I have listed all sources of information used within it in accordance with the methodical instructions for observing the ethical principles in the preparation of university Thesis.

In Prague, date: 13th July 2020

…….....

(Signature)

Čestné prohlášení

Čestně prohlašuji, že tato diplomová práce byla vypracovaná samostatně a že jsem uvedl všechny zdroje informací, které v ní jsou použity, v souladu s metodickými pokyny pro dodržování etických principů při přípravě závěrečné práce.

V Praze dne: 13. 7. 2020

…….....

(Podpis autora)

Acknowledgements

First of all, I would sincerely give thanks to my supervisor Ing. Michal Vašíček, Ph.D. for his valuable advice, professional guidance and for the time he had sacrificed in helping me to succeed.

My professional career started at Porsche Engineering and complementation of this Thesis would not be possible without my colleagues and friends from there. My most sincere gratitude and appreciation goes to Ing. Karel Vedral and Dipl.-Ing. Michael Soellner for giving me the guidance and providing me with the necessary help. A special thanks also belong to Ing. Lukáš Kosek for his assistance with 3D printing of some parts necessary for a throwing device modernisation.

I would also like give thanks to my colleagues from the CTU Faculty of Mechanical Engineering, specifically to Ing. Vojtěch Klír, Ph.D. for his vital role in the throwing device modernisation and Ing. Marin Kovář for his data acquisition software.

Finally, I would like to give special thanks to my family and the closest ones for their support, patience and understanding.

Contents

1 Introduction

The issue of the vehicle passive safety is probably as old as motor vehicle itself. History of the vehicle safety probably began after the first fatal accident caused by a motor vehicle in 1869 [1].

At the beginning of the 20th century, the importance of safety began to grow together with the expansion of the passenger vehicles and also the freight transport. The progress in the passive safety has been recorded after the group of US vehicle manufacturers led by GM and Ford introduced technological innovations increasing the passive safety, thus reducing the road accidents mortality. An important milestone in future developments was the performance of the first barrier crash test in 1934 [2] by General Motors.

After World War II, the road vehicle safety was influenced by a newly established *World Forum for Vehicle Harmonization and Regulation*, under the patronage of the *United Nations*. This organization is developing and harmonizing the regulations concerning for example environmental protection, fuel combustion, exhaust emission and of course – pedestrian protection. The first document issued by this organization was in the 1958 the *Agreement Concerning the Adoption of Harmonized Technical United Nations Regulations for Wheeled Vehicles.* This agreement established a legal framework in which the participating countries undertake to apply a common set of technical regulations and protocols relating to the approval of motor vehicles. The Czech Republic became a signatory of this agreement on the 1st January 1993 as the eighth country in the world. For the purposes of this Thesis we would mainly concentrate on with the Regulation No. 127 [3], which stipulates the uniform regulations for the approval of motor vehicles in regard of pedestrian safety. By law the pedestrian protection tests form the essential part of vehicle type approval.

Over the past year has the importance of pedestrian protection tests increased due to the development concerning some previously hidden problems regarding the specifics of the pedestrians. The first issue is the growing share of SUV within the vehicle market. The second problem is the increase in the average age of the population. [4] From the combination of these factors it is evident, that the importance of the pedestrian protection will be increasing. For that purposes it is required that a suitable testing device and equipment, described in detail further on in this Thesis, shall be developed. One of the chapters deals with modernisation of CTU testing device in Juliska laboratory that will be used for in-house pedestrian protection experiments. New headform impactors will need to be manufactured for testing purposes. Their design is presented in the last chapter of this Thesis.

The basics for experiment verification are FEM simulations, which are the core of the Thesis. These simulations were developed in the ANSA pre-processor, computed by using an LS-DYNA software and evaluated in META post-processor. The headform impactors were designed in CATIA V5 software.

1.1 Accidents statistics

1.1.1 Czech Republic

According to the statistics of the Police of the Czech Republic[1] [5], there were 104 764 road traffic accidents in the territory of the Czech Republic in the year 2018[2]. The results of these collisions were 25 215 mild injuries, 2 465 severe injuries, and 565 fatalities It means that the year 2018 had the third-lowest number of fatalities as a result of a traffic accident in the history of police statistics. On average, there were 1.55 fatalities per day what means that life has died out on every 15.5 hours as a consequence of a traffic accident. The estimated material damage caused by these accidents is quantified as 6.5 billion CZK (approximately 254.2 million €).

Further on we can determine from the statistics the most vulnerable road user on-road communications. In overall, the highest share in the number of casualties of the road accidents are drivers of the passenger cars followed by the second most vulnerable group – pedestrians. As shown in Table 1, the proportion of killed pedestrians in the year 2018 was 20 %. Every 5th person killed due to road accident was a pedestrian. The third most vulnerable group are the passengers of passenger cars.

The subsequent table gives an overview of the injured and killed persons in the year 2018 in Czech Republic sort by their relation to the incident:

Table 1 – Overview of injuries and death share regarding traffic accidents in the Czech Republic [5]

Class	Injuries	[%]	Deaths	[%]
Driver of passenger car	9 946	35.93	202	35.75
Pedestrians	3 341	12.07	113	20.00
Passenger in a passenger car	5 486	19.82	98	17.35
Motorcyclist	2 447	8.84	86	15.22
Cyclist	3 590	12.97	38	6.73

The total number of pedestrian-related accidents is 4 113. This number consists of 3 532 accidents of adult pedestrians and 779 collisions involved a child pedestrians. This resulted in total death count of 122 persons which accounts for 21.59 % of the total deaths on-road in the Czech Republic in the year 2018

According to Table 1, the total number of pedestrians killed is less than the number stated in the previous paragraph. The root of this phenomena has origin in the pedestrian-involved traffic accidents, where not only the pedestrian but also some other participant of the traffic was killed

For the improvement of pedestrian protection, it is important to concentrate on the causes and circumstances of pedestrian-involved accidents. As illustrated in Figure 1-1 the most frequent cause of death of pedestrians was when the driver was not fully engaged in the driving of the vehicle. [5] [6] 31 pedestrians were killed as a result of this negligence, in other words, 27% of total pedestrian casualties. The second reason of pedestrian fatalities are pedestrians themselves. The Police statistic shows that the most common pedestrian

[1] The data from the Police of Czech Republic are within 24 hours after the accident
[2] Unfortunately, the statistics from year 2019 were sill not being issued by the Police at the time of writing this Thesis.

behaviour causing the traffic accident was a sudden entry into the roadway combined with in accurate estimation of the approaching vehicle distance and speed. The third largest contributor to lethal traffic accidents involving pedestrian-has a source in not giving way to the pedestrian on a marked pedestrian crossing. This fact correlates with locations where the accidents happened. From the total sum of 113 killed pedestrians in the Czech Republic, 68 % of all casualties were killed in built-up areas. [6]

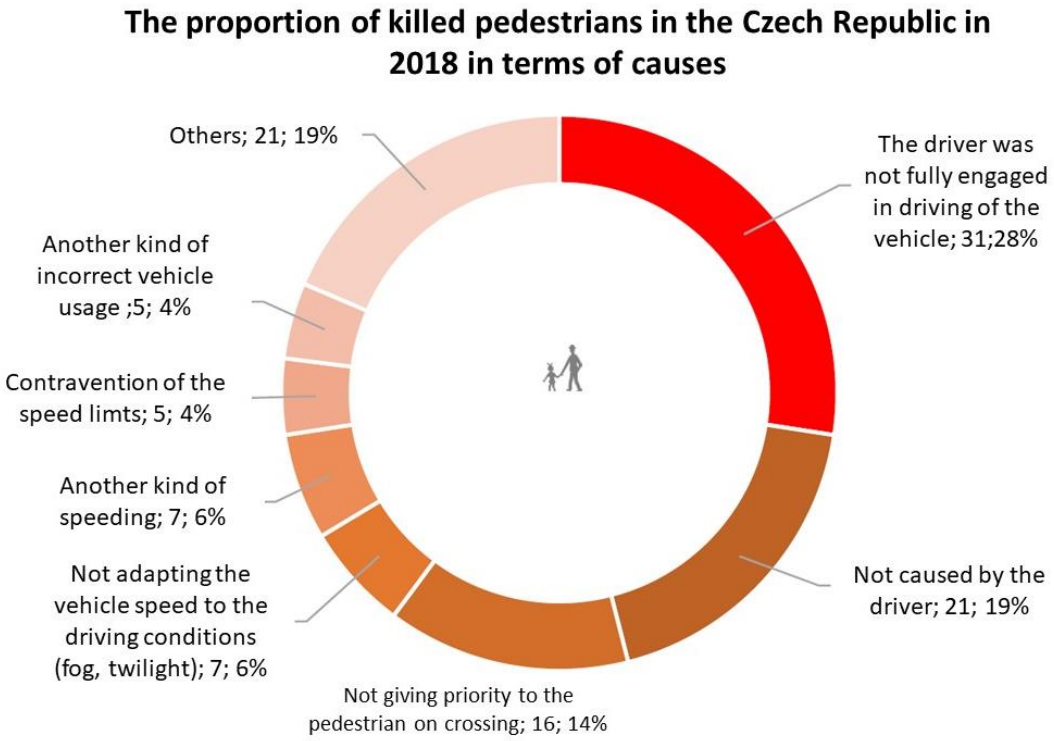

Figure 1-1 – The proportion of killed pedestrian sorted by the causes. [6]

Although the total sum of road accident casualties in the Czech Republic has dropped by 62 % and the number of pedestrians killed by 74 % since the year 1994, the Czech Republic is still lagging behind the European average [5]. By the latest report from the BESIP [6], an independent department of the *Czech Republic Ministry of Transport*, with reference to the IRTAD[3] (*International Traffic Safety Data and Analysis Group*) [7] the fatality rate of pedestrian is 13 causalities per million population. In comparison, the average fatality rate of the other European countries is9 fatalities per million population.

This difference in fatality rate with the rest of Europe was the reason to establish The *National Strategic Road Safety Plan 2011-2020* (NSRSP) [8], which is supposed to lower the fatality rate to the EU average. This strategy specifically aims for 60 % reduction in fatalities and 40 % reduction in number of persons seriously injured by the year 2020 compared to the year 2009. Despite initial satisfactory progress, the interim targets of the NSRSP between the years 2014 and 2018 were not fulfilled.

[3] Data taken from year 2018

As it is apparent from Figure 1-2 the long-term trend of pedestrian fatalities in the Czech Republic has notably decreasing character. The number of annual pedestrian deaths fell by 28 %. [6] between the years 2009 and 2018. The record low number was recorded in the year of 2017 when the pedestrian fatalities dropped to 101 followed by an increase to 113 the next year. New measures are needed to stimulate progress to achieve the target for 2020.

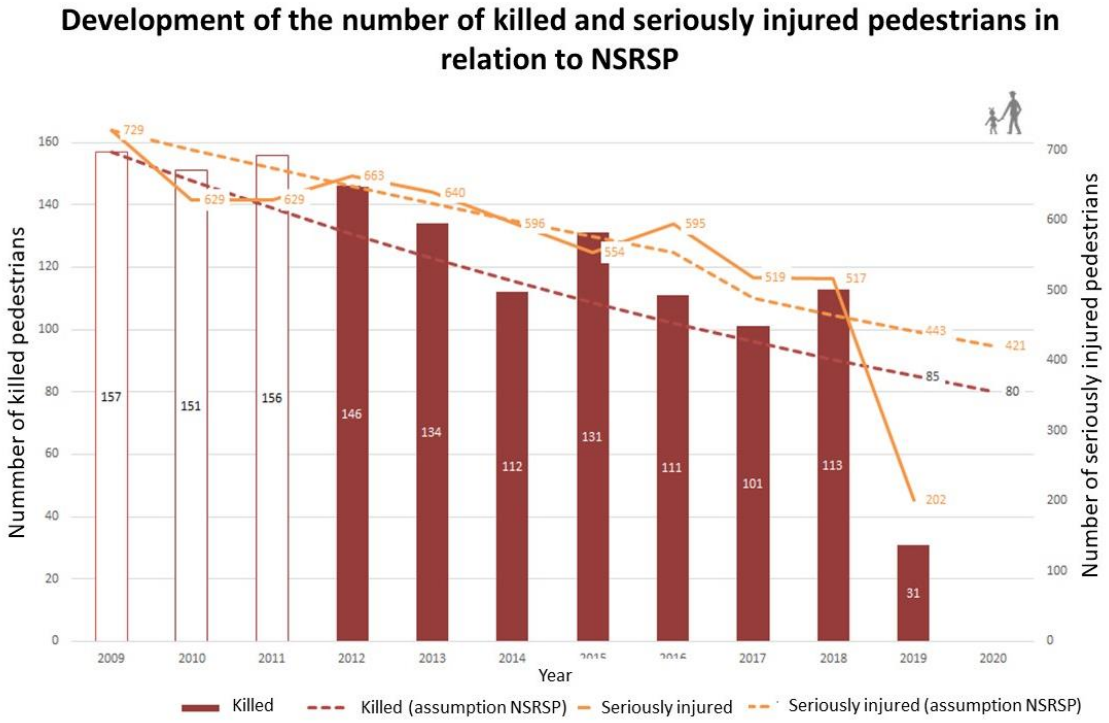

Figure 1-2 – Overview of the number of killed and seriously injured pedestrians over the past years. [6]

1.1.2 European Union

European Union has set a long-term goal to reduce the fatalities of accidents to zero. This initiative is called *The Vision Zero* [9] and has an origin in Sweden. Overall it can be summarized in one sentence: "*No loss of life is acceptable."* To fulfil this goal the interim targets were set. Generally, these targets aim to reduce the total number of serious injuries and deaths in the year 2020 by half compare to year 2010.

Currently the latest statistics data [10] shows that the number of causalities has dropped from 31 604 in the year 2010 to 25 047 in the year 2018. Even though it is a significant decrease of 20.7 % in the past 8 years the EU is still failing to achieve its interim goals. Achievement of these goals would require that the number of casualties drop by 40% by the year 2018 (compare to year 2010). This means, that in the year 2018 only 18 962 fatalities should occur.

As is illustrated in Figure 1-3 the Czech Republic, although it did not meet the requirements, was in better position to achieve the better average in the area of the killed pedestrian. Only two countries were able to get bellow the assumptions made by the EU: Slovenia with a decrease of 12.0 % and Denmark with a decrease of 11.9 %. [6]

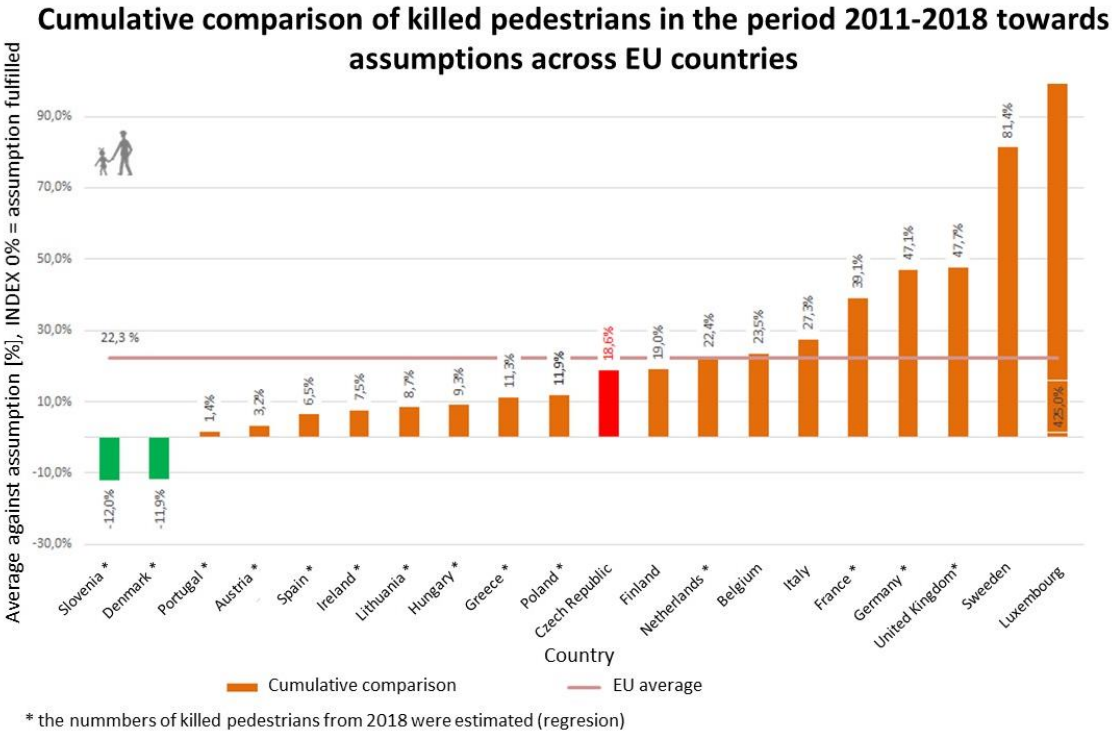

Figure 1-3 – Overview of pedestrian fatalities comparison in the EU. [6]

2 Pedestrian related collisions

Pedestrians and cyclists face a considerable risk of severe injury or death in a collision with a motor vehicle. Pedestrians account for up to 21% [11] of all road deaths in Europe, with older people and children at greatest risk. The main cause of the injuries is the enormous difference between the weights of the participants because the lighter object, the pedestrian, absorbs most of the energy generated by the collision. Another factor that affects the resulting injury is missing protection of the pedestrian or cyclists. The vehicle body, safety belts and airbags that can absorb the impact and may protect the passenger in the vehicle but, unfortunately in most cases, the pedestrians have no similar protection. The risk of fatality within a motor vehicle-related accident involving pedestrian is enormous and, as illustrated in Figure 2-1, significantly increases with the speed of the vehicle. It shall be noted that if the collision occurs at a speed of 30 $km \cdot h^{-1}$ the chance of pedestrian survival is up to 90%. Survival rate dramatically decreases with vehicle speed increments.

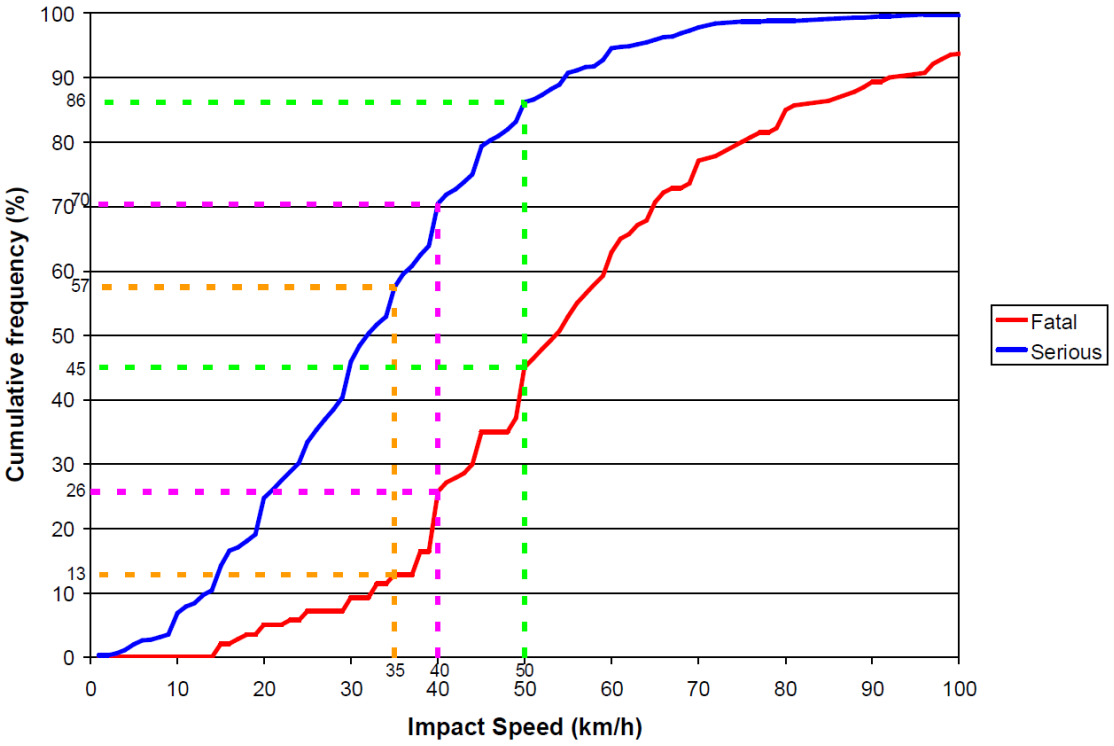

Figure 2-1 – Likelihood of pedestrian injuries vs. impact speed of the vehicle. [69]

As stated in the report [12] of the British research and mobility innovative company *TRL* the location of the pedestrian injuries are dominated by the damages of two body parts, the head and the lower extremities. This pattern of injuries is taken from hospital accident statistics, which record the injuries of pedestrian casualties who are admitted to hospitals in England. The absolute number of admissions stated in Figure 2-2 is related only to cases recorded in England however we may use this statistic as a marker for defying the most endangered body parts of the pedestrian. At first sight, it may look like that fracture of the lower leg is the most common type of injury and consequently establish the belief that lower extremities are the most vulnerable body parts. On the contrary, all injuries regarding the head such as the intracranial injuries, open wounds of the head, fractures of the skull and the superficial injuries of the head combined prove that the head is the most

vulnerable body part injured during the collision with the vehicle. Moreover, head injuries are usually more life threatening and have more serious consequences than lower extremities injuries.

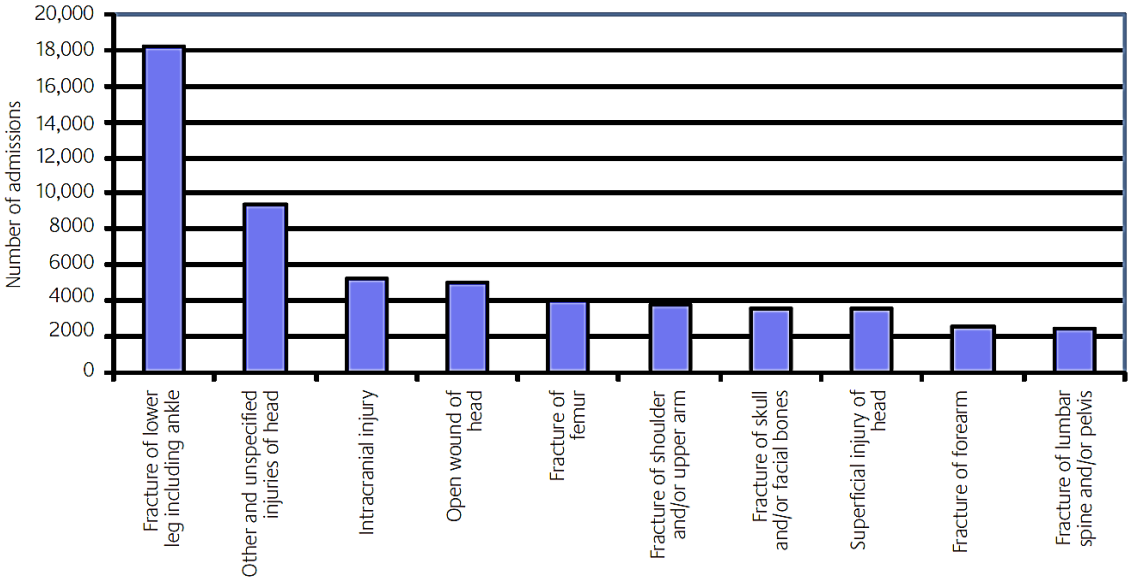

Figure 2-2 – Most frequent primary injuries in pedestrian collisions. [12]

Smooth vehicle body surface, safe clearance to rigid structures of the vehicle and energy-absorbing bumpers can help to protect pedestrians in the event of an impact. The more advanced technologies improving pedestrian safety are the dynamically raised bonnet and windscreen airbags.

New active safety systems able to automatically stop a car before it hits a pedestrian, can represent a big step forward for pedestrian safety if fitted across the vehicle fleet. Automatic braking systems use several sensors fitted around the vehicle that can predict the existence of the conditions around the vehicle and either warn the driver or even intervene by applying the brakes to avoid a crash.

2.1 Kinematics of the vehicle-pedestrian accident

It is essential to know how the body of the pedestrian behaves while undergoing car-related accidents. This knowledge allows us to understand the nature of the typical pedestrian injury and thus implement improvements on vehicle body decreasing the severity of injuries.

Even though the research in this field has undergone significant development in the past years, the kinematics of human body in the moment of the accident is still complicated to be fully described because of many factors influencing the resultant motion. The precise trajectory of pedestrian movement and the seriousness of the injury is dependent on [4]:

- Pedestrian factors – height and weight;
- Impact factors – velocity of the vehicle, relative angle between the frontal part of the vehicle and pedestrian
- Vehicle factors – a type of the vehicle, shape of vehicle frontal part and stiffness of components

The pedestrian-related accident could be divided into three phases as illustrated in Figure 2-3. First phase is the primary impact. Depending on the relative heights of the pedestrian and the front of the car, two cases may occur. The smaller vehicles may hit the pedestrian by the bumper to the lower parts of the pedestrian's leg (bumper-to-leg) or, in a case of the higher vehicle, the pedestrian's tight or pelvis would be hit by the front edge of the vehicle bonnet.

The second phase is the rolling of the pedestrians body over the vehicle until the upper body of the pedestrian hits the surface of the bonnet or the windscreen. This second phase is critical because the head hitting the vehicle bonnet is the most common and leads to most serious type of injuries related to pedestrian accidents [4]. The third phase is the ejection of the pedestrian to the roadway. The severity of the injury from the first and second phase could be optimized by the construction and design of the frontal part of the vehicle however that is not a case in the third phase of the impact.

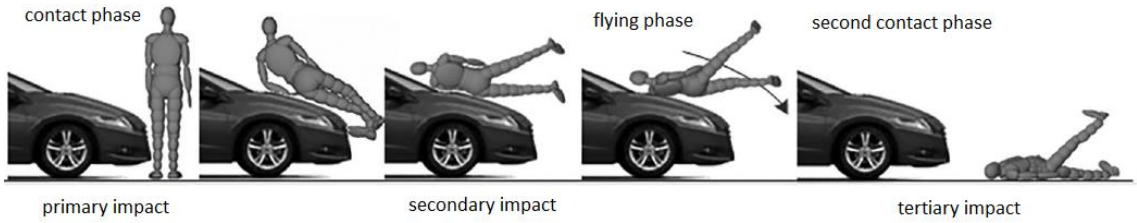

Figure 2-3 – Description of pedestrian-related collision. [70]

2.2 Definition of the and test areas reference lines

To proceed with the description of how to execute the pedestrian protection tests, it is first necessary to define the areas on motor vehicle front face where the tests shall be performed. These test areas are defined by the *Commission Regulation No 631/2009 laying down detailed rules for the implementation of Annex I to Regulation No 78/2009 of the European Parliament and of the Council* [13], [14] and by *Regulation No. 127* of the *UNECE* concerning the pedestrian safety. [3] Due to the complexity of the pedestrian protection, only definition and areas related to the impactors' testing will be mentioned.

2.2.1 Normal ride attitude

While marking the reference lines and testing areas the vehicle shall be positioned in normal ride attitude. This position itself is defined in regulations as follows:

"Normal ride attitude means the vehicle attitude in running order positioned on the ground, with the tyres inflated to the recommended pressures, the front wheels in the straight-ahead position, with maximum capacity of all fluids necessary for operation of the vehicle, with all standard equipment as provided by the vehicle manufacturer, with a mass of 75 kg placed on the driver's seat and with a mass of 75 kg placed on the front passenger's seat, and with the suspension set for a driving speed of 40 km/h or 35 km/h in normal running conditions specified by the manufacturer. Especially for vehicles with an active suspension or a device for automatic levelling." [14]

When the vehicle is positioned and prepared in its normal ride attitude, we can proceed with the description of the other definitions. According to the regulations, the test areas and reference line are defined as follows:

2.2.2 Bumper

"*Bumper means the front, lower, outer structure of a vehicle. It includes all structures that are intended to give protection to a vehicle when involved in a low speed frontal collision and also any attachments to this structure. The reference height and lateral limits of the bumper are identified by the corners and the bumper reference lines*." [3].

2.2.3 Corner of the bumper

"Corner of bumper" means the vehicle's point of contact with a vertical plane which makes an angle of 60° with the vertical longitudinal plane of the vehicle and is tangential to the outer surface of the bumper." [13] We refer the reader to see Figure 2-4 in which the corner of the bumper is illustrated.

2.2.4 Third of the bumper

"Third of the bumper means the geometric trace between the corners of the bumper, measured with a flexible tape following the outer contour of the bumper, divided into three equal parts." [13]

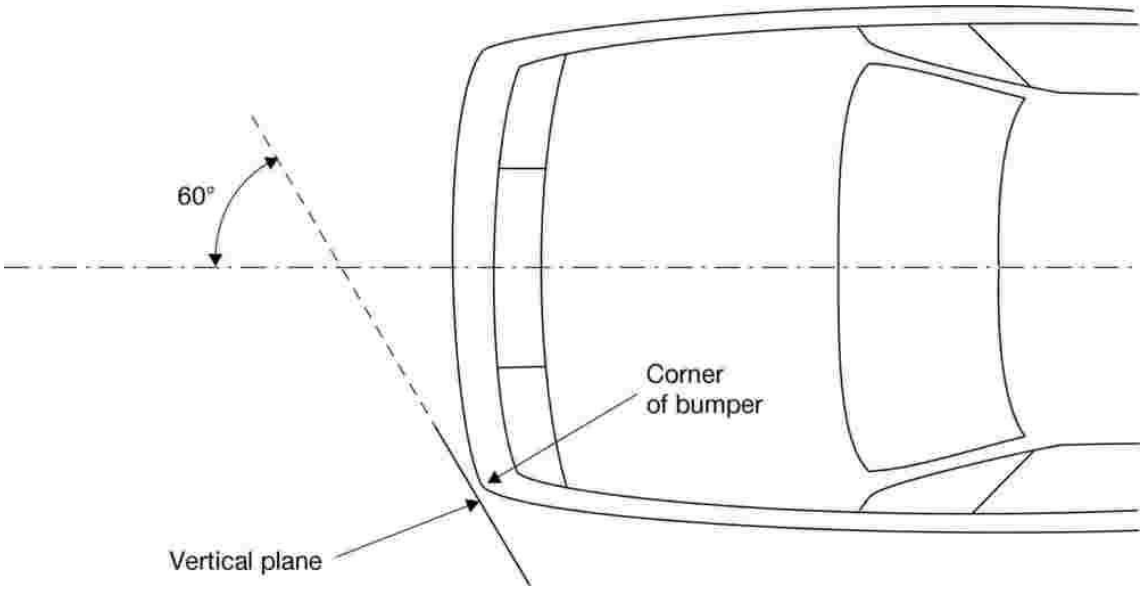

Figure 2-4 – Determination of the corner of the bumper. [13]

2.2.5 Lower bumper reference line

"Lower bumper reference line means the lower limit to significant points of pedestrian contact with the bumper. It is defined as the geometric trace of the lowermost points of contact between a straight edge 700 mm long and the bumper, when the straight edge, held parallel to the vertical longitudinal plane of the car and inclined forwards by 25°from the vertical, is traversed across the front of the car, while maintaining contact with the ground and with the surface of the bumper." [13]. For illustration, the reader is referred to see Figure 2-5.

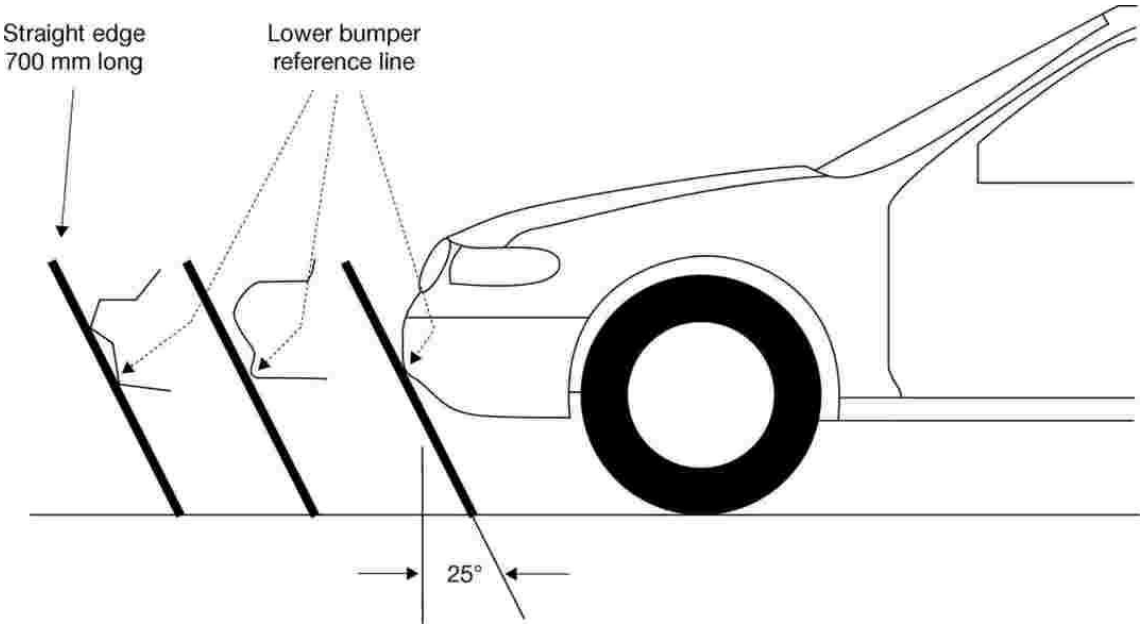

Figure 2-5 – Determination of the lower bumper reference line. [13]

2.2.6 Upper bumper reference line

"Upper bumper reference line" means the upper limit to significant points of pedestrian contact with the bumper. For vehicles with an identifiable bumper structure it is defined as the geometric trace of the uppermost points of contact between a straight edge and the bumper, when the straight edge, held parallel to the vertical longitudinal plane of the car and inclined rearwards by 20° to the vertical, is traversed across the front of the car, while maintaining contact with the surface of the bumper." [13] The process of determination of the upper bumper reference line is shown in Figure 2-6.

2.2.7 Bonnet leading edge

"Bonnet leading edge' means the front of the upper outer structure, including the bonnet and wings, the upper and side members of the headlight surround and any other attachments." [13]

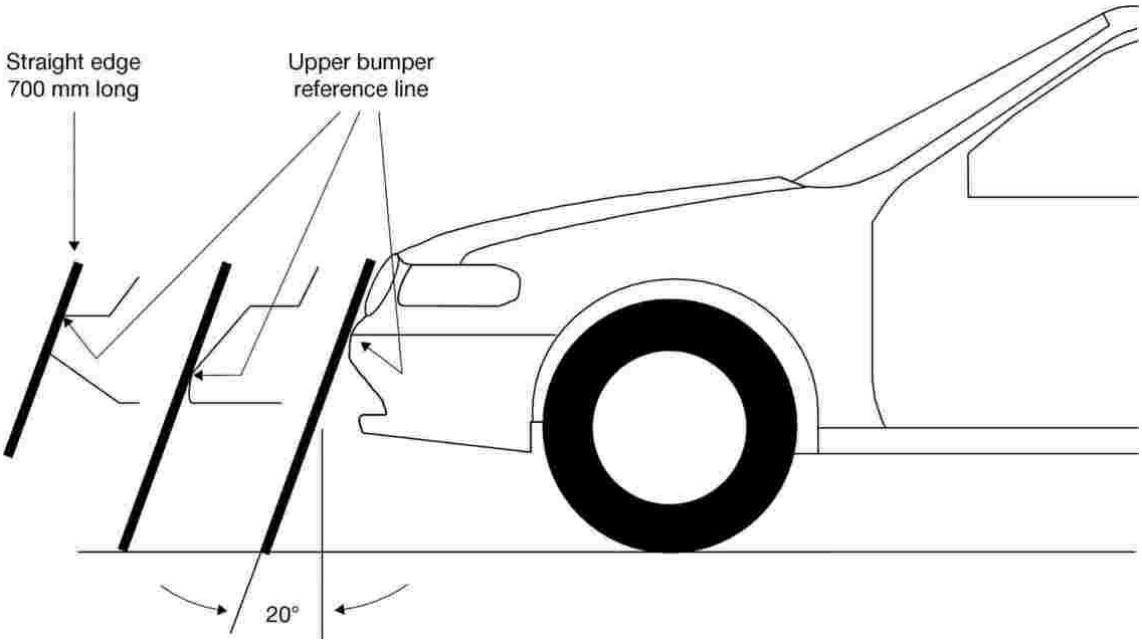

Figure 2-6 – Determination of the upper bumper reference line. [13]

2.2.8 Bonnet leading edge reference line

"Bonnet leading edge reference line" means the geometric trace of the points of contact between a straight edge 1,000 mm long and the front surface of the bonnet, when the straight edge, held parallel to the vertical longitudinal plane of the car and inclined rearwards by 50° from the vertical and with the lower end 600 mm above the ground, is traversed across and in contact with the bonnet leading edge." [13]

This procedure is obvious in Figure 2-7.

The definition of bonnet leading edge reference line is different for vehicles that have an unusual front face shape or inclination of the bonnet top greater than 50°. For more details, the reader may see *Part I* of *Commission Regulation No 631/2009* point 2.2.

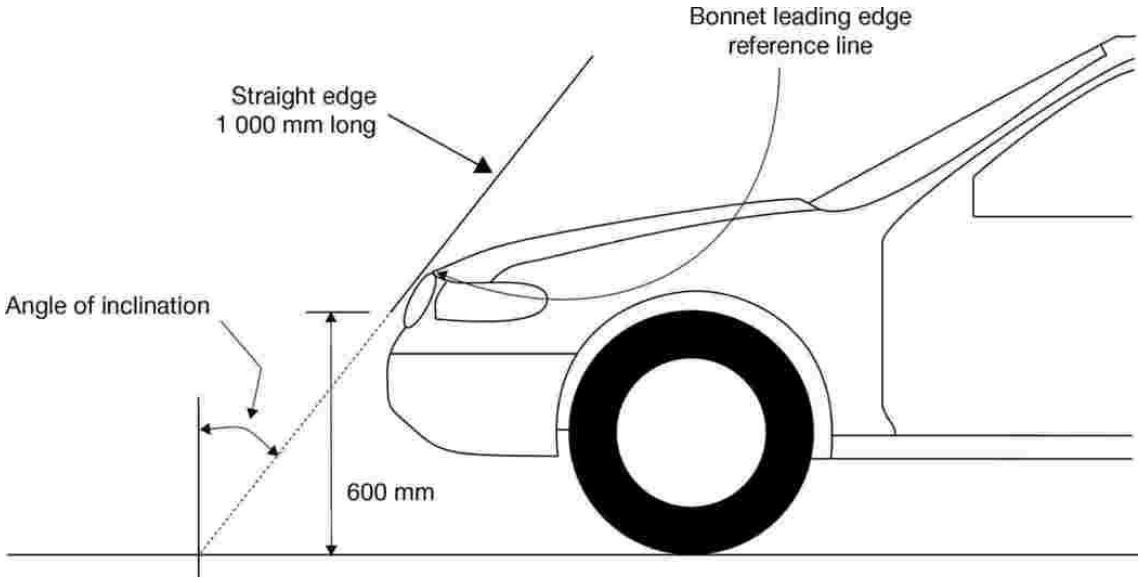

Figure 2-7 – Determination of the bonnet leading edge reference line. [13]

2.2.9 Third of the bonnet leading edge

"Third of the bonnet leading edge means the geometric trace between the corner reference points, measured with a flexible tape following the outer contour of the leading edge, divided in three equal part." [13]

2.2.10 Bumper lead

"Bumper lead for any longitudinal section of a vehicle means the horizontal distance measured in any vehicle vertical longitudinal plane between the upper bumper reference line and the bonnet leading edge reference line." [13]

2.2.11 Bonnet rear reference line

"Bonnet rear reference line' means the geometric trace of the most rearward points of contact between a 165 *mm sphere and the frontal upper surface, when the sphere is traversed across the frontal upper surface, while maintain-ing contact with the windscreen. The wiper blades and arms are removed during this process".* For illustration, see Figure 2-8.

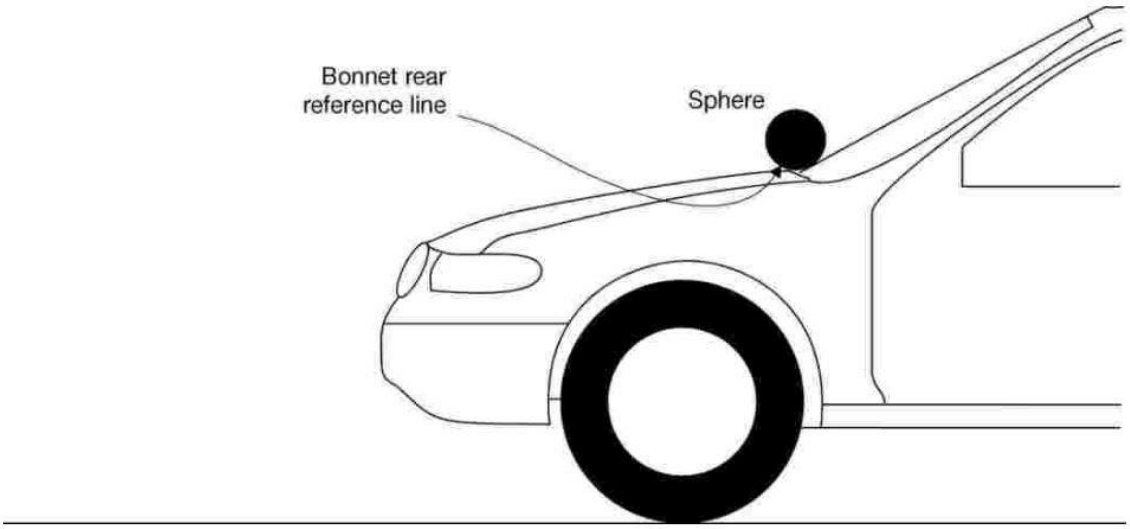

Figure 2-8 – Determination of the bonnet rear reference line. [13]

"If the bonnet rear reference line is located at a wrap around distance of more than 2 100 mm, the bonnet rear ref-erence line is defined by the geometric trace of the 2 100 mm wrap around distance. Where the bonnet rear refer-ence line and side reference lines do not intersect, the bonnet rear reference line shall be modified according to the procedure set out in point 2.17 of Annex I of Commission Regulation No. 631/2009." [13]

2.2.12 Wrap around distance

"Wrap Around Distance (abbreviated WAD) *means the geometric trace described on the outer surface of the vehicle front structure by one end of a flexible tape, when it is held in a vertical longitudinal plane of the vehicle and traversed across the front structure. The tape is held taut throughout the operation with one end held at ground reference level, vertically below the front face of the bumper and the other end held in contact with the front structure".* See Figure 2-9. *"The vehicle is positioned in the normal ride attitude.*

This procedure shall be followed, using alternative tapes of appropriate lengths, to describe wrap around distances of 1,000 mm (WAD1000), of 1,700 mm (WAD1700) and of 2,100 mm (WAD2100).” [3]

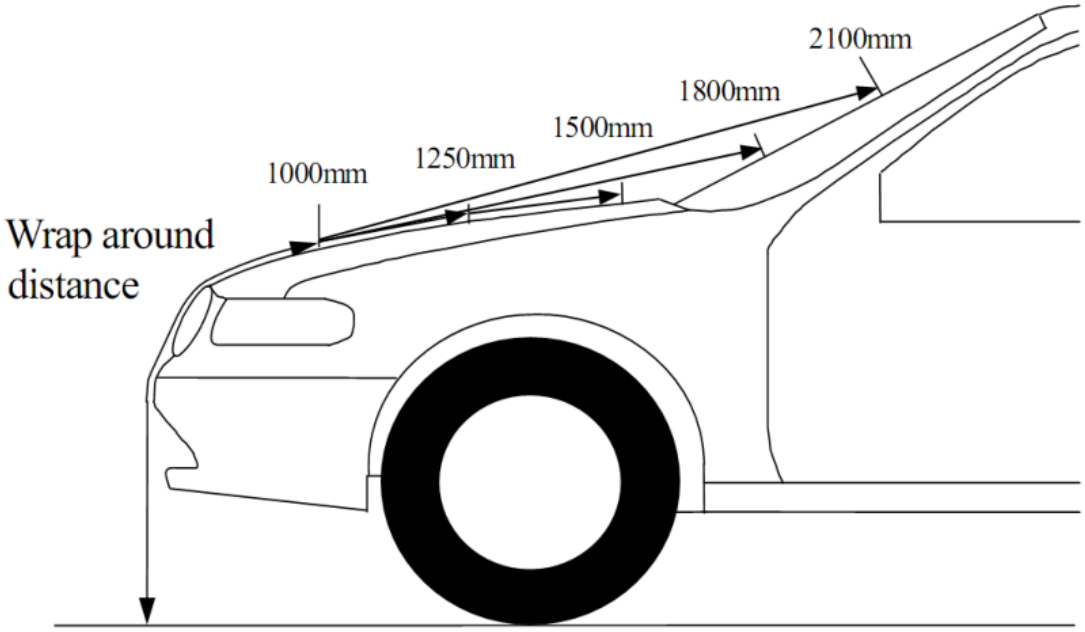

Figure 2-9 – Illustration of the wrap around distance. [71]

2.2.13 Side reference line

“Side reference line means the geometric trace of the highest points of contact between a straight edge 700 mm long and the side of a vehicle, when the straight edge, held parallel to a transverse vertical plane of the vehicle and inclined inwards by 45° is traversed down the side and maintains contact with the sides of the frontal upper surface.” [13] For illustration, how the side reference line is marked see Figure 2-10.

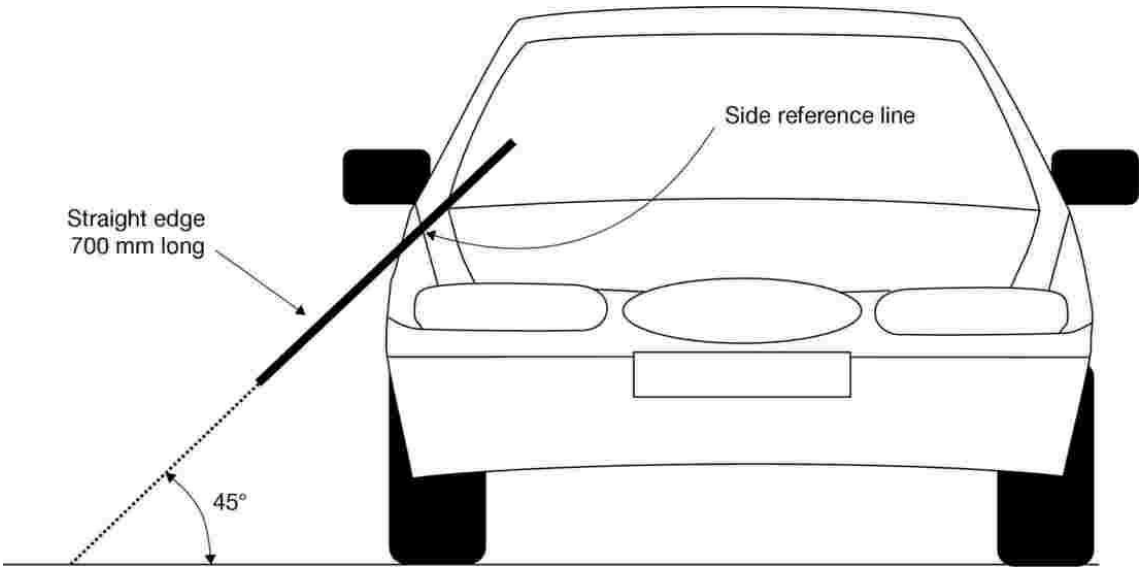

Figure 2-10 – Determination of side reference line. [13]

2.2.14 Corner reference point

"Corner reference point means the intersection of the bonnet leading edge reference line and of the side reference line." [13]

2.2.15 Bonnet top

"Bonnet top means the outer structure which includes the upper surface of all outer structures except the wind-screen, the A-pillars and structures rearwards of them; it therefore includes, but is not limited to, the bonnet, wings, scuttle, wiper spindle and lower windscreen frame." [14]

By other words:

"*Bonnet top is area, which is bounded by the bonnet leading edge reference line, the bonnet rear reference line and the side reference lines.*" [13]

2.2.16 Third of the bonnet top

"Third of the bonnet top means the geometric trace of the area between the side reference lines, measured with a flexible tape following the outer contour of the bonnet top on any transverse section, divided in three equal parts." [13]

2.2.17 Windscreen

"Windscreen means the frontal glazing of the vehicle situated between the A-pillars." [3]

2.2.18 Rear windscreen reference line

The rear windscreen reference line definition is similar to the bonnet rear reference line.

"Rear windscreen reference line means as the geometric trace of the most forward points of contact between a sphere and the windscreen, when a sphere of diameter 165 mm is traversed across the windscreen top frame, including any trim, while maintaining contact with the windscreen." [13] For illustration, this process is shown in Figure 2-11.

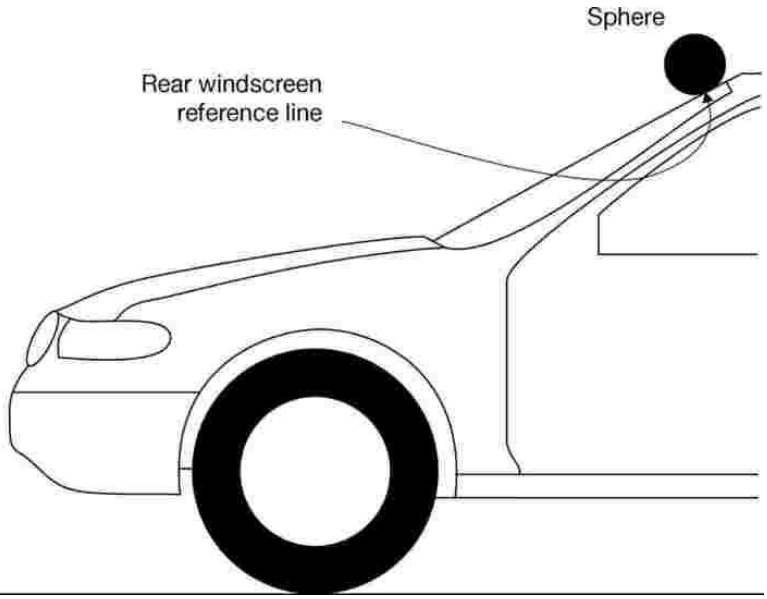

Figure 2-11 – Determination of rear windscreen reference line. [13]

2.3 Pedestrian safety assessment criteria

2.3.1 Dynamic knee bending angle and dynamic knee shearing displacement

The knee, as the largest and most complicated joint in the human body, could be a source of many injuries while undergoing collision with the vehicle bumper or bonnet leading edge. From a mechanical point of view, the knee represents a joint with only one degree of freedom. When we apply displacement or rotational load to the knee in directions, which are restricted by the ligaments or condyles the serious injuries might occur.

The dynamic knee bending angle represents relative rotation between the tibia and femur bones in the lateral direction. Such movement happen if the joint would be hit from the side. Dynamic knee shearing displacement is defined as relative motion between the tibia and femur at the knee joint level in the lateral direction.

To evaluate the consequences of loads applied to the knee, the studies using cadaver lower extremities were performed. One of the outcomes was that the resultant injury of the knee joint depends on the knee preload as well as on the dynamics of the load. *European Enhanced Vehicle-safety Committee* (EEVC) has considered this effect and carried out experiments at high-velocity corresponding with the speed of pedestrian collisions. If the knee is a subject to bending load, the most common initial damage can be observed when the knee joint was bent laterally at angle of $15°$ for ligament avulsion failure (injury in which a body structure is torn off) or at angle of $16°$ for diaphysis (midsection of the long bone) fracture. If the knee is deformed subject to shearing load, the two most common initial damage failures appear as the lateral shearing displacement of $16\ mm$ for epiphysis (the rounded end of a long bone) failure or as displacement of $28\ mm$ for diaphysis fracture. The peak shearing force required to cause such injuries in lateral direction was $2.4\ kN$ and $2.9\ kN$ respectively. The peak of the bending moment appears within the range of $400 - 500\ Nm$. [15]

The outcomes from these studies set the threshold for the assessment whether the vehicle meets lawful conditions for type approval while undergoing pedestrian protection tests focused on lower extremities.

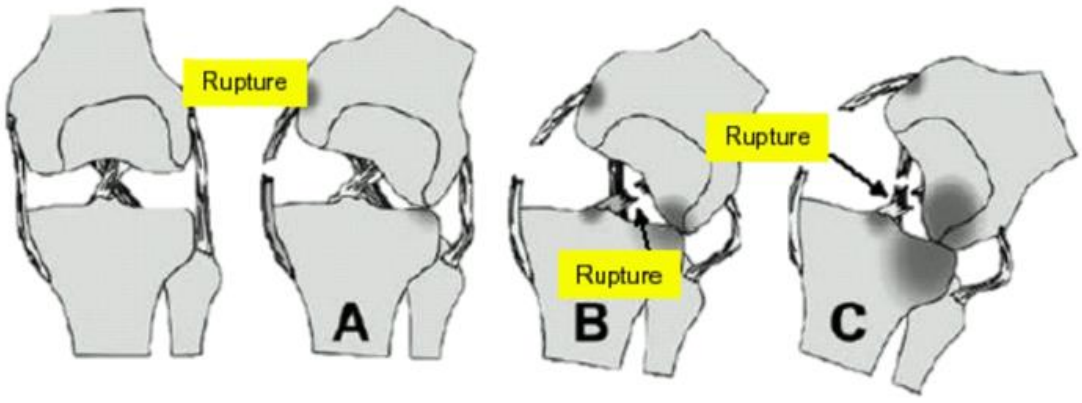

Figure 2-12 – Stages of left knee injury. [72]

Figure 2-12 illustrates a frontal view of the stages of the left knee injury in a case that the knee is turned outwards from its vertical axis. Stage "*A*" shows rupture of the medial collateral ligament followed by the stage "*B*" with abruption of the anterior cruciate ligament. The final stage "*C*" represents the rupture of the posterior cruciate ligament. This type of injury mechanism is present when the compression of the lateral tibial and femoral condyles increase as a result of strike to the pedestrian lower extremities caused by a vehicle.

2.3.2 Head injury criterion

Taking into account the number of most frequent injuries and the consequences of head or brain injury, the bio-mechanic engineers and pedestrian protection research community has focused on developing a criteria describing head injury based on the physical parameter of the collision. These criteria were developed as the indicator of the likelihood of the brain damage and skull fractures. Former system proposed as a reliable injury measure was the *Wayne State Tolerance Curve* (WSTC) which defined a boundary between safe and damaging acceleration of head as a resultant of the collision. The successor of the WSTC was the *Gadd Severity Index* (GSI). The modification of the GSI called *Head Injury Criterion* [4](HIC) was proposed more than four decades ago and is up to today the most commonly used criterion to assess the severity of the head injury. [16]

The difference between the GSI and HIC is in limited time interval in which the criterion is evaluated. To investigate the connection of the HIC with human head injuries, the impact, drop and pendulum tests were conducted on animals, cadavers and human volunteers to develop the predicted cumulative function of the severe injury depending on HIC values. [17]

The severity of the injury can be described by using the *Abbreviated Injury Scale* (AIS). The probability of death is increasing with every level starting with level one and goes up to level six with no probability of survival. An example of AIS 1 injury is the superficial laceration while an example of AIS 6 injury is the total aorta severance. As expected, the severity of the injury, thus AIS level, depends on the HIC value. Figure 2-14 shows the individual AIS head injury risk curves based on the HIC values.

The validation of the severity of the injury vs. HIC values has been performed by many studies and under different circumstances. E.g. from the study prepared by Hayes, Erickson and Power [18] it is evident, that for the HIC value of 1 000 there is approximately a 16% probability of suffering an AIS4+ head injury while the HIC value of 1 500 coincide with 50% likelihood of ASI4+ head injury. The risk curves are illustrated in Figure 2-14.

Figure 2-13 shows the chart of the probability of for the life-threatening brain injury as a function of HIC. From Figure 2-13 it is not possible to define the severity of the injury however the main benefit of this figure is a direct dependency representation between the fatality probability and the HIC values.

[4] In regulation of the European Parliament and the Council this criterion is referred as a *Head Performance Criterion* (HPC). Although different titles these criteria are identical. [73]

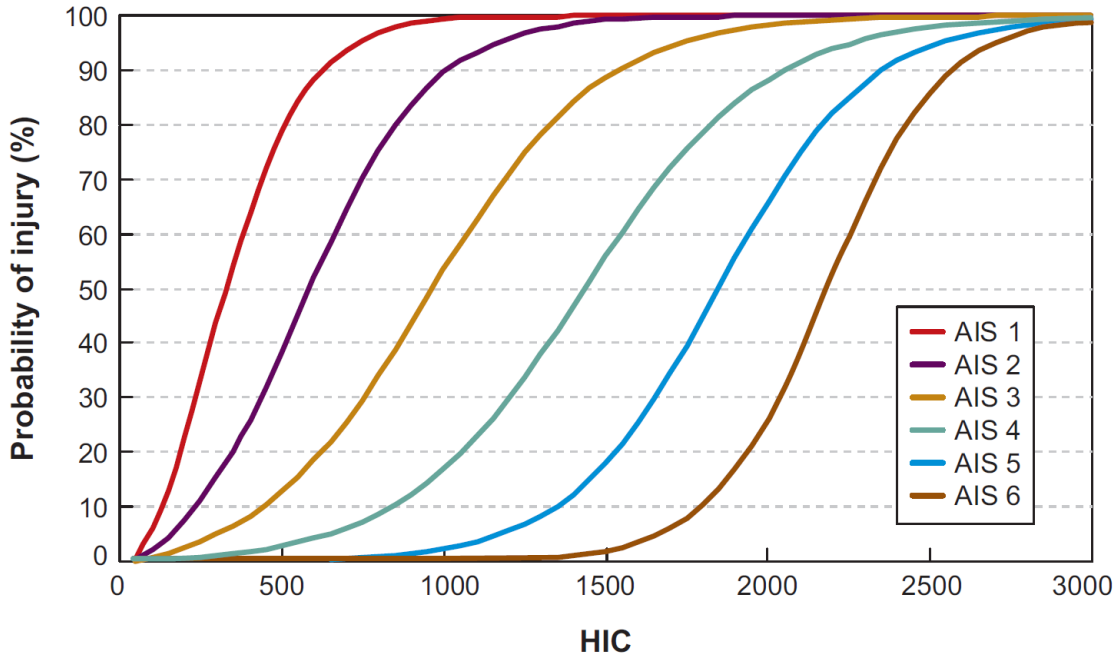

Figure 2-14 – Head injury risk curves based on HIC values. [18]

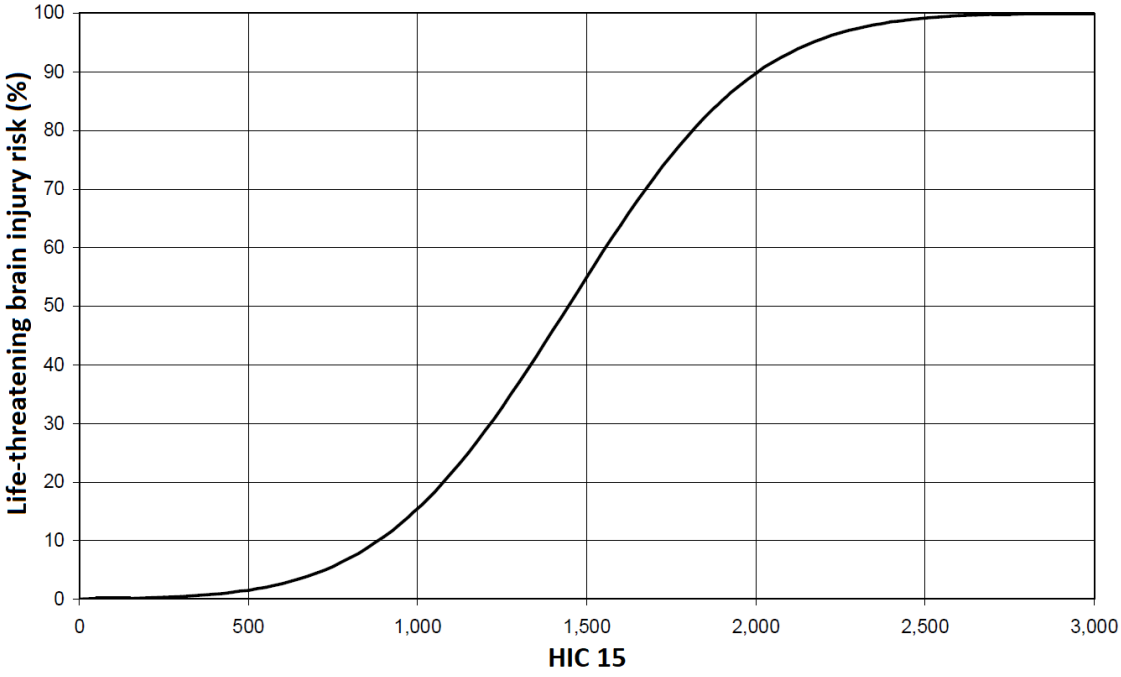

Figure 2-13 – Example of the risk curve for life-threatening brain injury. [69]

2.3.2.1 Calculation of the HIC value

The HIC value shall be calculated by using the following formula [19], [14]

$$HIC(\Delta t_{max}) = \max_{t_1,t_2}\left\{\left[\frac{1}{t_2 - t_1}\int_{t_1}^{t_2} \widehat{a_r} \cdot dt\right]^{2.5} \cdot (t_2 - t_1)\right\} \tag{2.1}$$

subject to:

$$t_2 - t_1 \leq \Delta t_{max} \tag{2.2}$$

Where $\widehat{a_r}$ is a resultant acceleration measured in units of g. The magnitude of the acceleration $\widehat{a_r}$ shall be calculated as a geometric sum of individual axes acceleration measured in the headform impactor´s centre of the gravity divided by the gravity of Earth to express acceleration in units of g:

$$\widehat{a_r} = \frac{a}{g} = \frac{\sqrt{a_x^2 + a_y^2 + a_z^2}}{g} \tag{2.3}$$

Where $g \approx 9.807\ m \cdot s^{-2}$

The time instances t_1 and t_2 expressed in seconds are defying the beginning and the end of the record for which is the HIC value maximum. The result is then called HIC_{15} if the time interval Δt_{max} is $15\ ms$ and HIC_{36} for Δt_{max} equals to $36\ ms$. For the type-approving purposes the HIC values calculated within the time interval greater than $15\ ms$ shall not be taken into account [14]. The main reason for not using the longer time interval is that head impacts take place within a few milliseconds. As this pulse itself is shorter than $15\ ms$ there is no risk of losing some part of acceleration curve while calculating the HIC. The second reason for time interval restriction is that the head injury, thus HIC values, are supposed to be dependent on head acceleration and duration of the impulse. Such requirement is set to exclude unreliable results.

One of the disadvantages using the HIC criterion is, that for evaluation of the head injury, exclusively the translational acceleration is used and the rotational effects are completely neglected. [20]

2.4 Pedestrian protection tests

Already in 1970, the *European Enhanced Vehicle-safety Committee* (EEVC) began to focus on pedestrian safety on the roads [21]. Gradually, data collection and evaluation obtained from pedestrian accidents related to this topic become the task for *Working Group 1* (WG 1). At the beginning of the eighties, the *Working Group 7* (WG 7), began to perform tests with models representing individual parts of the human body. Since 1991, the working group labelled as EEVC WG10 started to develop a methodology for pedestrian protection tests and criteria that would improve a chance of pedestrian survival during the collision. The proposal was completed and adopted in 1992 by the *Council Directive 74/483/ECC* related to the external projections of motor vehicles. In 1999, the EEVC WG 17 was established to improve methodologies and regulations.

Type approval of the motor vehicle in regards to the protection of pedestrians and other vulnerable road users requires and defines a series of tests that shall be conducted. These tests are prescribed by the *Regulation (EC) No 78/2009 of the European Parliament and of the Council* [14] to the car manufactures as compulsory for every vehicle type sold on the territory of European Union. This regulation defines the specifications for the construction of the motor vehicle and its frontal protection systems to decrease the number and seriousness of pedestrian-related accidents. The series of tests to which individual car models are subjected is designed to represent, in a simplified form, the most common scenarios of the road accidents, which can result in injury or even death to the pedestrian.

In November 2019 a new *Regulation 2019/2144 of European Parliament and of the Council* [22] came into force. This regulation repeals currently used *Regulation No 78/2009* and *631/2009* with the effect from 6th July of 2022 to simplify and harmonize the requirements for the protection of pedestrians and other vulnerable road users. Since the technical requirements and test procedures developed at UN level are more advanced the *Regulation No 2019/2144* accepts type-approval of a motor vehicle in accordance with the UN Regulations as EU type-approval. Therefore, from the year 2022 the pedestrian protection test shall be conducted only in accordance with the UN Regulation No. 127 [3] as the only standard.

Generally, the collision with the pedestrian is a complex problem and it would be difficult to perform a full mock test experiment with the dummy. To simplify that issue , only the parts of the dummy (impactors), representing individual parts of the human body, are used. These impactors could be divided into three types according to their corresponding body parts. For evaluation of the simulated collision, the lower legform impactor, the upper legform and headform impactors are used [13]. The test areas of the vehicle and its associated impactors are illustrated in Figure 2-15.

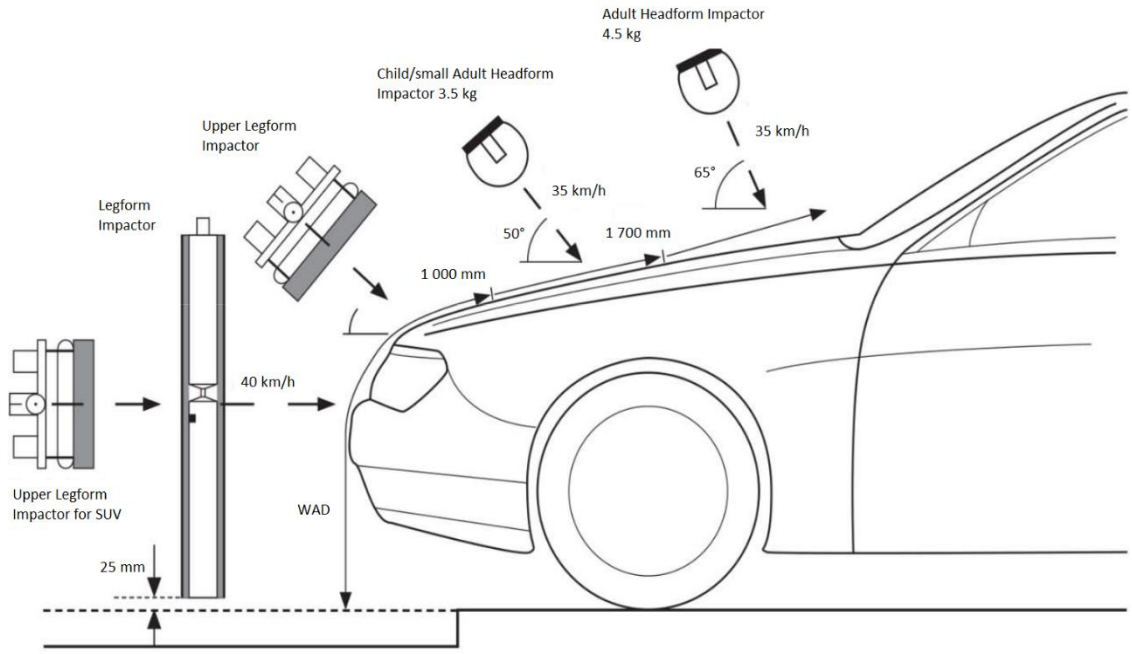

Figure 2-15 – Illustration of impact tests for pedestrian protection. [75]

2.4.1 Lower legform impact tests

Typical injuries resulting from a pedestrian collision with a car bumper are fractures of the lower limb, knee and a damage to the ligament. These injuries are rarely fatal but unfortunately are often associated with a permanent disability. For the evaluation of the severity of these injuries, only the maximum dynamic knee bending angle and the dynamic knee shearing displacement are assessed.

Lower legform to bumper test is obligatory for vehicles with a height of the lower bumper reference line below $425\ mm$. If the height of the vehicle lower bumper reference line lies within a range between $425\ mm$ and $500\ mm$ the vehicle manufacturer may choose to apply either lower legform or upper legform to bumper test. For proper evaluation of the test, a minimum of three impacts shall be conducted. One of these tests shall be directed to the centreline of the vehicle and other two to the outer thirds of the bumper at the positions predicted to be the most likely to cause injuries. At the time of the first contact, the impactor vertical centreline shall be within $\pm 10\ mm$ tolerance towards the selected target location. [13]

The methodology of the test shall be as follows:

The lower legform impactor is propped to the impact speed of $11.11 \pm 0.2\ m \cdot s^{-1}$ while the effect of the gravity shall be taken into account. The vertical axis perpendicular to the horizontal plane shall be within $\pm\ 2°$ of the lateral and longitudinal planes. The minimum height between ground reference level and the bottom of the impactor at the time of the first contact shall be $25\ \pm 10\ mm$. [13]

To pass this test, the maximum dynamic knee bending angle shall not exceed 19.0 °, the dynamic knee shearing displacement shall not be greater than $6.0\ mm$ and the acceleration measured at the upper end of the tibia shall not exceed $170\ g$. [14]

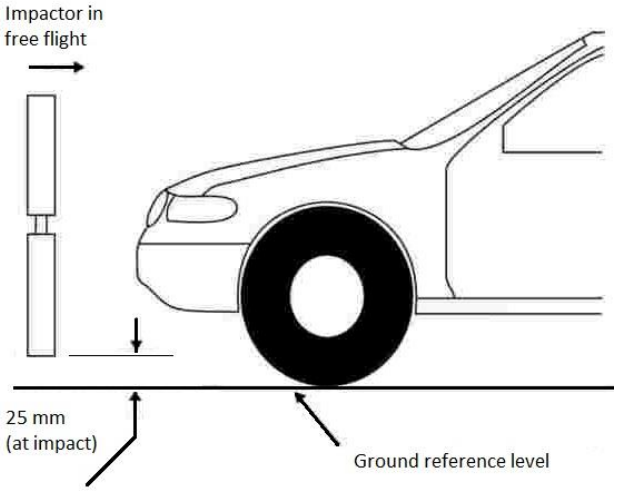

Figure 2-16 – Lower legform to the bumper test for the complete vehicle in normal ride attitude. [13]

For illustration, Figure 2-16 demonstrates the execution of lower legform to the bumper test.

2.4.2 Upper legform impact tests

The shape of the bumper or the bonnet leading edge can play a key role in the outcome of a pedestrian collision with the vehicle. If these parts of the vehicle are not correctly designed, they may adversely contribute to injuries to the femur or the pelvis. The severity of these injuries is determined by evaluating of the bending moments and the sum of all forces acting on the impactor. For the assessment of the pedestrian protection in regard of lower extremities, a vehicle is tested with the upper legform impactor in two areas - the bumper and the bonnet leading edge.

The test of the bumper with the upper legform impactor must apply to vehicles with the lower bumper reference line height greater than $500\ mm$. If the height of the lower bumper reference line is less than $500\ mm$ but exceeds $425\ mm$, the car manufacturer may choose to conduct either lower or upper legform to bumper test. [13]

In the case of the bumper testing, the execution and the test areas of the upper legform test are the same as the lower legform to bumper test.

Testing of the bonnet leading edge is performed differently. The first difference is, unlike the lower legform and headform impactors, that the upper legform impactor is still connected to the throwing device while testing the bonnet leading edge at the moment of impact. Test points are than determined same way as in a case of bumper tests described in the previous paragraphs with the exception that the test points in each third shall be selected in a such manner that the kinetic energy of impact exceeds $200\ J$. The selected target points shall be hit with a tolerance of $\pm 10\ mm$ in the lateral direction and the impactor centreline shall be convenient with the bonnet leading edge reference line with a $\pm\ 10\ mm$ tolerance. [13]

The required impact velocity and the impact angle are determined by empirical charts using the known values of the bonnet leading edge height and bumper lead. The tolerance to the impact velocity is $\pm\ 2\ \%$ and the tolerance to the impact angle is $\pm\ 2°$.Testing the vehicle bumper or the bonnet leading edge using the upper legform impactor shall have

variable weight. The weight is defined in accordance with the impact velocity and the required energy. The total mass impacting the bonnet shall be as follows: [13]

$$M = \frac{2E}{v^2} \tag{2.4}$$

where M $[kg]$ is the mass of the upper legform impactor assembly including the impactor itself, propulsion and the guidance components and extra weights to give the calculated mass. E $[J]$ is the energy of impact and v $[m \cdot s^{-1}]$ is the impact velocity, both derived from charts. The set of upper legform to the bonnet leading edge test is illustrated in Figure 2-17.

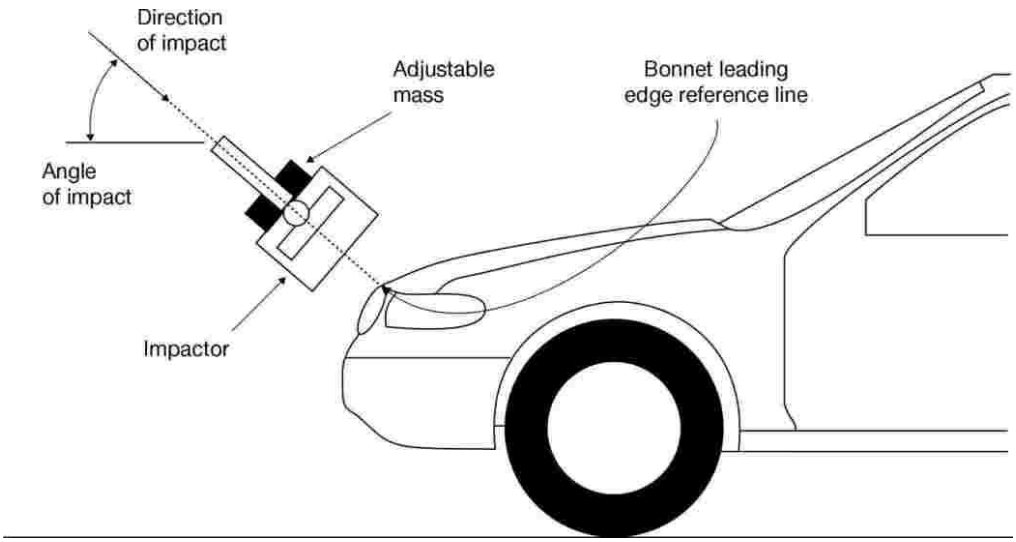

Figure 2-17 – Upper legform to bonnet leading edge test. [13]

To pass the upper legform test series the instantaneous sum of the impact forces time shall not exceed 7.5 kN for a case of upper legform to bumper test and 5.0 kN for a case of upper legform to the bonnet leading edge. The threshold of 5.0 kN is not compulsory however the test results shall be recorded and compared with possible targets. The dynamic bending moment of the impactor striking the bumper shall not exceed 510 Nm. In the case of bonnet leading edge, the result shall be recorded and compared with the possible target of 300 Nm. [14]

To mitigate the impact of a collision, a structure that promotes better energy absorption or other shapes of the bumper shall be used. For example, placing the bumper lower so the lower limb is hit as low as possible below the knee or removing sharp edges that were designed primarily for vehicle appearance.

2.4.3 Headform impact tests

The analysis of the most common injuries related to the pedestrian accidents [12] shows that the head is the most vulnerable part of the human body. During the collision, the pedestrian´s head can suffer various injuries depending on the load conditions and the prepositions of the pedestrian. As expected, the head impact points on the vehicle front-end depend on many parameters. Mainly on the height of the pedestrian, the impact speed and generally on the shape of vehicle bonnet. For illustration, a representative of each vehicle type in collision with a pedestrian is shown in Figure 2-18. Moreover, in comparison with legform impactors, three types of headform impactors are used to simulate both the adult and child pedestrians and different test areas.

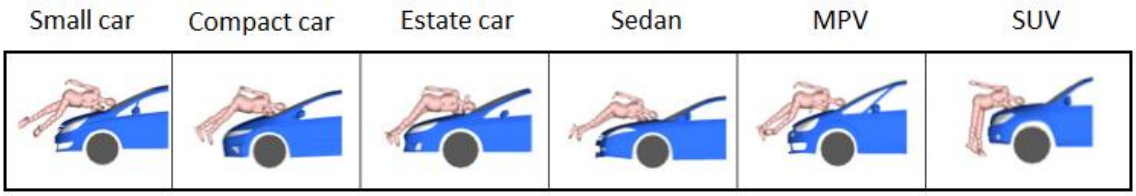

Figure 2-18 – Representatives of several vehicle types striking a pedestrian. [4]

From the illustration it is evident that if we want to evaluate the consequences of the accident, we shall apply the headform impact tests to different areas of the vehicle front-end. Every test related to headform impactor has similar execution, only the initial conditions as impact angle and impactor used could vary. In every case, the impactor shall be propelled by air, spring or hydraulic throwing device such that the impactor experience the state of free flight. The release distance between the vehicle bonnet and the impactor should be such that the results are not influenced by contact of the impactor with the propulsion system after the impactor rebound. [13]

For setting up the experiment, the vehicle shall be positioned in its normal ride attitude. Assuming that the vehicle bonnet is fitted with a badge, figurine or similar object which would yield under compressive force lesser than $100\ N$, then such force is applied before or while the measurement is conducted. Further on, the vehicle and the laboratory instrumentation shall be tempered to $20°C\ \pm 4°C$. When all these tasks are performed, then the vehicle is ready for the experiment.

Within every headform impact test, the direction of the impact shall be in a longitudinal plane of the vehicle through the impact point and the tolerance for the impact is $\pm\ 10\ mm$ from the desired impact point. Although the impact velocity of each impactor while striking the test area shall be $9.7\ \pm 0.2\ m \cdot s^{-1}$, the impact angle is altering depending on the used headform impactor. In both cases, the effect of the gravity must be taken into account while defying the propulsion velocity and the angle.

The impactor velocity shall be measured in the state of its free flight with $0.01\ m \cdot s^{-1}$ accuracy. Considering all factors, which may affect the impactor in the state of the free flight such as the effect of the gravity or the air resistance, the measured velocity might vary from the impact velocity. To eliminate those effects, the measured velocity shall be adjusted to determine the velocity of the impactor at the moment of impact. While post-processing the experiments, the acceleration vs. time history is used to calculate the HIC value. This criterion is a threshold for passing this type of tests and the particular maximum values for every test is described below. [13]

2.4.3.1 Adult headform to windscreen test

This test is intended to assess the pedestrian safety in a case when the pedestrian's head hit the windscreen of the vehicle. The results are recorded for monitoring purposes only. This means that the resultant HIC value shall be compared with the possible target of 1 000, but the fulfilment of this criterion is not obligatory. It is expected that the current version of regulation will be revised and this test will become obligatory to guarantee better pedestrian protection.

For the assessment, a minimum of five tests shall be carried out and the impact points should be chosen to be the most likely to cause injury. The selected impact points shall be at minimum $165\ mm$ apart and at least $82.5\ mm$ from the windscreen borders as shown in Figure 2-19. If a certain number of test points have been tested and the remaining area is too small to conduct another test while maintaining the prescribed distances, less than five tests may be carried out. The impact points tested in the laboratory shall be recorded in the test protocol.

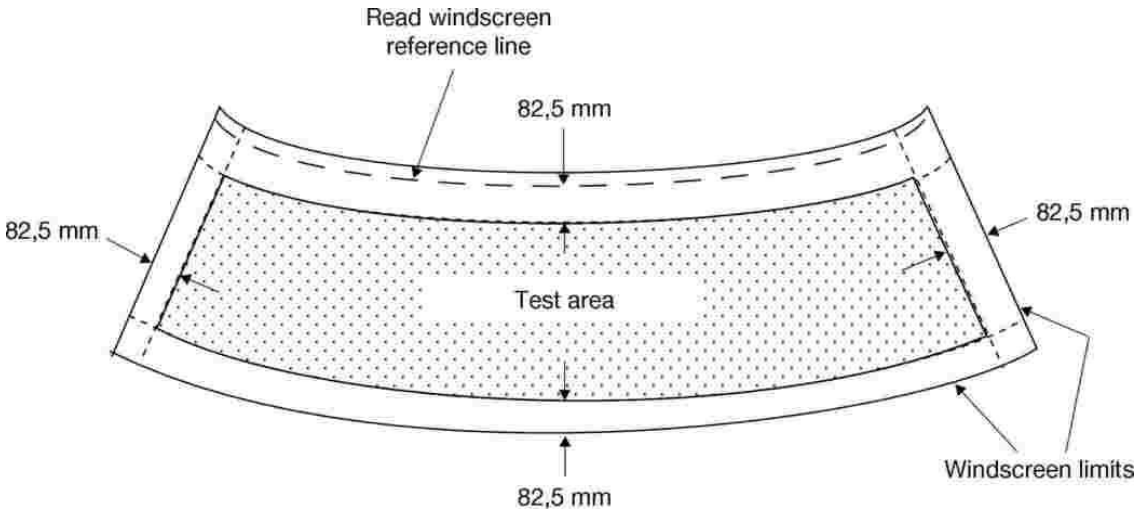

Figure 2-19 – Windscreen impact area. [13]

The test is carried out with an impact velocity of $9.7\ \pm 0.2\ m \cdot s^{-1}$ and the impact angle of $35° \pm 2°$. The effect of the gravity shall be taken into account when the impact velocity and angle are measured at the time before impact. [13]

2.4.3.2 Child and adult headform impactor to bonnet top tests

These tests are conducted on the bonnet top test area. Minimum of nine tests with child headform and nine tests with adult headform are required. For each type of the headform, three impacts shall be targeted to the middle third of the bonnet, the rest of the impacts shall go to the outer two thirds. The impact points are selected to be the most likely to cause the injury. The main difference between the child or adult headform, except the different weight, is the definition of the test areas as illustrated in Figure 2-20.

a) For child headform impactors the test points shall be at least 165 mm apart and a minimum of 82.5 mm from the defined side reference lines. The area is defined in longitudinal direction by a minimum of 82.5 mm backwards of the bonnet leading edge reference line or wrap around distance of 1 000 mm whichever is more rearward. The rear of the test area is defined by a minimum of 82.5 mm forward of the bonnet rear reference line or wrap around distance of 1 700 mm whichever is more forward. [13]

The spacing between impact points and lateral limits of the testing area is the same for adult and for child headform. The difference is in the definition of the area in the longitudinal direction. The reason being that the adult pedestrian is taller than the child pedestrian thus would hit the vehicle bonnet farther.

b) The area is then defined in a longitudinal direction by a minimum of 82.5 mm backwards of the bonnet leading edge reference line or wrap around distance of 1 700 mm whichever is more rearward. The rear of the test area is defined by a minimum of 82.5 mm forward of the bonnet rear reference line or wrap around distance of 2 100 mm whichever is more forward. [13]

The impact points shall be selected in a such way that the impactor would not bounce of the bonnet and hit the windscreen or an A-pillar with much greater effect. If the distance between the test points could not be maintained because the remaining area is too small, less than nine tests may be performed however, the testing laboratory shall execute as many tests as possible to assure the pedestrian protection.

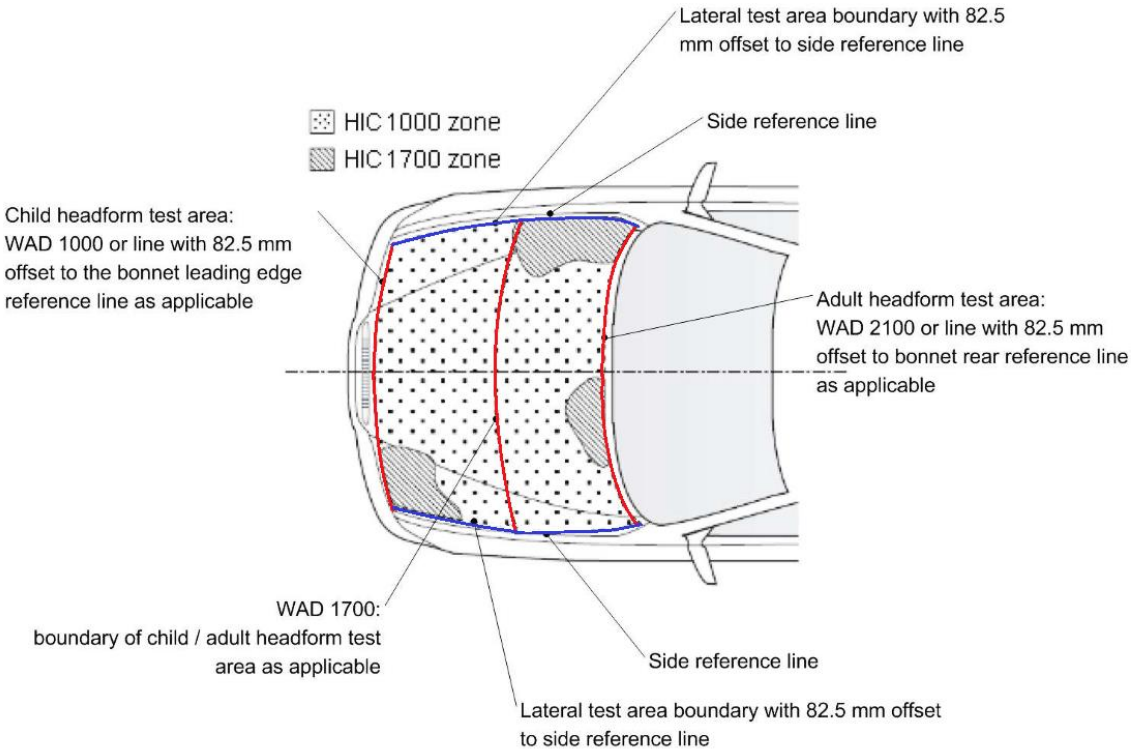

Figure 2-20 – Example of marking of HIC1000 zone and HIC1700 zone with the designation of child and adult headforms impact areas. The figure is edited to better show the zones. [76]

The vehicle manufacturer is obligated to determine the impact zones on the vehicle bonnet top where the head injury criterion shall not exceed 1 000 for HIC1000 zone respectively 1 700 for HIC1700 zone. Marking of these test zones before the experiments is conducted according to the drawing provided by the manufacturer. Drawing shall be as a top view from horizontal plane above the vehicle. This horizontal plane shall be paralleling with the ground reference level. The HIC1000 and HIC1700 zones may be divided into several parts with no restriction to the number of the parts.

The test areas and the HIC value on the vehicle top bonnet are chosen by the manufacturer. Both shall meet the requirements defined in point 3.5 of *Annex I* to *Regulation No 78/2009 of the European Parliament and of the Council on the type-approval of motor vehicle with regard to the protection of the pedestrian and other vulnerable road users*. The HIC criterion shall not exceed 1 000 over one-half of the child headform test area and further on the HIC shall not be greater than 1 000 over the two-thirds of the child and adult headform test area combined. For the remaining areas, the performance of the HIC criterion shall not exceed the value of 1 700 for both headform impactors. [14]

As stated before, the difference while using various headform impactors is not the velocity but the angle of the impact. For the child headform the impacting angle is $50° \pm 2$ and for the adult headform the impact angle is $65° \pm 2°$ [13], both measured in the plane parallel to the ground reference level – see Figure 2-21. This figure also shows the difference between target and impact point due to the spherical shape of the impactor. Impact point on the vehicle means the location of the first contact between vehicle bonnet and impactor outer surface. The target point represents the intersection of the projected impactor longitudinal axis with the surface of the bonnet. The proximity of these two points depends on the initial impact angle and the shape of the vehicle front-end.

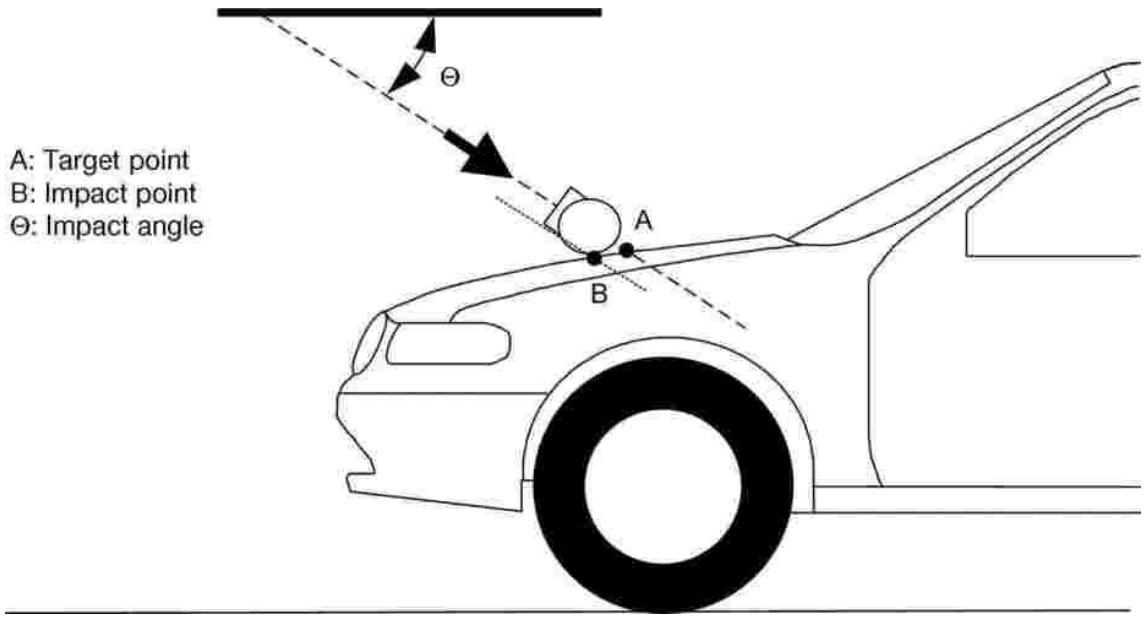

Figure 2-21 – Designation of target and impact points. [13]

Table 2 explains the impact-related parameters for three different settings of headform impactor tests.

Table 2 – Summary of the headform impactor testing [13]

	Child headform to bonnet top test	Adult headform to bonnet top test	Adult headform to windscreen test
Impactor weight $[kg]$	3.5	4.5	4.8
Impact velocity $[m \cdot s^{-1}]$	9.7 ± 0.2	9.7 ± 0.2	9.7 ± 0.2
Impact angle [°]	50 ± 2	65 ± 2	35 ± 2
Impact point location tolerance $[mm]$	± 10	± 10	± 10
Number of tests	9	9	5
HIC limits[5] [-]	$< 1\,000$ $< 1\,700$	$< 1\,000$ $< 1\,700$	1 000
Test temperature $[°C]$	20 ± 4	20 ± 4	20 ± 4
Impact velocity measurement accuracy $[m \cdot s^{-1}]$	± 0.01	± 0.01	± 0.01

[5] The HIC values for both child and adult headforms shall not exceed 1 000 over the one-half of the child headform test area and further the HIC shall not exceed 1 000 over the two-thirds of the child and adult headform test area combined. The HIC for the remaining testing areas shall not exceed 1 700 for child and adult headforms. The recorded HIC value of the adult headform to windscreen tests shall be compared with possible the target of 1 000. [14]

2.4.4 Headform impactors

Use of headform impactors as measurement object within the pedestrian protection tests is defined in *Part V* of *Commission Regulation (EC) No 631/2009 laying down detailed rules for the implementation on the type-approval of motor vehicles with regard to the protection of pedestrians and other vulnerable road users*. [13] In general, the impactor is a spherical rigid object fitted by artificial cover representing human skin. The placement of the skin is important so that the impactor will have similar friction properties as real pedestrian head. For the evaluation of both adult and child pedestrian safety, a child/small adult and adult headform impactors shall be used.

In both cases, the impactors shall be manufactured as a rigid sphere made of aluminium and fitted with the $14.0 \pm 0.5\ mm$ thick skin covering at least half of the sphere. The diameter of the impactor with the skin should be within $165 \pm 1\ mm$. The centre of the gravity of the impactor, including instrumentation, should be identical with the geometrical centre of the sphere. The tolerance for the centre of gravity is different for both types so for simplification the tolerance values are listed in Table 3 together with all the other requirements. [13]

A cavity in the sphere shall allow the installation of one triaxial accelerometer or three uniaxial accelerometers. Those accelerometers are measuring acceleration vs. time history which could be further used to assess the aggressiveness of the impact of the vehicle front part on pedestrians based on biomechanical criteria. Same criterion was presented in chapter 2.3.2. The impactor shall be designed to have first natural frequency over $5\ 000\ Hz$.

The regulation further prescribes the instrumentation parameters. The channel frequency class (CFC) shall be 1000 [13] as defined in ISO 6487:2015. The CFC value indicates, which data filter shall be applied for post-processing of the measured data. Furthermore the channel amplitude class response value (CAC) of the accelerometer shall be $500\ g$. The CAC number is equal to the upper limit of the measurement range [23], [24]. The positioning of the accelerometer for both impactors is illustrated in the following Figure 2-22 and Figure 2-23.

The main difference between the child and adult headform impactor is in weight because in real world the head of the adult pedestrian is heavier. Further differences , like the moment of inertia about an axis through the centre of gravity and perpendicular to the direction of the impact, tolerance of the accelerometer and impactor COG positioning result from slightly different design of the impactors. The specification for both impactors is in Table 3.

To ensure flawless and repeatable performance of the impactors, the certification process described further in the chapter 3.1 of this Thesis. The impactor may be used only for 20 impact tests before re-certification is required and the certification process is obligatory also when the transducer output exceed the specific CAC value. [13]

Table 3 – Headform impactors physical parameters [13]

	Child impactor	Adult Impactor
Weight $[kg]$	3.5 ± 0.07	4.5 ± 0.1[6]
Impactor diameter $[mm]$	165 ± 1	165 ± 1
Skin thickness $[mm]$	14.0 ± 0.5	14.0 ± 0.5
Moment of inertia $[kg \cdot m^2]$	0.008 to 0.012	0.010 to 0.013
Tolerance of the COG $[mm]$	± 2	± 5
Tolerance of the accelerometer positioning[7] $[mm]$	± 10	± 10
Tolerance of the accelerometer positioning[8] $[mm]$	± 1	± 1
CFC value [-]	1000	1000
CAC value $[g]$	500	500
First natural frequency $[Hz]$	5 000	5 000

Figure 2-22 and Figure 2-23 shows cross-sections of both headform impactors. The main difference between these two types is in the cavity size and endplate height. This is due to the specific weight requirements.

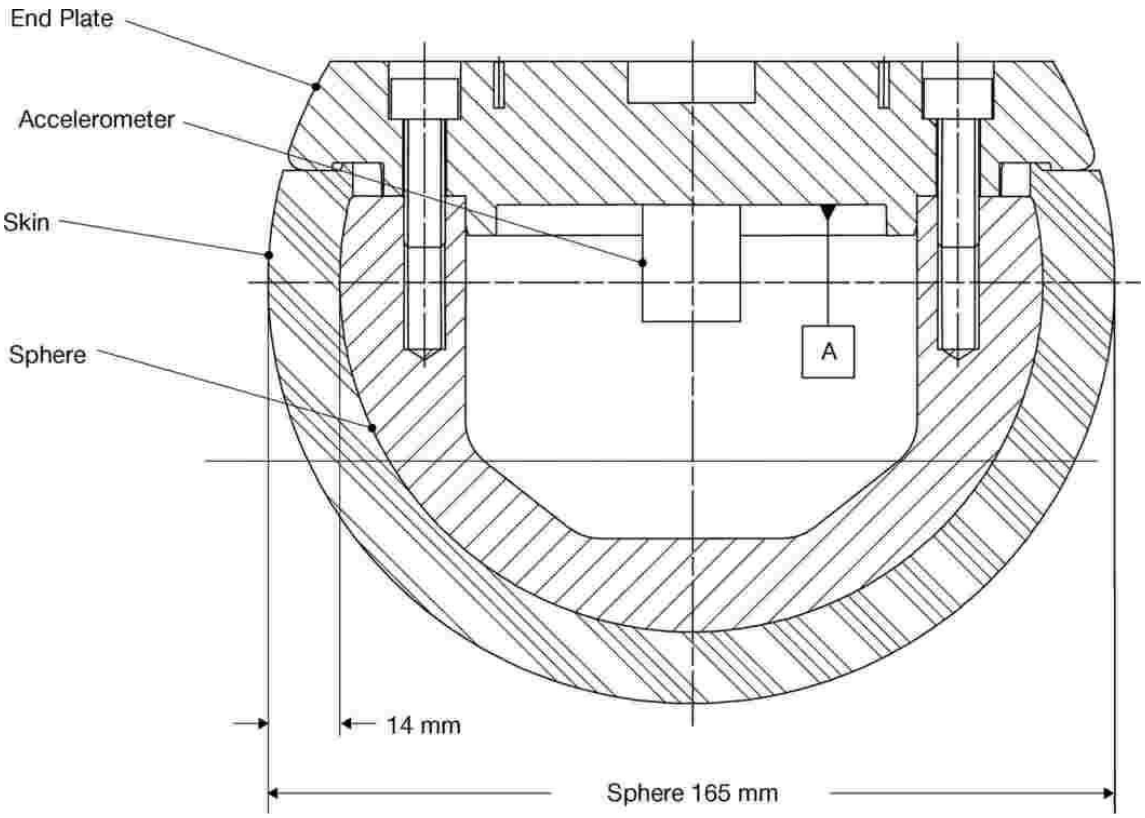

Figure 2-22 – Cross-section of the child headform impactor. [13]

[6] For the purposes of the adult headform to windscreen test, the total impactor mass including instrumentation shall be 4.8 ± 0.1 kg.
[7] Distance between the seismic mass of the accelerometer and COG of impactor for measurement axis.
[8] Distance between the seismic mass of the accelerometer and COG of impactor for the perpendicular direction to the measurement axis.

The endplate is connected to the sphere via bolts and the skin is fitted over the sphere by means preventing the stripping of the skin. The datum base *A* is used for placement of the three uniaxial accelerometers. These days most of the headform impactors are using three uniaxial accelerometers and the more advanced ones are using the wireless connection to acquire measurement data.

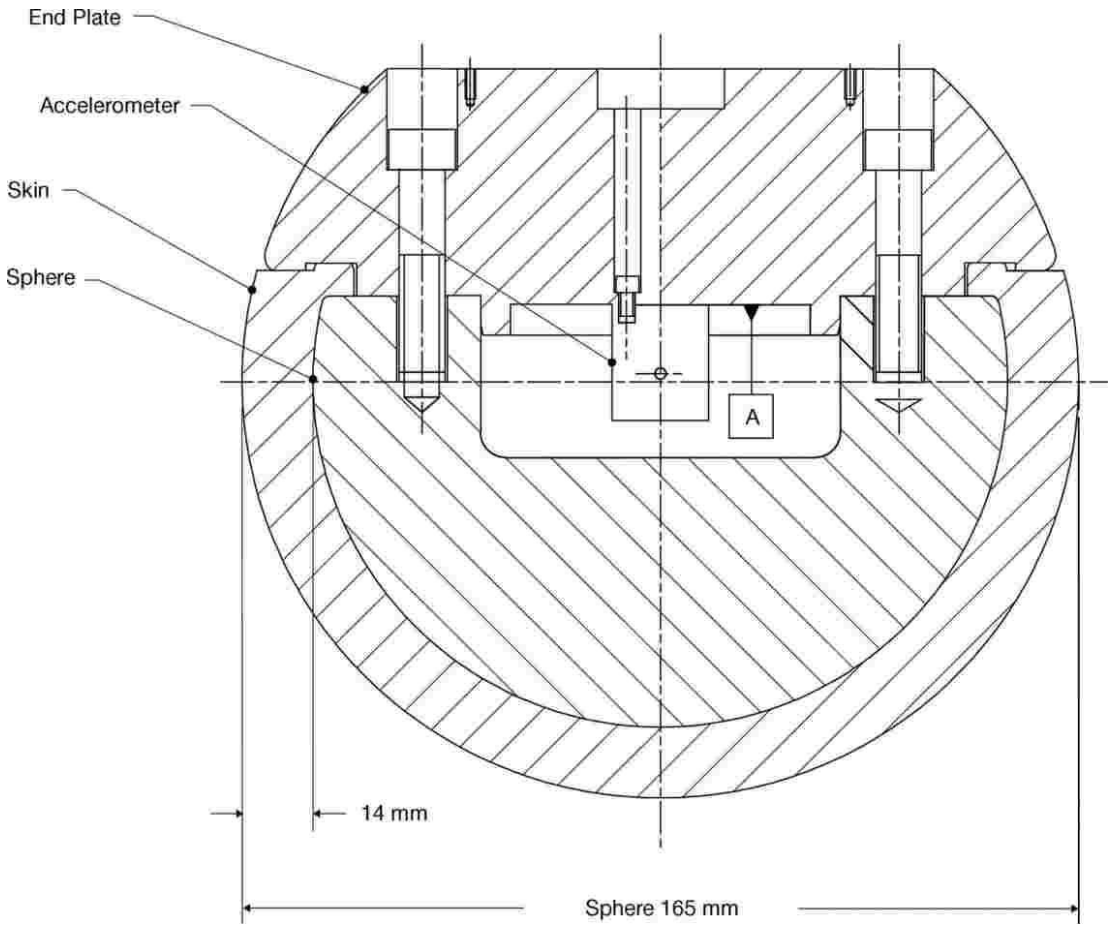

Figure 2-23 – Cross-section of the adult headform impactor. [13]

3 Sensitivity analysis of the selected parameters

3.1 Requirements for the headform impactor dynamic certification test

Headform impactors used in tests described in chapter 2.4.3 shall comply with relevant performance requirements. These requirements are necessary to deliver the sustainable experiment outputs within the laboratory conditions. Dynamic certification test for headform impactors, as like as the pedestrian protection testing procedures, has undergone development over the past years. Older version of this certification test consisted of pendulum impact to the suspended headform impactor. The current execution of the test for certification is performed by dropping the suspended headform onto the rigid desk.

In both cases, the impact is causing a dynamic response, which cause the change of the acceleration. This response is then intended to be within the limits outlined by the standards. This way certified headform impactor may be used for a maximum of 20 impacts before recertification. The impactor must be also recertified at least once during the period of one year and in a case that the transducer output of any impact exceeds the specific CAC (Channel Amplitude Class). The CAC number is numerically equal to the upper limit of the measurement range (for headform impactor tests $500\ g$). According to the actual norms [13] and [3], the dynamic certification test shall be performed as follows.

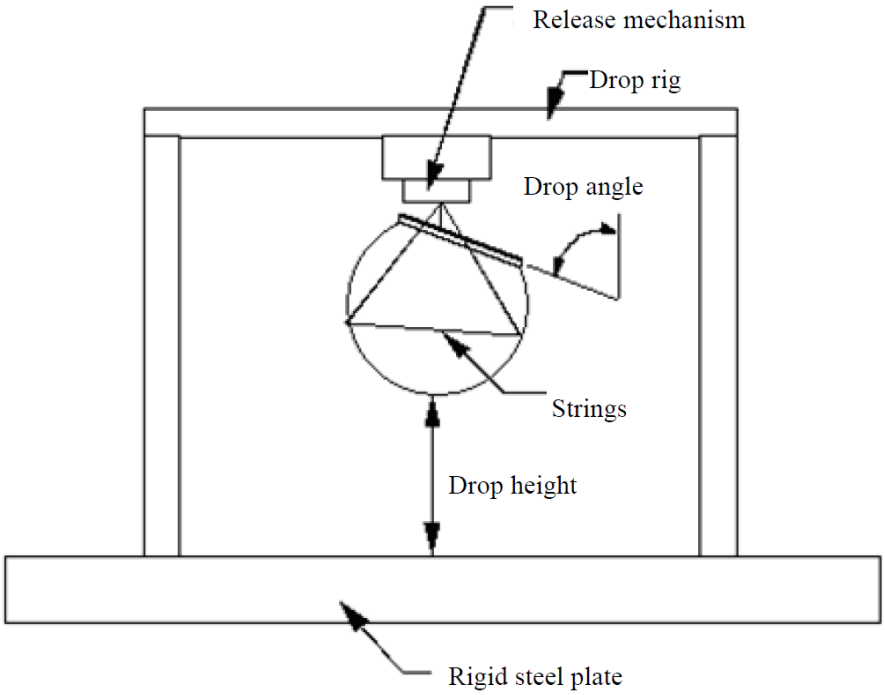

Figure 3-1 – Test set-up for headform impactor dynamic certification. [13]

As illustrated in Figure 3-1 the impactor is suspended from the drop rig at a height of 376 ± 1 mm from the firmly supported rigid plate and shall be equipped by the mechanism allowing immediate release. The headform impactor is then dropped with the rear face at the angle of $50 \pm 2°$ from the vertical for child headform and $65 \pm 2°$ for adult headform. It is required that the suspension attachment shall not allow rotation

during the fall. The rigid plate should be at least 50 mm thick and has the area not less than 300 mm x 300 mm. The surface of this plate should be clean and dry with the surface roughness between 0.2 and 2.0 μm.

To ensure responsiveness and reliable outputs of the certification test it is necessary to perform the drop test at least three times with the headform impactor rotated 120° around its axis of symmetry. The headform impactors shall have the temperature of 20 $\pm$ 4 °C at least 4 hours before the test at a relative humidity of 40 $\pm$ 30 %.

The peak result of the acceleration measured in the centre of gravity of the child headform impactor shall be between 245 g and 300 g and for the adult headform impactor it shall be between 225 g and 275 g. [13]

3.2 FEM simulation of the headform impactor dynamic certification test

Headform impactor dynamic certification test is a basics simulation test needed for further investigation. This virtual experiment is easy to set up and compute and the results obtained from this test offer an extensive source of data for future research. The simulation model was created in finite element pre-processor ANSA and does correspond with the specification described in paragraph 3.1. The FEM model of the impactor used in all simulation is *Adult Head – 4.5 Kg – Version 5A* from company *LASSO Ingenieurgesellschaft mbH.*

To save the computation time and to keep the principles of the correct modelling of FEM simulations there is a different way how to give the impactor required velocity before hitting the rigid steel plate. Instead of dropping the impactor from the height of 376 mm, the impactor is brought closer to the steel plate and accelerated as an initial condition. The distance between impactor and steel plate, is only 1,25 mm, which is the contact thickness In other words, the contact between the rigid plate and outer surface of impactor skin will apply only when these two parts are closer than contact thickness. The initial speed that shall be given to the impactor could be calculated as follows:

The drop height lowered by contact thickness is:

$$z = 376 - 1{,}25 = \mathbf{374.75\ mm} \tag{3.1}$$

With using the common formula for the displacement of linear acceleration motion where g is the gravity of Earth and t is time:

$$z = \frac{1}{2} \cdot g \cdot t^2 \tag{3.2}$$

The initial velocity of the impactor then shall be:

$$v = g \cdot t = g \cdot \sqrt{\frac{2 \cdot z}{g}} = \sqrt{2 \cdot g \cdot z} = \sqrt{2 \cdot 9.807 \cdot 0.37475} = \mathbf{2{,}711\ m \cdot s^{-1}} \tag{3.3}$$

This initial velocity condition is applied to all nodes of headform impactor in the vertical direction.

Figure 3-2 shows the dynamic response of adult headform impactor obtained from the simulation of a dynamic certification drop test. As can be seen, the resultant peak of acceleration is within the tolerance window for the adult headform impactor and therefore this simulated dynamic certification would be considers as valid.

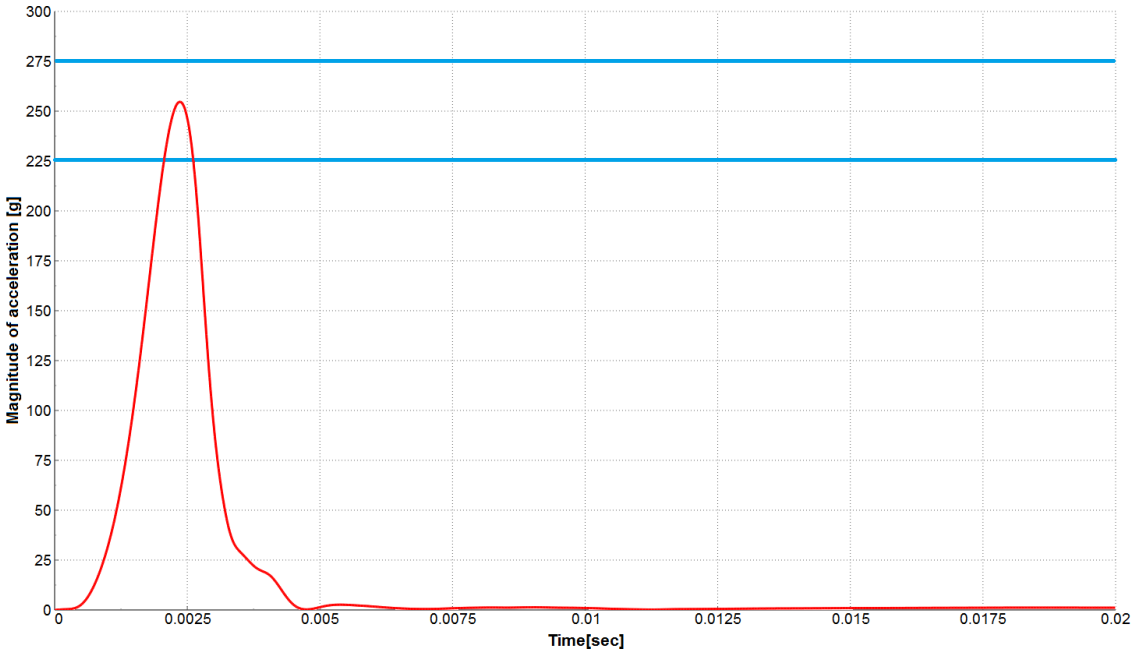

Figure 3-2 – The acceleration vs. time history of the adult headform impactor in dynamic certification drop test simulation.

3.3 Sensitivity analysis

The focus of this analysis is to obtain the essential information about the behaviour of the acceleration curve in case of alternation of the simulation parameters. This study can be used for further determination of simulation parameters that have a considerable influence on the behaviour of results of experiments.

The drop test was chosen as an object for sensitivity analysis because of the simplicity of simulation. The main criterion in the assessment of the outputs from the simulations is the maximum value of resultant acceleration measured in units of g and the sensitivity of standard and relative deviation. Interpretation of the results requires essential understanding that the absolute values of standard and relative deviations are not directly comparable between each other. The range of investigated parameters varies because some parameters need deeper analysis than the others.

3.3.1 Examined parameters and settings

Parameters subject to analysis could be divided into three classes:

- Computational parameters:
  Settings of Property ID (*PID*) of the solid elements belonging to the skin of the headform impactor. Particularly, element formulations could affect computation cost and it is also responsible for hourglass energy

- Material property:
  Settings of material **MAT181 MAT_SIMPLIFIED_RUBBER/FOAM* which describes the material formulation of the impactor skin. The data describing this material were supplied with the FEM model of headform impactor from the company *LASSO Ingenieurgesellschaft mbH*. The investigated property from this section includes bulk modulus, damping coefficient and material density.

- Contact parameters:
  The setting of contact as **AUTOMATIC_SURFACE_TO_SURFACE* between other surface of the impactor and target surface. These parameters contain static and dynamic coefficient of friction and exponential decay coefficient.

Before introducing the individual simulation parameters, it shall be noted that only one parameter was altered at the same time. This decision was taken to investigate the influence of only one specific parameter while the rest of the parameters was left with their default settings.

3.3.1.1 ELFORM – Element formulation

Several approaches can be used to transform the physical formulation to its finite element form. This option could be set for both shell and solid elements. In our case, we altered this setting for property ID of solid elements of the skin. The criterion for comparison was the value of impactor acceleration measured in the centre of gravity, elapsed time and the value of hourglass energy. The used formulations were: [25]

- EQ.-1: Fully integrated, selectively reduced solids intended for elements with poor aspect ratio, efficient formulation

- EQ.-2: Fully integrated, selectively reduced solids intended for elements with poor aspect ratio, accurate formulation

Table 4 summarizes the results. It is obvious that for both element formulation the hourglass energy is zero, acceleration values do not significantly vary and from the perspective of elapsed time, the formulation EQ.-1 is more convenient. Therefore, it was decided to use the element formulation EQ.-1 for all further simulation of the drop test. It shall be emphasized that the results and computational cost will be strongly affected in a case of worse mesh quality.

Table 4 – Comparison of different element formulation

ELFORM	Acceleration [g]	Elapsed time [min]	Hourglass energy [J]
-1	255.23	6:06	0
-2	255.44	8:04	0

3.3.1.2 KM – Bulk modulus

Bulk modulus [26] (in LS-DYNA titled *KM, normally denoted K)* is used to define the material resistance to the volumetric stresses. It can be defined as a ratio between the infinitesimal pressure increase and the resulting relative decrease of the volume. This form is possible to rewrite into the following formula:

$$K = -V\frac{dP}{dV} \tag{3.4}$$

The negative sign before the fraction is used because we assume compression forces. Bulk modulus could be described as an extended form of Young´s modulus and is a measure of how a substance is resistant when undergoing three-axial strain.

To define the range we should investigate the behaviour of simulation and determine which values of Bulk modulus are physically sensible for rubber materials. This definition result from standard elasticity relation between Young's modulus E and Poisson's ratio ϑ according to the [27] and [28]:

$$K(E,\vartheta) = \frac{E}{3(1-2\vartheta)} \tag{3.5}$$

Considering that the headform impactor skin is manufactured from silicone-like rubber, we can define the range of Young´s modulus and Poisson´s ratio from material datasheets. For example, according to the [29] and [30] the standard silicone rubber has a range of Young´s module between $0.01\ GPa$ to $0.50\ GPa$. The Poisson´s ratio for silicone rubber could vary from 0.47 to 0.49.

If we calculate the sensible values of Bulk modulus from the datasheets according to the (3.5) we can get the results within the range from $0.05\ GPa$ to $2.7\ GPa$. Considering that the default setting of bulk modulus for rubber material model in LS-DNYA is $2.5\ GPa$ we could limit the range for investigation to save the iterations. We have adjusted the lower limit of bulk modulus to $1.8\ GPa$ because the more yielding material would not be considered and the upper limit was shifted to $3.2\ GPa$ so we could cover the rubber of higher stiffness.

From plotted results (see Figure 3-3) it is evident that with the increasing Bulk modulus the acceleration values are slightly decreasing. The standard deviation of the acceleration with the variation of the Bulk modulus is $2.59\ g$ and relative deviation is 1.02 %. If we take into account that the Bulk modulus was modified by 28 % from the standard value and the change in resultant acceleration is only 1.02 % we can assume that the variation in Bulk modulus has no significance.

Another sign of how the parameter is influencing the resultant acceleration is the slope of the dependency curve. If we interpolate dependency curve by it's linear regression, we could calculate the slope using the function in MS-Excel. In our case, the linear regression function has a formula with 98% accuracy as follows:

$$y = -5.9508 \cdot x + 270.2 \tag{3.6}$$

The differential of this formula represents the slope of bulk modulus alternation dependence -5.95.

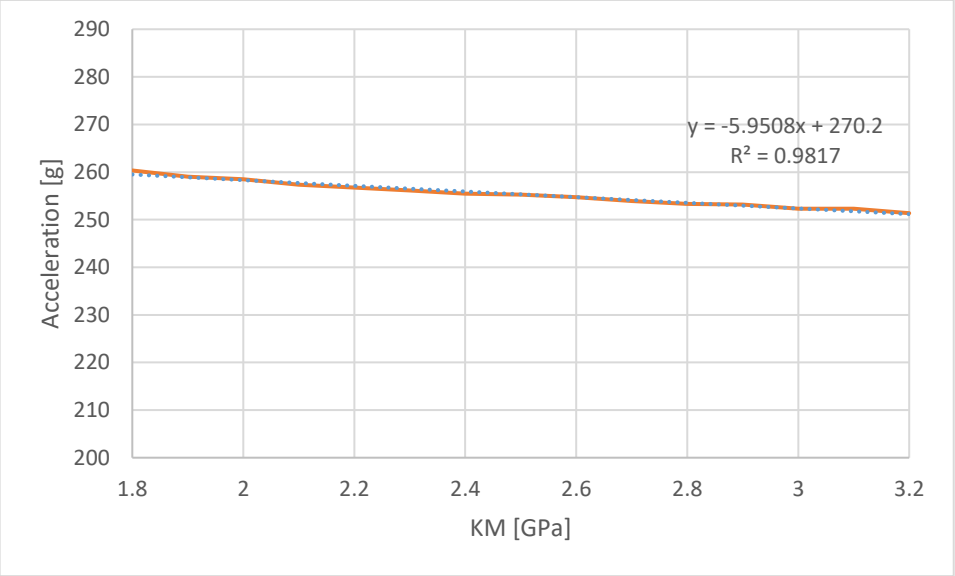

Figure 3-3 – Alternation of the Bulk modulus.

3.3.1.3 MU – Damping coefficient

In general the damping coefficient (in LS-DYNA titled *MU*) is a parameter describing how oscillations of the physical system attenuate after the system is disturbed from the position of static equilibrium. In our case, the damping coefficient is meant as a material property that shows whether a material will rebound or return the energy to the system. This material property is required when we try to evaluate material response to dynamic loading condition. [31]

In FEM applications, the damping can be expressed in several forms. A common type of damping used in the nonlinear analysis of the system assume that the damping matrix C is proportional to the mass and stiffness matrix or that the damping forces are proportional to the kinetic and potential energies of the system. This proportional type of damping is normally referred as a Rayleigh damping. [32] From the definition, the sensible values for damping coefficient must lie within the range of $0 - 1$ where the value 0 is considered for non-damped system and the value 1 represents the critical damping.

To assess the influence of the damping coefficient of the rubber material substituting the skin on the impactor, the damping coefficient was altered within the range from 0.01 to 0.3 with a default setting of 0.1. The resultant dependency can be seen in Figure 3-4. These simulations revealed the expected reciprocal dependence of impact acceleration on the damping coefficient. This tendency could be explained as a consequence of reduction of the bouncing capability of the impactor and consequent reduction of the resultant acceleration.

The standard deviation of acceleration with variable damping coefficient is $20.78\ g$ and relative deviation is $8.42\ \%$. Once more, if we use the linear regression function in MS-Excel, we will obtain the linear function with 98% accuracy:

$$y = -255.64 \cdot x + 280.76 \tag{3.7}$$

Differential of this formula will result in the slope of -225,64. We may declare that the variation of the damping coefficient could significantly influence the deviation of resultant acceleration.

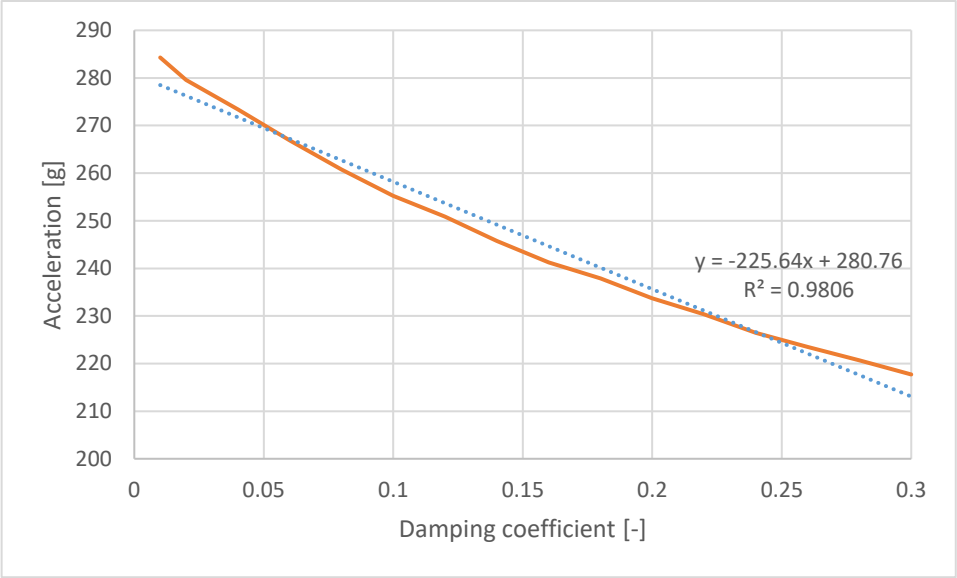

Figure 3-4 – Alternation of the damping coefficient.

3.3.1.4 Density of skin material

Except the deviation of the impact acceleration, the alternation of material density has another consequence.

The regulations, [3] and [13] require that the impactors shall have required weight of 4.5 kg for the adult impactor and 3.5 kg for child headform impactor. If we use the FEM model of the impactor, we should investigate if the density of the material used in the model corresponds to the reality or if the density of some parts of the impactor were manually altered to optimise the impactor assembly weigh.

Another consequence of changing the density of the skin is the relocation the impactor's centre of gravity which, according to the standards, shall be identical with the geometrical centre of the aluminium sphere. With altering the skin density it is necessary to adjust the density of other parts of the assembly to ensure preservation of the standardised conditions. Such modification was realised through the modification of the density of the impactor back-end cover. That also kept the correct weigh of the impactor and the position of its centre of gravity.

Within the sensitivity analysis, we have altered the density of the impactor skin in a range of $\pm 10\%$ to investigate the dependency of resultant acceleration. The default density of the rubber material used in LS-DYNA was $1.186 \cdot 10^{-6}\ kg \cdot mm^{-3}$. The unusual units are a consequence of using kilogram, millisecond and millimetre as standard units in LS-DYNA. Due to the complexity of density variation, only two iterations were simulated and the outcome has proven that only two calculations were sufficient. As illustrated in Figure 3-5, the difference in skin density have almost no effect on resultant acceleration. The standard deviation is 1.38 g and relative deviation is only 0.54 %.

In this case the calculation of the slope of the curve is not necessary because, as shown in the Figure 3-5, the dependency curve is almost flat.

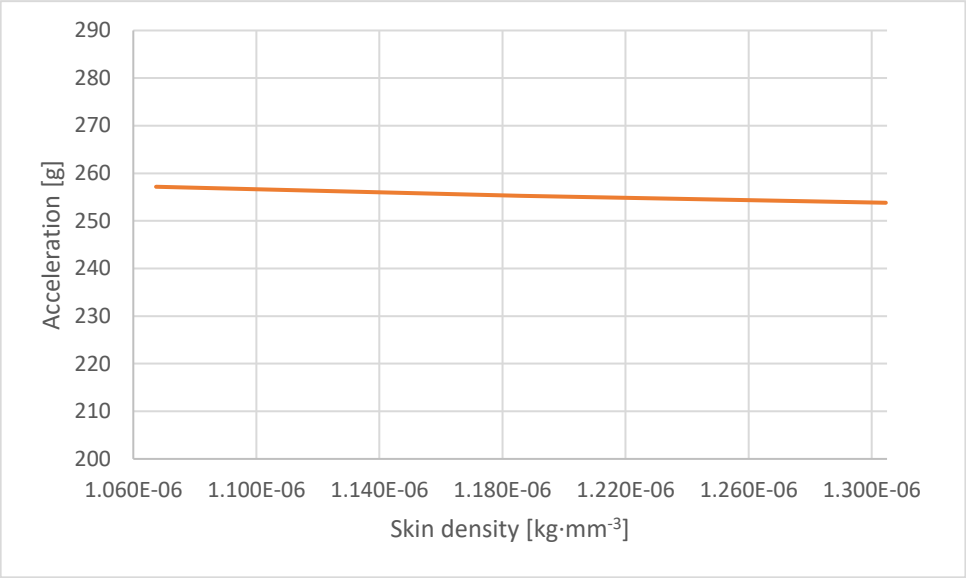

Figure 3-5 – Alternation of skin density.

3.3.1.5 FS – Coefficient of static friction

In further paragraphs we will investigate the dependency of the resultant acceleration on the alternation of some contact parameters. The examined contact is between the outer surface of impactor skin and the target surface. In our case, the target surface is a rigid steel plate where the impactor shall be dropped. This contact is defined in LS-DYNA as **AUTOMATIC_SURFACE_TO_SURFACE* with basic settings of Static coefficient of friction (in LS-Dyna denoted *FS*), Dynamic coefficient of friction (*FD*) and Exponential decay coefficient (*DC*). According to the LS-DYNA Keyword User´s manual [25], the resultant coefficient of friction is assumed to be dependent on the relative velocity v_{rel} of the surfaces in contact according to:

$$\mu_C = FD + (FS - FD) \cdot e^{-DC \cdot |v_{rel}|} \tag{3.8}$$

Static friction will apply when two or more solid objects shall slip on each other but the applying force is not sufficient to generate relative motion [33]. For example, the static friction is preventing a solid from sliding down from the inclined surface. To enable relative motion between any solids a force greater than the threshold for static friction is required to overcome a static cohesion. This threshold could be expressed as follows:

$$F_{ts} = \mu_s \cdot F_n \tag{3.9}$$

where μ_S is a coefficient of static friction and F_n is the normal compressive force. The static coefficient of friction is usually larger than the dynamic coefficient of friction due to the mutual roughness locking mechanisms between the surfaces. The value of the static coefficient of friction depends on the surface roughness of both materials.

In our simulation, the static coefficient of friction was altered in the range between $0.4 - 0.9$ to affect the possible variation of the static coefficient of friction by various rubber materials in contact. From the dependency shown in Figure 3-6 it is clear that with increasing value of the static coefficient of friction, the curve has asymptotic course

towards the constant value. This means that from the value of static coefficient of friction of 0.65 the resultant acceleration is almost constant.

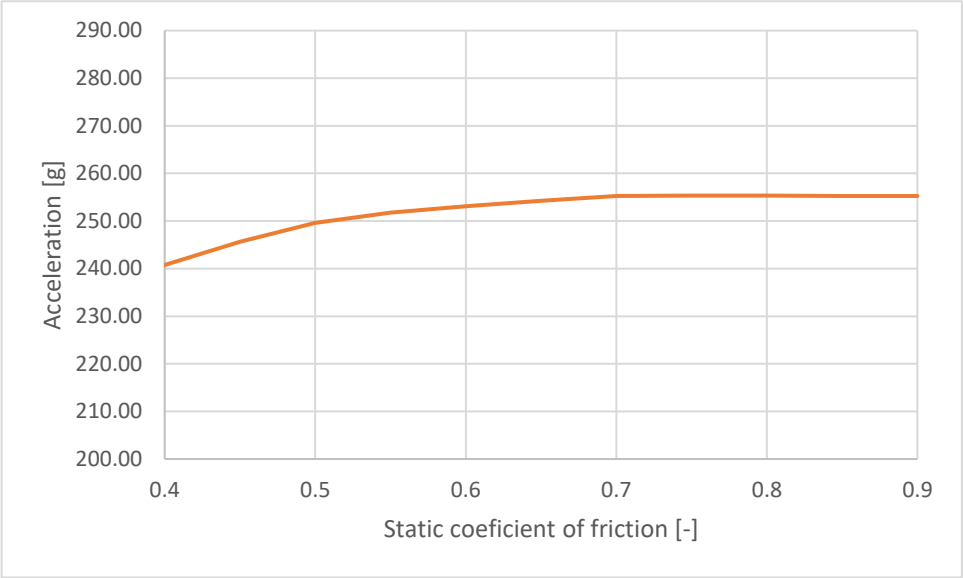

Figure 3-6 – Alteration of the static coefficient of friction.

Standard deviation of the acceleration with altering the static coefficient of friction is 4.59 g and the relative deviation is 1,82%. If we consider that the standard value of the static coefficient of friction appearing between rubber and metal materials could be approximately 0,7 we can assume that the increase of the static coefficient of friction has no considerable influence on the resultant acceleration, the decrease of the static coefficient of friction (for example with better surface finish technology) results in acceleration drop of almost $15g$.

3.3.1.6 FD – Coefficient of dynamic friction

This type of friction apply if two solid materials have relative motion between each other. With the increase of the applied force the threshold preventing the relative motion is exceeded from that point only the dynamic friction became the factor. The dynamic friction force F_{td} between the solid surfaces depends on the normal compressive force F_n according to the following formula:

$$F_{td} = \mu_d \cdot F_n \tag{3.10}$$

where μ_d (in LS-Dyna denoted *FD*) is the coefficient of dynamic friction which is usually less than the coefficient of static friction for the same material. However, some studies [34] mention that the coefficient of dynamic friction could be greater than the coefficient of static friction. The difference is probably caused by definition and understanding of the dynamic friction mechanism. If we consider the friction between two dry metal materials, the chemical bonding between the surfaces will apply rather than interlocking between the surfaces due to their roughness. In contrary in any other application, the roughness effect is prevailing thus the dynamic frictional forces are lower than static frictional forces.

For the evaluation of the influence of altering the coefficient of dynamic friction we have calculated the simulations within the range of 0.4 to 0.9 and the results are expressed in Figure 3-7. From the course of the curve it is evident, that the variation of the dynamic coefficient of friction has no influence on the deviation of the resultant acceleration. The slope of the curve is almost horizontal (constant) thus there is no need to calculate the slope of the function. It shall be also noted that the considered range of the dynamic coefficient of friction was properly chosen because the nearly constant value of resultant acceleration continues before and after the range limits. The corresponding standard deviation value is only 0.18 g and the relative deviation value is only 0.07 %.

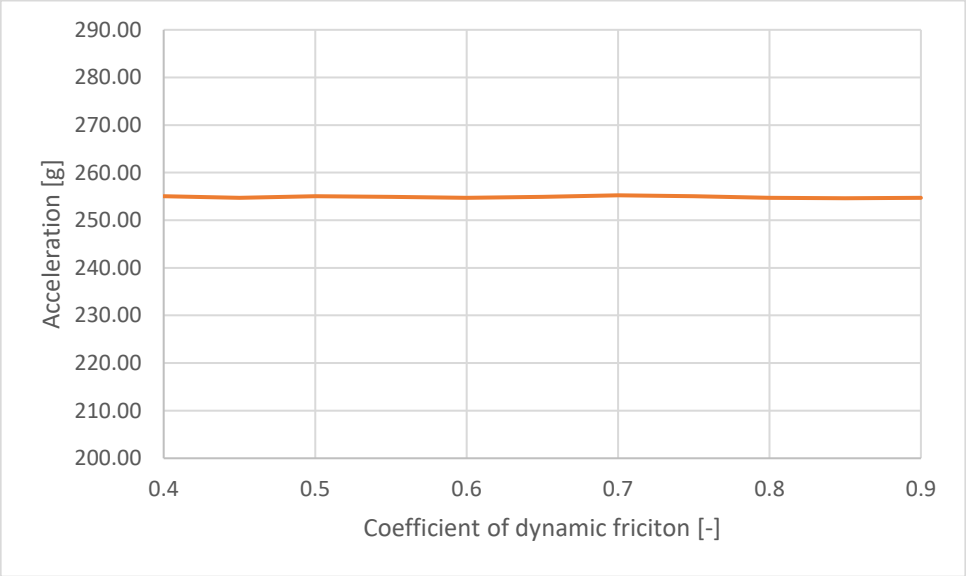

Figure 3-7 – Alteration of the dynamic coefficient of friction.

3.3.1.7 DC – Exponential decay coefficient

Unlike the previous parameters (except element formulation), the exponential decay coefficient is purely the computational parameter and has no physical background. In mathematics, the exponential decay coefficient defines the progress of the reduction of the value by a consistent percentage rate within the defined period.

In general, when two surfaces are brought together closer than the contact thickness defined in the contact settings, the penalisation forces will arise. These penalisation forces are simulating the physical contact reactions of the two surfaces that shall occur and try to separate the two surfaces from each other. Within our application, the exponential decay coefficient helps to specify the transition when two surfaces are moving away from each other and the penalisation forces disappear. The problem arises when the distance between surfaces exceeds the contact thickness and the penalisation forces suddenly cease to exist. It is necessary to avoid such action as it will destabilise the system and cause system oscillations. To prevent this, the penalisation forces shall decrease by exponential curve pre-defined by the decay coefficient. [35]

In a case, that we keep the default setting of the static and the dynamic coefficient of friction of 0.7 the result of the difference using formula (3.8) would be zero and the effect of the exponential decay coefficient will not be taken into account as well as the relative

velocity of the two solids. To avoid this problem, the default setting of the dynamic coefficient of friction was also changed to value of 0.6.

For the assessment of how the exponential decay coefficient influences the results, the variation of that coefficient from 0.0001 to 0.1 was used in calculations and the Figure 3-8 presents its results. It is clear that the resultant dependency of acceleration on exponential decay coefficient is insignificant. This statement is also supported by the values of standard and relative deviations, which are only 0.12 g and 0.05% respectively.

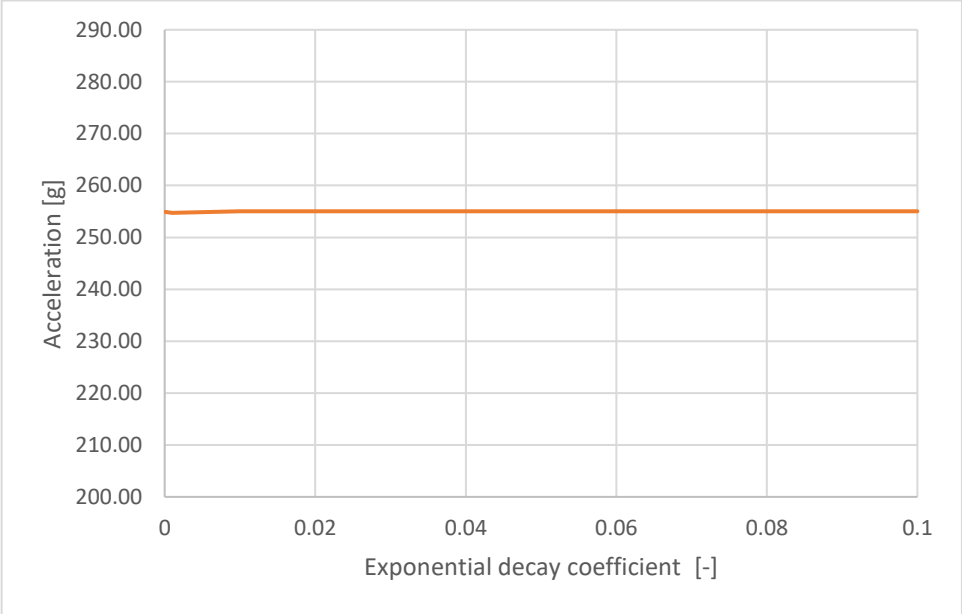

Figure 3-8 – Alternation of the exponential decay coefficient.

3.4 Conclusions of sensitivity analysis

The sensitivity analysis was conducted to evaluate the influence of individual parameter on the resultant acceleration of the headform impactor during the simulated dynamic certification drop test. We have examined the ranges of various parameters to assure the sensible results of acceleration. As a measure of determining if the parameter has a noteworthy influence on the resultant acceleration, the standard and the relative deviation arising from this sensitivity analysis were chosen.

We would like to emphasize again that the absolute values of standard and relative deviations are not directly comparable between each other. To compare two parameters directly we would have to set the identical range for examination. This is not possible due to the different nature of the parameters. Typical example being the research of the influence of Bulk modulus of the used rubber material where the percentage change from the mean value can be assumed to be around 28% from the default setting while e.g. the damping coefficient variation influence can be in a range of -90% to $+200\%$ from the mean value.

One of the reliable means how to compare two or more parameters is to perform the linear regression of the calculated acceleration values and then space the linear function. The slope of this function could be a marker of the impact of variation of the parameter on resultant acceleration variation. However, this approach could be used only for

parameters with the dependency expressed as approximately linear function. The class of accuracy could verify this requirement. In our case, it is reasonable to show only the slope of the alternation of the Bulk modulus and the damping coefficient. The role of the rest parameters is more or less insignificant or the function describing the dependency is not linear.

In Table 5 the investigated parameters are presented together with the range within the simulation were calculated.

Table 5 – Investigated parameters and their range of examination

Parameter	Default value	Lower limit	Upper limit	Investigated range [%]
Bulk modulus [GPa]	2.5	1.8	3.2	$\langle -28; 28 \rangle$
Damping coefficient [-]	0.1	0.01	0.3	$\langle -90; 200 \rangle$
Material density [kg·mm^{-3}]	$1.186 \cdot 10^{-6}$	$1.067 \cdot 10^{-6}$	$1.305 \cdot 10^{-6}$	$\langle -10; 10 \rangle$
Coefficient of static friction [-]	0.7	0.4	0.9	$\langle -42; 28 \rangle$
Coefficient of dynamic friction [-]	0.7	0.4	0.9	$\langle -42; 28 \rangle$
Exponential decay coefficient [-]	0.01	0.0001	0.1	$\langle -90; 99 \rangle$

The following Table 6 shows the resultant acceleration depending on examined parameters together with the mean value of the acceleration, absolute and relative deviations and the slope of the curve sorted decreasingly by the relative deviation.

Table 6 – Results of sensitivity analysis

Parameter	Mean value [g]	Absolute deviation [g]	Relative deviation [%]	Slope [-]
Damping coefficient	246.77	20.78	8.42%	-225.64
Coefficient of static friction	251.95	4.59	1.82%	-
Bulk modulus	255.32	2.59	1.02%	-5.95
Material density	255.40	1.38	0.54%	-
Coefficient of dynamic friction	254.90	0.18	0.07%	-
Exponential decay coefficient	254.93	0.12	0.05%	-

If we set 1% of the relative deviation as a threshold assessing whether the parameter influences the acceleration of the impactor, only damping coefficient, coefficient of static friction and the bulk modulus have fulfilled this requirement. From these three parameters, only the damping coefficient shows significant influence within the reasonable range. The rest of the parameters shows only negligible influence on the acceleration of the impactor during the certification drop test. The effect of damping coefficient could be explained by comparison with the bouncing ball. With the increasing damping coefficient, the ability of the ball to bounce back will decline thus the resultant acceleration will decrease.

In the Annex I of this Thesis the all results of the sensitivity analysis are presented.

Originally, the purpose of this sensitivity analysis was to set the fundamentals for further research of the behaviour of the finite element model of the headform impactor during simulations and experiments. Unfortunately, by the time of writing this Thesis the testing equipment of CTU laboratory of pedestrian protection on Juliska location in Prague was not ready to conduct further experiments. The new headform impactors of the design explained in the chapter 6.3 were not manufactured and the testing device was not fully prepared.

Notwithstanding that fact the results of the analysis described in this chapter can not be further used within this Thesis, they could be a valuable source of information for eventual future research performed by others.

4 Box testing device

The dynamic certification drop test described in chapter 3.1 does not entirely reflect the head impact on actual vehicle components such as the vehicle bonnet or the windscreen. Even though the resultant acceleration peak is similar as in the case of standard headform impactor testing, the rigidity of the real vehicle bonnet is much less than the rigidity of the stiff desk used in the certification process. To evaluate the alternation in impactor's parameters in a form closer to reality, a special box structure was developed to act as an effective substitute of a passenger vehicle front-end.

4.1 The old version of the box testing device

The original version of the box testing device was designed in the year 2004 by the *Research and development department* of *Porsche AG*. From the beginning, a series of tests were performed to assess headform impactors' behaviour but unfortunately, due to the fire, which has destroyed the testing laboratory, the box testing device together with the other laboratory equipment was lost. Following this disastrous event, the activities regarding the box testing device were seized. Fortunately, some of CAE data together with the results of simulations and experiments were restored. Data packet contained the original finite element model which established the foundation for further design and development of the new box testing device.

The old FE model of the box is shown in Figure 4-1. This model was restored only as an output file from the simulation. Because of that, the original geometry of the model is unfortunately lost.

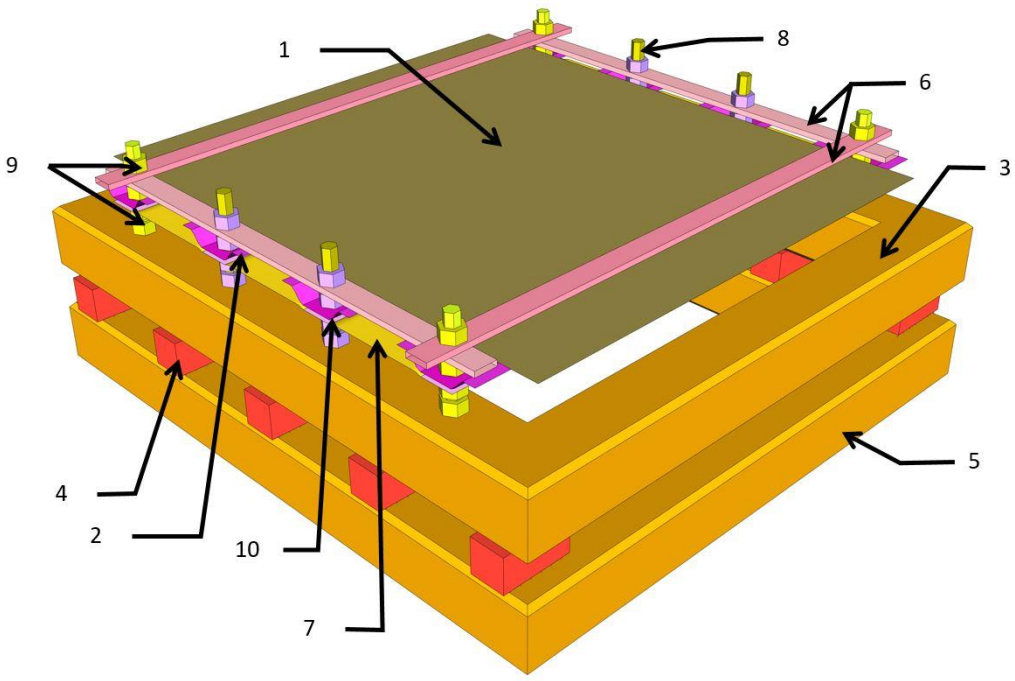

Figure 4-1 – The description of the old box testing device.

***1** – Testing plate (specimen); **2** – Trapeze profiles; **3** – Upper frame; **4** – Middle profiles; **5** – Lower frame; **6** – Lateral and longitudinal support bars; **7** – Trapeze profiles support; **8** – Threaded rods; **9** – Tightening nuts; **10** – Square washers*

The fundamentals of the device are two frames (3;5) made of square cross section hollow profiles welded together via inserted smaller square middle profiles (4). The lower frame (5) is ought to be connected to the laboratory floor by dovetail grooves. The upper frame (3) has eight through holes with inserted threaded rods (8) with a diameter of $20\,mm$. These threaded rods are there to press the assembly of the testing plate (1) together with the trapeze profile (2) against the trapeze support bars (7) by using five sets of tightening nuts (9). To ensure better pressure distribution and to create the elevation between the support bars and trapeze profiles, the square washers (10) underneath the trapeze profiles are used.

Positioning and the usage the nuts is obvious from Figure 4-2. When proceeding the description in the bottom-up direction the first set of nuts (9.1) is connecting threaded rods to the upper frame. Second two nuts (9.2) are squeezing the trapeze profiles against the square washer and further on to the trapeze support bars while the uppermost nut (9.3) is compressing the lateral and longitudinal supporting bars (6). The connection between the testing plate and trapeze profiles is realized by spot welds represented by green squares in the following Figure 4-2.

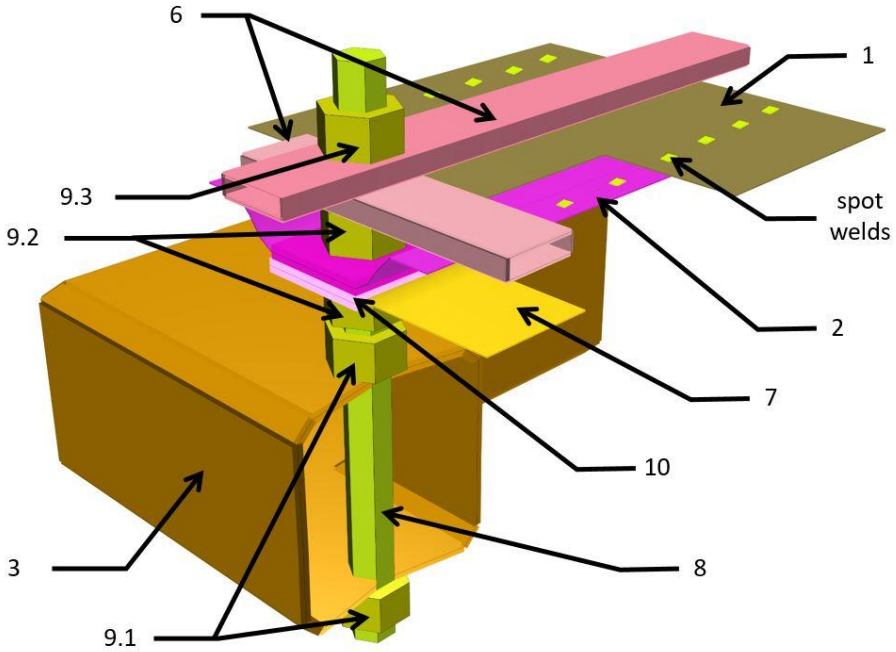

Figure 4-2 – Detail of connection. Some entities of the model were hidden to show more details. Shell element thickness mode is shown in terms of better readability.

***1** – Testing plate; **2** – Trapeze profiles; **3** – Upper frame; **6** – Lateral and longitudinal support bars; **7** – Trapeze profiles support; **8** – Threaded rods; **9** – Tightening nuts, **10** – Square washer*

As stated before, this testing device was originally intended to study the behaviour of the headform impactors. Since some variants regarding the testing device were important for the evaluation, a sensitivity analysis of the individual parameters was conducted with varying some of the experimental initial conditions and the design of the testing device. The experiments were conducted with both types of headform impactors and the altered experimental parameters are listed below together with brief conclusions of the former research done by the *Porsche AG.*

- The thickness of the testing plates - for steel testing plate the variants were 1.00 *mm* or 0.75 *mm* thick. As expected, the thicker plate caused greater acceleration response.

- The angle of impact – for the evaluation purposes the angle of the impact was altered in a range of 25° to 60° for child headform impactor and in a range of 50° to 90° for adult headform impactor. The increase of the angle of the impact cause the increase of the resultant acceleration.

- The usage of eight or four threaded rods – as explained in Figure 4-1 and Figure 4-2 the threaded rods are used to hold the assembly of the testing plate onto the rigid frame. Originally, eight threaded rods were used – four in each of the two lateral sides. To reduce the number of parts and to simplify the assembly of testing plates only four threaded rods in each corner were used. Even though that the resultant acceleration was not higher due to the more flexible structure, the four-point mounting of the testing plate was less favourable because it resulted in larger differences in the comparison between the experiments and the simulations.

As stated before, the FE model of the box device was recovered only as an input key file. Such type of files is used when we want to export finished finite element model from pre-processor to FEM solver (in this case LS-Dyna).

For the future progress, it was necessary to rebuild the headform impactor simulation with the old design of the box and then try to adjust the modification for a newer design. Rebuilding of the simulation included mainly addition of the actual version of the FE headform impactor model, setting its initial velocity and the angle of impact, setting contact definition between testing plates and impactor skin, adding the load of Earth´s gravity and at last setting the control and define cards for computing of the simulation.

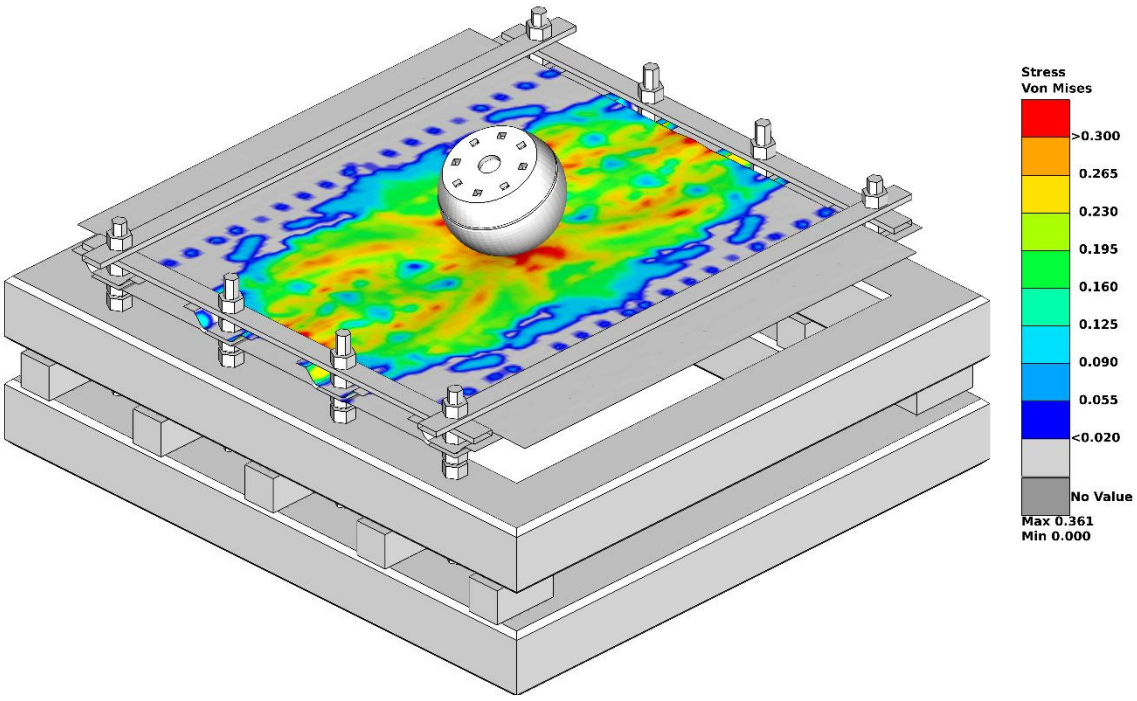

Figure 4-3 – Snapshot of simulation post-processing at the moment of maximum acceleration. The fringe colors is showing Stress Von Mises in units of GPa.

The preview of the simulation results is illustrated in Figure 4-3. The headform impactor used is *Adult Head – 4.5 Kg – Version 5A* from company *LASSO Ingenieurgesellschaft mbH* with the initial velocity of 40 $km \cdot h^{-1}$ and the impact angle of 65°.

The acceleration sensor is substituted in simulations by the possibility of recording multiple values in the specific nodes or nodes sets. For the purposes of evaluation of the simulation, we were recording acceleration values in the impactor´s centre of gravity. The tool used for post-processing of simulation was software Meta post-processor.

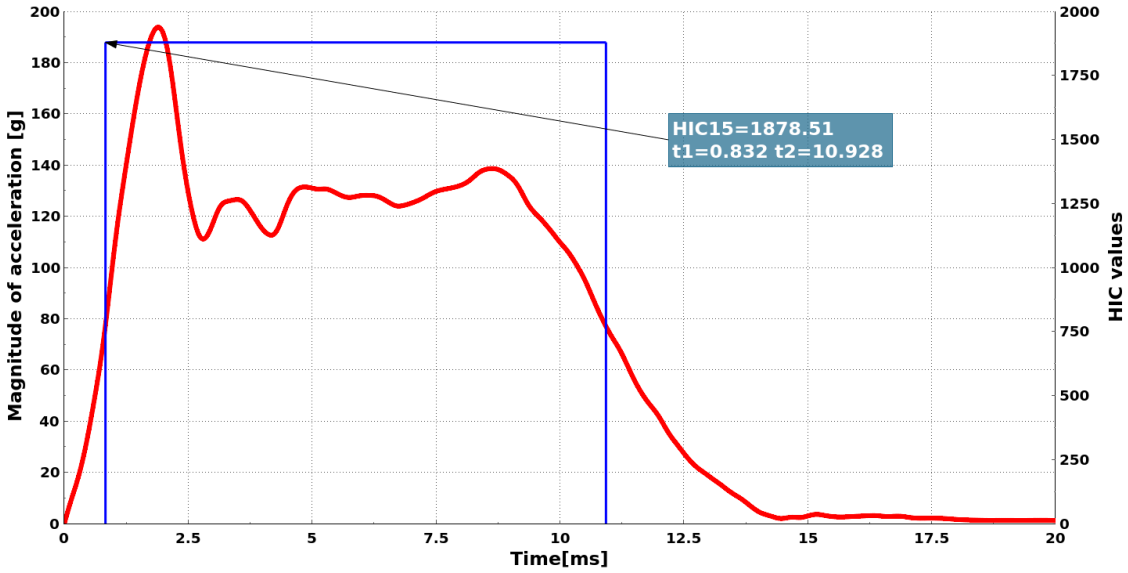

Figure 4-4 – Magnitude of acceleration vs. time history of adult headform impact derived from the original design of the old box testing device.

On secondary axis is shown the HIC value which precise value is shown in the blue text box.

After the assessment of the recorded data it was possible to show a magnitude of acceleration versus time history – the most important dependence for the overall assessment. Before calculating the HIC value it was necessary to convert units for acceleration from $mm \cdot ms^{-2}$ to g. Figure 4-4 shows the results of the first simulation. Red line represents the filtered[9] magnitude of acceleration in units of g measured in impactor´s centre of gravity. The blue box represents the time window, in which was the HIC value calculated. The secondary axis is showing absolute values of HIC.

[9] Using an ISO 6487 Channel Frequency Class 1000 filter

4.2 Modification of the old box testing device design

When the *R&D Centre* of the *Porsche AG* was developing the old testing device, the effort has been concentrated on adjustment of the resultant acceleration course as close as possible to the authentic acceleration response on real vehicles. This was particularly made by using trapeze profiles similar to the actual inner panel of the vehicle bonnet.

The next step for us was to optimize the old box testing device design. The target was to reduce the weight of the box assembly and also simplify the construction while preserving the acceleration curve course and other structural properties. The procedure consisted of modification the old box FE model design in pre-processor Ansa. The adjustments in any other CAD software were not possible due to loss of the model geometry. We've found that adjustments made in Ansa were sufficient even though the changes were done only at the level of finite element entities.

Each of these modifications was independently assessed and compared with the original acceleration curve to evaluate the design adjustments and FE model settings. For every modification described below the comparison with the base model is shown. The magnitude of acceleration curve of the base model is coloured red every time.

4.2.1 Pre-stress in the threaded rods

This modification is not focused on box design but the settings of the finite element model. Originally the testing plate assembly was connected to the box frame via **CONTACT_TIED_NODES_TO_SURFACE_OFFSET* applied on nuts sets *9.1; 9.2* and *9.3* as illustrated in Figure 4-2. In this type of contact, the slave nodes of one part are attached the selected master surface of another part. Figure 4-5 is illustrating the contact principle. At the start of the simulation, the nearest maser entity for every slave node is detected based on an orthogonal projection of the slave node to the master surface [36]. The red circles are representing the tied slave nodes of the tightening nuts and the orange segment is master surface of the trapeze profile. One of the disadvantages restricting usage of this type of contact within our model is a firm connection between the two parts. In reality, the contact between parts in the box assembly is created via axial compressive force arisen from tightening torque applied to nuts. The absolute value of compressive force together with the friction coefficient is preventing slippage of the two surfaces on each other. When we apply the tied nodes to surface, we can restrict the movement of two concerned surfaces without using any pre-stress in the threaded rods. As a consequence, we would not be able get the exact value of tightening torque needed to prevent the slippage during the real experiment.

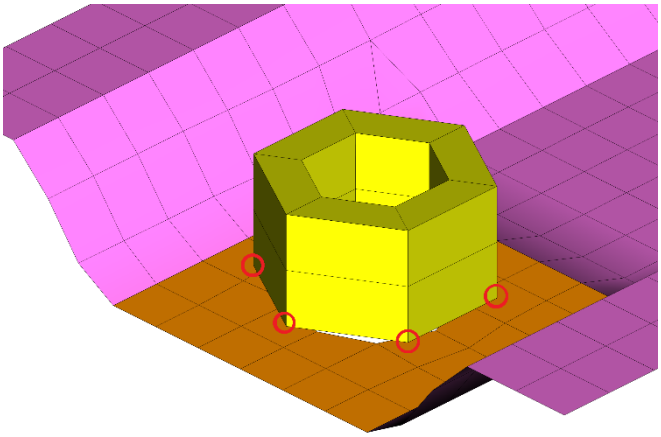

Figure 4-5 – Tied nodes to surface contact.

One possible reasons why this type of contact was used is the low computational cost because the approach with pre-stress is more advanced thus, more difficult to compute.

The philosophy of modelling preload in Ansa consists of three steps. First one is to create cross-sections through the parts where the pre-stress shall be applied. In our case three cross-sections of the threaded rods were created between the nuts *9.1*; *9.2* and *9.3* as illustrated in Figure 4-2. Second step is the creation of the sets where the pre-stress will take place. In our application, this set contains the PID of threaded rods. That approach assures that the preload will be affecting only the threaded rods and no other parts in the cross-section. The last step is creation of the pre-stress loading curve. This special treatment shall be considered when applying the value of the preload. If we would set the stress to its nominal value with imminent effect it might lead to an oscillation of the system as a consequence of shock waves. To avoid this complication, the load curve is used to assure that the preload is gradually increasing in a time period of $1\,ms$ and afterwards the stress value in threaded rods became constant throughout the whole simulation.

4.2.1.1 Pre-stress calculation

The definition of the pre-stress value is necessary to set up the simulation and also further on for computing the tightening torque to be applied in the assembly of the testing plate onto the upper frame. The first step was estimation of the axial compressive force. This was conducted using the internal company (non-published) document concerning the axial forces Q and tightening torques M_k depending on the bolt diameter and bolt strength grade. According to this document, for the metric thread $M20$ with standard pitch $2.5\,mm$ and the material grade 8.8 the preload axial force shall be $73\,000\,N$. Bearing in mind that such great force will need to be used for other, more dynamically exposed, applications, it will be sufficient to lower the axial force by one order to $7\,300\,kN$. In time of post-processing of the simulation we may assume that the frictional force as a consequence of axial force is sufficient to prevent the slippage. Restricting the movement of the trapeze profiles is necessary to eliminate the shear effect and consequent damage of the threaded rods.

To achieve the reliable values for stress and tightening torque it is important to determine the pitch diameter d_2 and minor diameter d_3 of the metric male thread *M20*. According to the pocket-book of Mechanical engineering [37] and the thread geometry table (available online [38]), the required diameters are as follows:

Table 7 – M20 male thread geometry

Pitch $[mm]$	Major diameter $[mm]$	Pitch diameter $[mm]$	Minor diameter $[mm]$	Half of the thread angle [°]
$P = 2.5$	$d = 20.000$	$d_2 = 18.376$	$d_3 = 16.933$	30.000

For the calculation of the compressive stress in the threaded rods, we can use the known formula of the theory of solid mechanics [39]:

$$\sigma = \frac{Q}{A} = \frac{Q}{\frac{\pi \cdot d_3^2}{4}} = \frac{7\,300}{\frac{\pi \cdot 16.933^2}{4}} = \mathbf{32.4\,MPa} \tag{4.1}$$

This value need to be converted into 0.0324 because the Ansa pre-processor is set to work with millimetre, kilogram millisecond thus the unit for stress are gigapascals.

4.2.1.2 Tightening torque calculation

Another parameter important for the execution of the experiments is the tightening torque to be applied while assembling the testing device. For determination of its value we can utilize formulas describing the geometry of the metric thread illustrated in Figure 4-6. At first, with knowledge of pitch, pitch diameter and the number of threads (helixes) is possible to determine the lead angle γ: [39]

$$\gamma = \arctan\left(\frac{i \cdot P}{\pi \cdot d_2}\right) = \arctan\left(\frac{1 \cdot 2.5}{\pi \cdot 18.376}\right) = \mathbf{2.48}° \tag{4.2}$$

where P stands for the thread pitch, i is the number of threads in case of using multi-start threads and d_2 is the pitch diameter. The second geometrical parameter is a conversion of the thread angle to the normal plane β_N: [39]

$$\beta_N = \arctan(\tan\beta \cdot \cos\gamma) = \arctan(\tan 30° \cdot \cos 2.48°) = \mathbf{29.98}\,° \tag{4.3}$$

where angle β is representing the half of the thread angle.

The last required input for calculating the torque is the friction angle φ' in a wedge-shaped groove: [39]

$$\varphi' = \arctan\left(\frac{f}{\cos\beta_N}\right) = \arctan\left(\frac{0.15}{\cos 29.98}\right) = \mathbf{9.82}° \tag{4.4}$$

the variable f stands for the friction coefficient of the steel threads – their value could be estimated in accordance with [37] and [40].

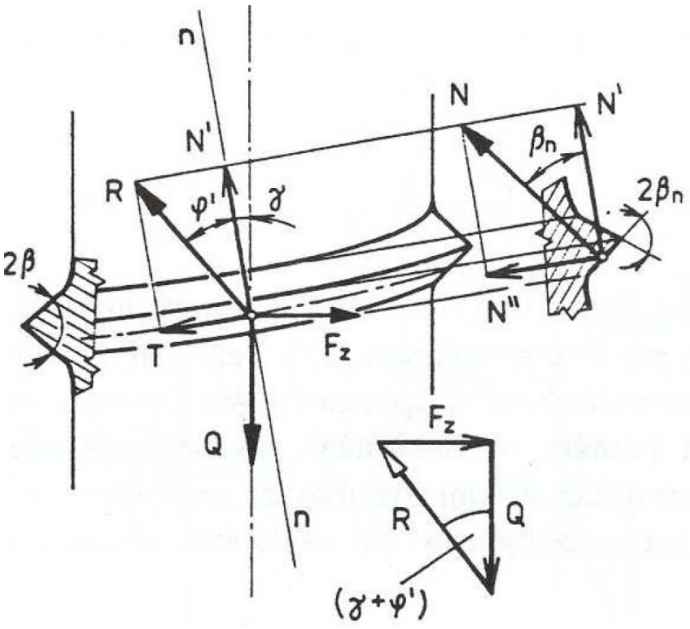

Figure 4-6 – Geometrics and force analysis of the metric thread with cross-sections in the normal and axial planes. [39]

***Q** – axial force, **T** – frictional force, **N** – normal force, **R** – resultant force, **F_z** – tightening force, **β** – thread angle, **γ** – lead angle, **φ'** – frictional angle*

The total tightening torque M_k is composed of the frictional torque in the thread pair M_{kt} and the frictional torque underneath the nut M_{kn}. With knowledge of all of the required geometrical parameters, the frictional tightening torque in the thread is possible to be calculated: [39]

$$M_{kt} = Q \cdot \frac{d_2}{2} \cdot \tan(\gamma + \varphi') = \\ = 7\,300 \cdot \frac{18.376}{2} \cdot \tan(2.48 + 9.82) = \mathbf{14.63\ Nm} \tag{4.5}$$

The frictional tightening torque underneath the nut is depending on the frictional coefficient f_n between the nut and the connected surface and on the frictional radius ρ_n.

The friction coefficient between the nut and connected surface shall be slightly less than the friction coefficient within the thread. This is due to the lesser surface roughness as a consequence of a better surface finish. According to the [39] and [37], the friction coefficient underneath the nut for steel materials should be around $f_n = 0.1$. The friction radius could be set as three-quarters of the pitch diameter [39]:

$$\rho_n = 0.75 \cdot d_3 = 0.75 \cdot 18.376 = \mathbf{13.782\ mm}. \tag{4.6}$$

The formula for determination of the frictional torque underneath the nut is following: [39]

$$M_{kn} = Q \cdot f_n \cdot \rho_n = 7\,300 \cdot 0.1 \cdot 13.782 = \mathbf{10.06\ Nm} \tag{4.7}$$

The minimal tightening torque to overcome the friction arising from assembly of the box device is a sum of both frictions torques:

$$M_k = M_{kt} + M_{kn} = 14.63 + 10.06 \approx \mathbf{25\ Nm} \tag{4.8}$$

Tightening torque $M_k = 25\ Nm$ is the lowest value available to achieve the required pre-stress of $\sigma = 32.4\ MPa$. In reality, the friction coefficients might be different and the other circumstances may appear , both leading to increase of the tightening torque.

4.2.1.3 Results

During the post-processing of the simulation the attention has been paid to check whether the trapeze profile is not slipping against the square washers. The slippage would mean that the value of pre-stress was not sufficient therefore the frictional force is lower than the deformational forces arisen from the headform impact. We came into the conclusion that the axial force in the threaded rods was adequate and the slippage was restricted.

The comparison between the magnitude of acceleration of the base model (red line) and the pre-stressed model (light blue line) is shown in Figure 4-7. Although the maximal peak of acceleration is lower, the subsequent course of acceleration is slightly higher. This is the reason why the resultant HIC value increased from 1878.51 to 1902.81, in percentage increase by 1.29 %. As a conclusion it was decided that for the new design of

the box device FE model the pre-stressed approach will be used as more actual, advanced and accurate approach to modelling. Notwithstanding the fact that the pre-stressed model will be used further on, the other modifications described below use the originally tied nodes to surface contact.

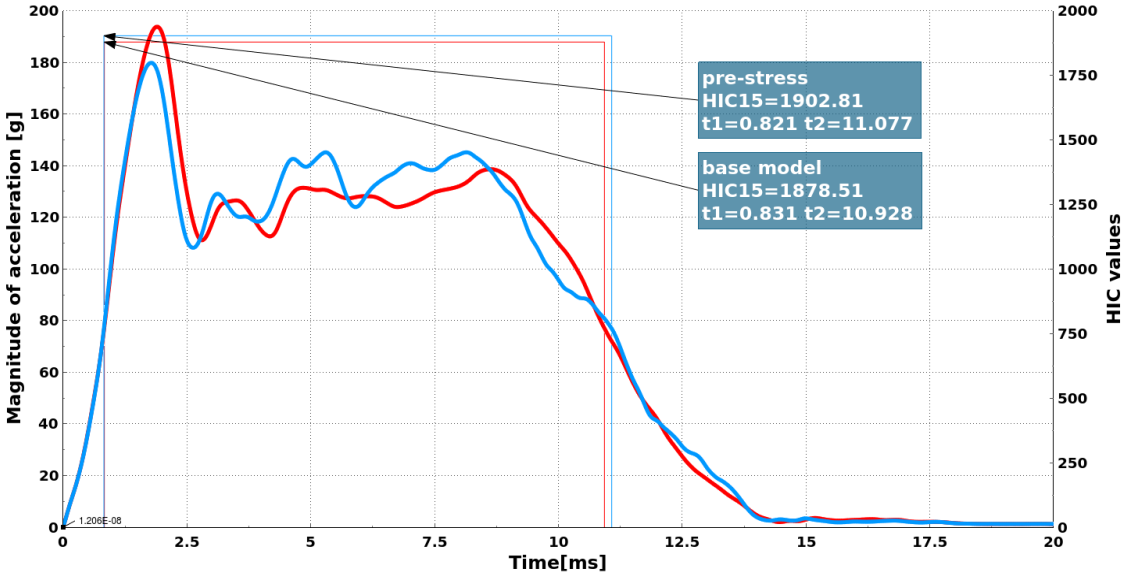

Figure 4-7 – Comparison between the magnitude of acceleration cures of the base model (red) and the model using pre-stress (light blue). The HIC value is increased by 1.29 %.

The subsequent modifications are concerning only the alternation in the box geometrical design. For more adequate comparison of the other modifications with the base model, the preservation of all FE entities, such as contacts, is relevant.

4.2.2 Modification I

The first idea of how to simplify the old box design was to reduce the number of used parts for fixing of the testing plates to the box frame. From the inspection of the simulation results it was evident, that threaded rods (in Figure 2-1 titled as number 8) are unnecessarily long. The decision taken was than to reduce their length and position the bottom surface of the trapeze profiles (2) directly onto the upper frame (3) while preserving the benefits of square washers use. Such design modification made the trapeze profiles support bars (*7*) redundant. All other geometrical parameters and FE model settings remain intact as like as in the case of the base model.

The final design of this modification is illustrated in Figure 4-9.

The comparison of the acceleration curves is illustrated in Figure 4-8. It could be noticed that the first peak, corresponding to the first contact of the impactor and the testing plate, is identical with the base model however at 2.5 ms the acceleration curves split. This phenomenon is a consequence of the design change. As the impactor is deforming the testing plates, the trapeze profiles are bending towards the centre of the testing device. Because we placed the trapeze profile directly onto the frame the deformed profile is leaning towards the frame edge radius, as shown in Figure 4-10. Logical result is than that the stiffness of the profile is increasing.

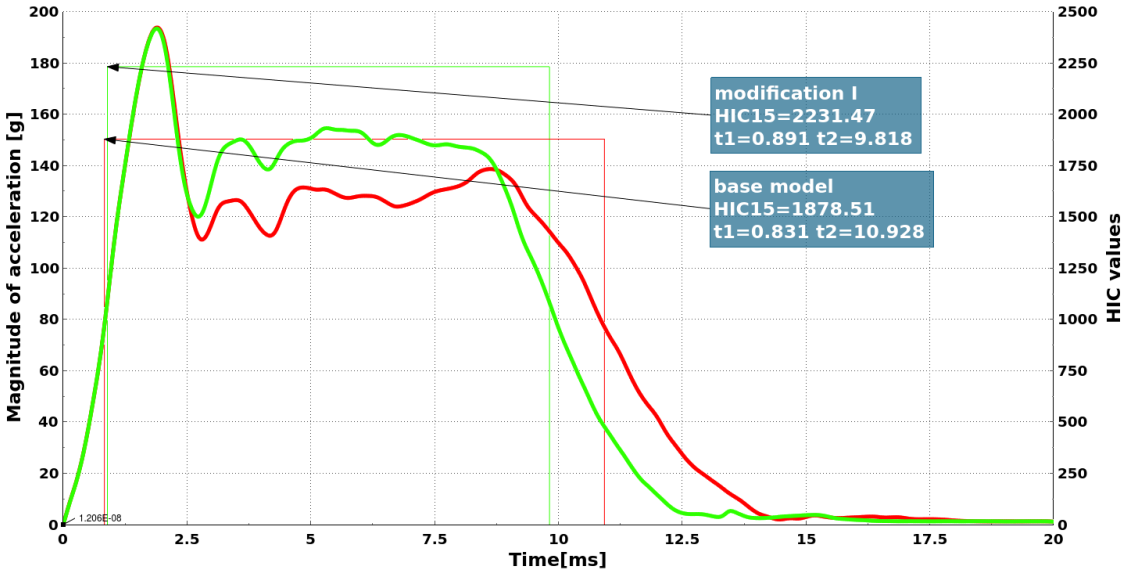

Figure 4-8 – Comparison between the magnitude of acceleration cures of the base model (red) and the modification I (green). The HIC value is increased by 18.78 %.

The elevation created by the square washers is not sufficient to prevent such leaning to happen. Because the structure is now more rigid, the deformation of the testing plate is limited thus the impactor shall experience a greater acceleration within the same period of time. Another implication is that the HIC has increased to a value of 2231.47 which is a percentage change of +18.78% in contrast to the base model.

The leaning of the trapeze profile and subsequent increase of the HIC values is unacceptable therefore the following modifications were realized.

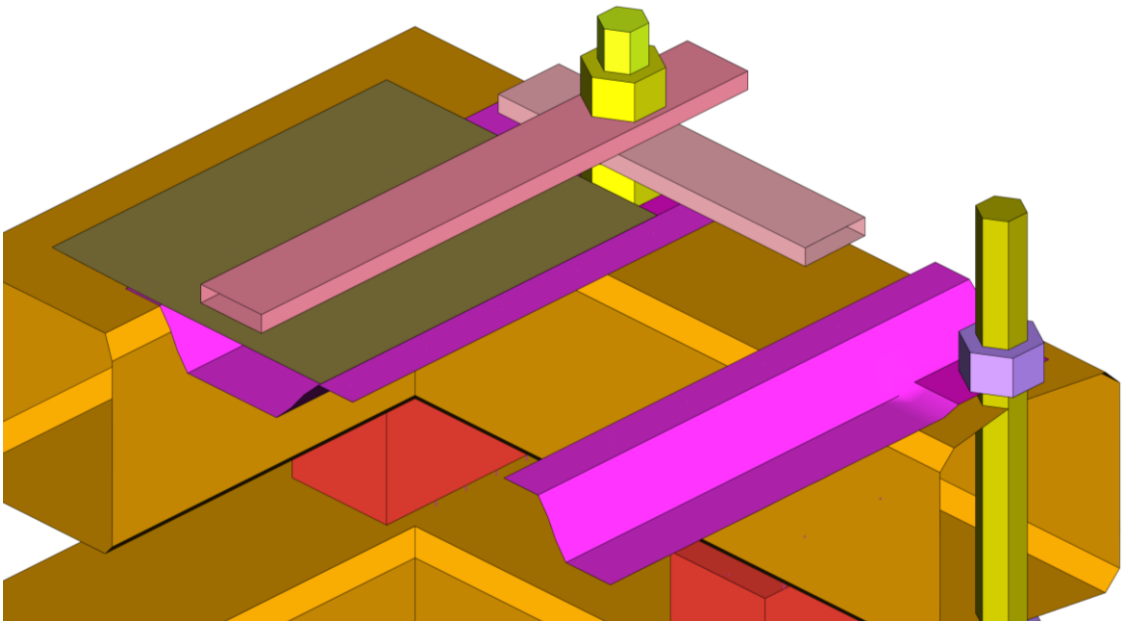

Figure 4-9 – Illustration of the modification I design. The trapeze profiles are placed directly to the upper frame. Some of the entities are hidden.

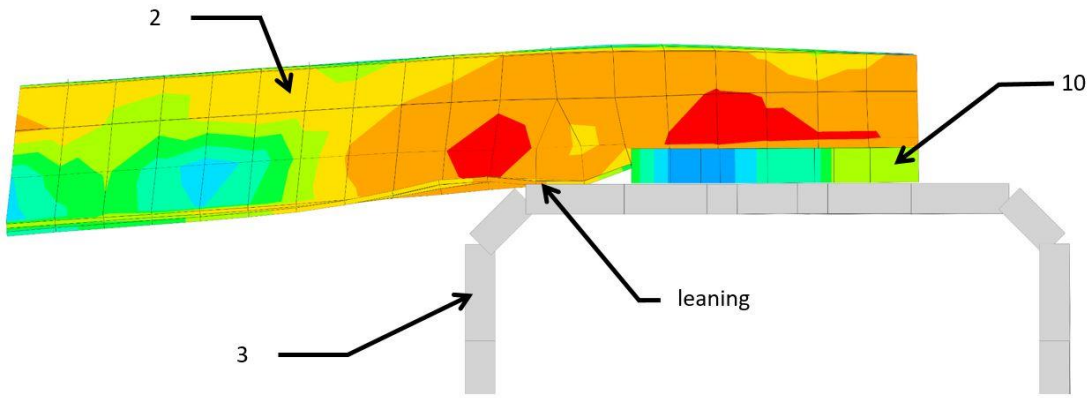

Figure 4-10 – Longitudinal cross-section of the trapeze profile leaning to the upper frame. The fringe colours and the shell thickness are shown only in terms of better readability.

4.2.3 Modification II

To preserve the benefits of placing the trapeze profile directly onto the frame but to avoid the issue with leaning, a second modification of the design has been prepared. One of the possibilities how to prevent the leaning is to change the mutual position of the trapeze profile and the frame in the longitudinal direction of the device.

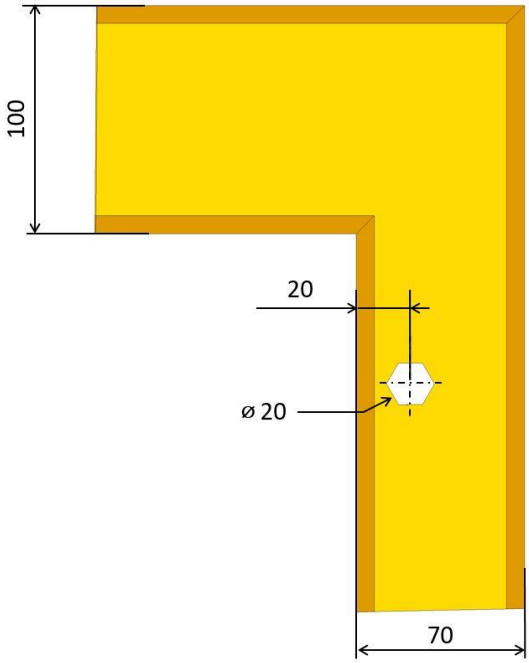

Figure 4-11 – Upper frame sketch. Dimension are in millimetres.

The idea is based on moving the holes intended for the threaded rods closer to the inner edge of the upper frame. This modification should correct the elevation created by the square washers to be sufficient and to prevent the contact between the trapeze profile and frame.

For simplification, the positions of the holes were not altered as that would need extensive adjustment of the other parts. Instead, the elements of the inner face of the frame were shifted towards the holes' position. This procedure modified the width of the frame from its original $100\,mm$ to $70\,mm$ as illustrated in Figure 4-11. The difference shall imitate the movement of the holes' position by $30\,mm$ towards the inner edge.

The result from the simulation as illustrated in Figure 4-13 proved our assumptions to be correct because the elevation from the washer in combination with the modified hole position prevented the contact. In the final concept, the edge of the washer shall be aligned with the inner face of the frame with the offset equal to the value of the outer edge radius of the frame. That also assures that the washer will not overlap.

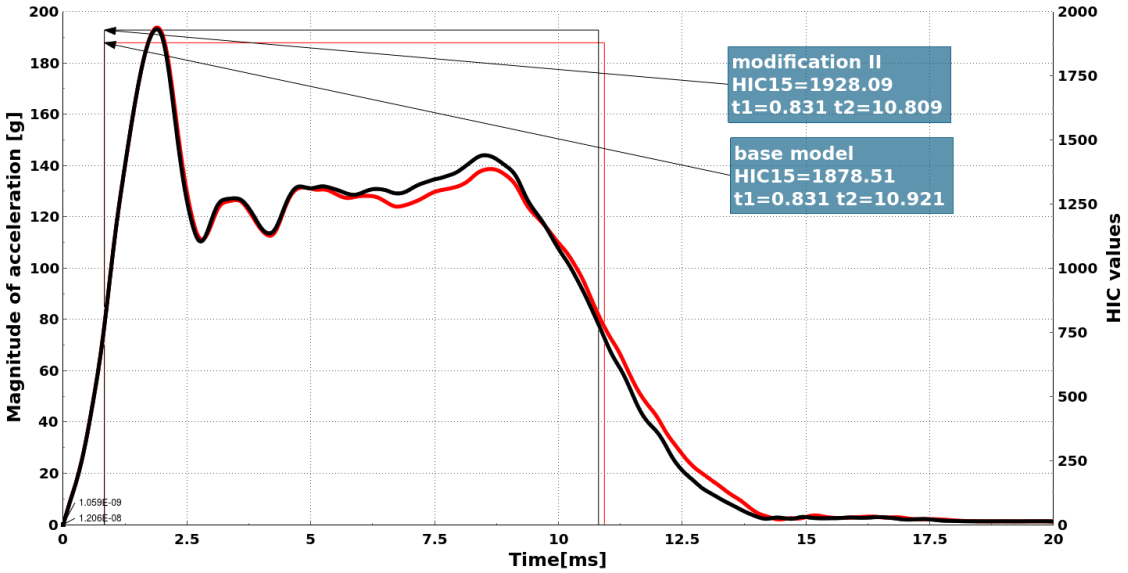

Figure 4-12 – Comparison between the magnitude of acceleration cures of the base model (red) and the modification II (black). The HIC value is increased by 2.66 %.

The resultant acceleration curve together with the acceleration of the base model is shown in Figure 4-12. The course of the curves is identical in the first quarter with a minor difference in the time interval from 5 ms to 15 ms. The HIC value is slightly greater with an overall percentage increase of 2.66 %. In conclusion, this design adjustment is suitable and beneficial.

The further modifications described below concentrate purely on the adjustment in the FE model and not the geometrical design. In addition to that, the testing plate from aluminium material was simulated and the attention was paid to the imitation of the spot welds.

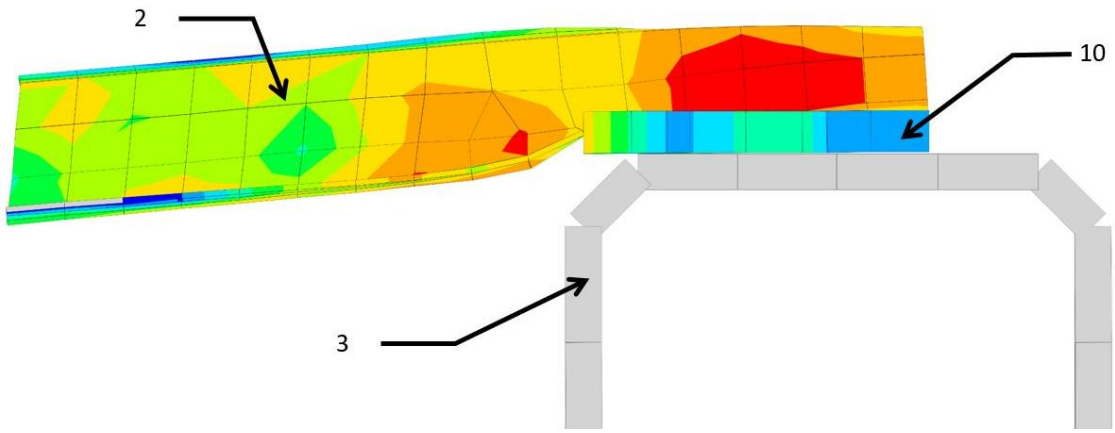

Figure 4-13 – Longitudinal cross-section of the trapeze profile and the frame. The fringe colours and the shell thickness is shown only in terms of better readability.

4.2.4 Aluminium testing plate and trapeze profile

In the original concept, the testing plates were manufactured from steel to reflect the material used in real vehicle bodywork. Since then the material engineering, together with vehicle design, has made great progress and actually the aluminium alloys are commonly used for components of the vehicle body. [4]

To evaluate the possibility of manufacturing the testing plates and trapeze profiles from the aluminium the material data of the testing plate and trapeze profiles were altered. Originally the material used for manufacturing was a steel with a yield strength of 144 MPa. Unfortunately, the designation of the material and other material properties are missing due to the age of the FE model and loss of data. The only information that was available were the material tensile loading curves, together with density, Young´s modulus and Poisson's ratio. The steel was substituted by the aluminium sheet conforming to *EN AW-5042 (EN AW-Al Mg3,5Mn),* commonly supplied in coils for sheet production. The yield strength of this material is 160 MPa and the tensile strength is 286 MPa. Although, the yield strength of the steel is lower than the aluminium, the main difference between these two materials is the strain rate in dynamic loading. The comparison between the two materials is shown in Figure 4-14.

It is evident that the course of the acceleration curves is different and the peaking maximum shifted in time to approximately 8 ms. The root of this phenomena is most probably the effect of strain rate. As the impactor rapidly actuates on the testing plate the material is resisting to the plastic deformation, thus reducing the possible displacement of the impactor and increasing the acceleration. In overall, the used aluminium alloy has lower stiffness than the original steel so the HIC value has decreased by 6.36 % compare to base model.

The behaviour of the aluminium material in simulation is different and together with other difficulties such as the price, welding and forming of the aluminium profiles, it was decided not to use the aluminium as material for production. This type of modification might be used further on as a basis for further research concerning the usage of different materials.

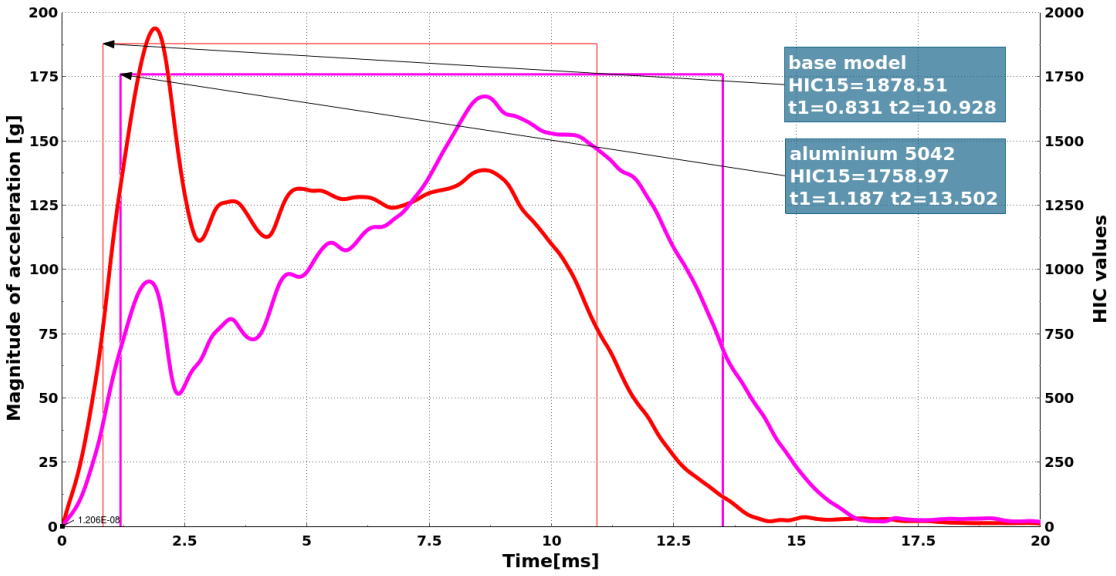

Figure 4-14 – Comparison between the magnitudes of acceleration cures of the base model with steel material (red) and the aluminium material (pink). The HIC value is decreased by 6.36%.

4.2.5 Simulation of the spot welds

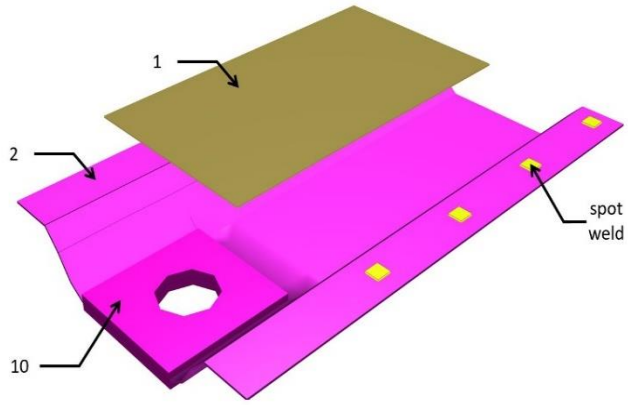

Figure 4-15 – Representation of spot welds.

Spot welding is undoubtedly the most common technique in the automotive industry how to join individual vehicle structures to create monocoque car-bodies. This welding technology is based on pressing two parts together by the electrodes and applying the electrical current. The applied pressure together with the heat generated from the electrical resistance result in localised fusion of metals, the spot weld. [41]

At the time when was the FE model of old box testing device was simulated, the connection between the testing plate and trapeze profiles was realized by imitated short beams, which were rigidly connecting the two parts. The beam had the same dimensions and material properties as real spot weld nugget. This approach of modelling is now replaced by a modern and more accurate method imitating the spot welds by FE connection representation called Hexa contact (illustrated by the green elements in Figure 4-15). The philosophy of representing the joint is in setting the contact between the created FE spot weld elements and original connected parts. Finally, the PID and material properties of the spot welds nugget shall be set.

The created spot welds nuggets are imitated such as to correspond with the original design. The diameter of the nugget is 6.2 *mm*, the pitch between the spot welds is 40 *mm*, so the total number of welding points is 144, 36 nuggets for each profile, 18 for one row. The result of the simulation is shown in Figure 4-16. The difference in the HIC and acceleration course is minimal. This method is considered more advance and, according to the internal research more accurate, therefore it will be used in further simulations.

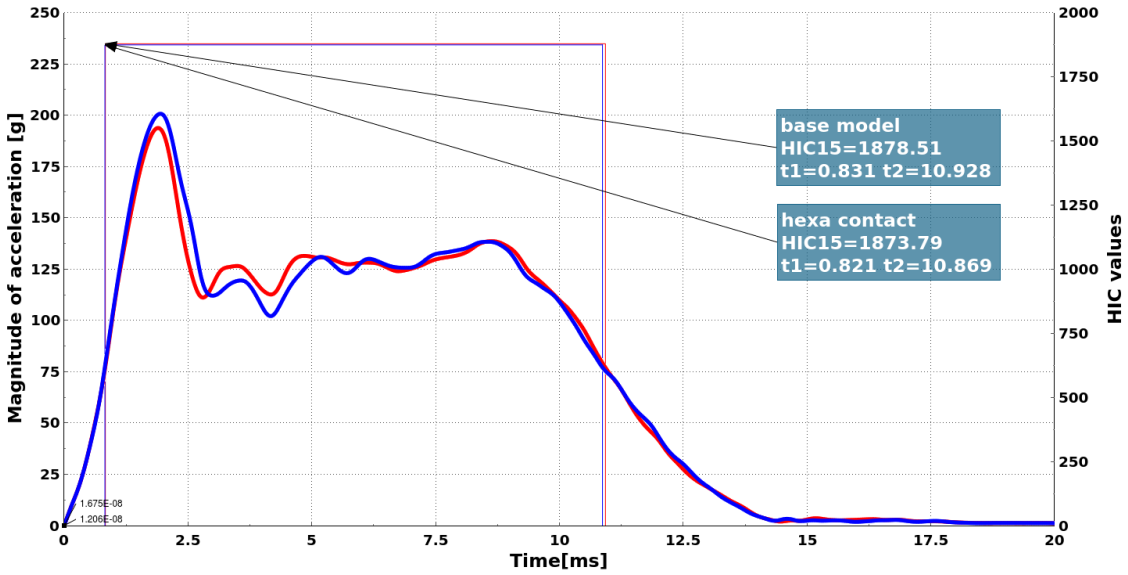

Figure 4-16 – Comparison between the magnitude of acceleration cures of the base model connected via rigid beams (red) and connected via the Hexa contact (blue). The HIC value decreased by 0.26%.

4.2.6 Adhesive bonding of the testing plate and trapeze profile

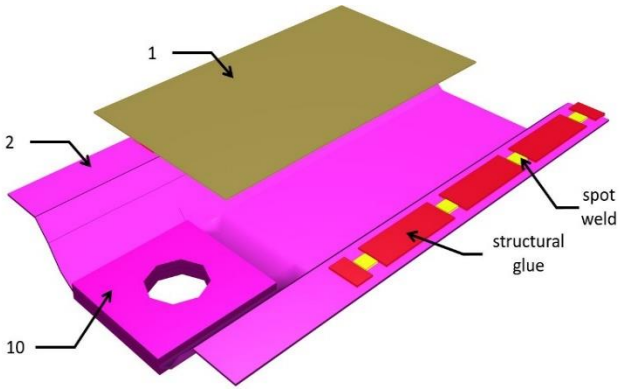

Figure 4-17 – Combination of structural glue and spot welds.

Adhesive bonding is becoming popular in the automotive industry as a replacement or complementation of conventional mechanical fastening methods such as spot welding or riveting. Using modern technique and products, adhesive glues might join metals, especially steel and aluminium or almost any plastics. Today the assembly of the vehicle body may contain tens of meters of adhesive lines. Their advantages are extensive elongation and gap-filling properties. The adhesive bonds in body construction used as a sealants in combination with spot welding or riveting make the joint more durable. [41]

For joining the testing plate to the trapeze profile a structural glue together with the conventional spot welds has been simulated. The number of adhesive stripes is eight, two for each trapeze profile, and the dimensions are 700 mm in length, 12 mm in width and the thickness of the adhesive layer is 1 mm. The pitch between the weld nuggets is the same as in the previous case – 40 mm.

The used adhesive is a structural glue with the following material properties:

Table 8 – Material properties of the adhesive glue:

-Density $[kg \cdot m^{-3}]$	Young's modulus $[GPa]$	Poisson's ratio $[-]$	Yield strength $[MPa]$
1 500	3	0.3	50

The comparison between the base model and model with a more advance approach using the adhesive bonds together with the spot welds is illustrated in Figure 4-18.

From the result it is evident, that the acceleration curve is almost identical and the HIC difference is insignificant. Taking into consideration the technological disadvantages concerning the adhesives such as the curing or higher expenses connected with manufacturing and almost none reasonable benefits for this type of application it was decided not to use this type of joint.

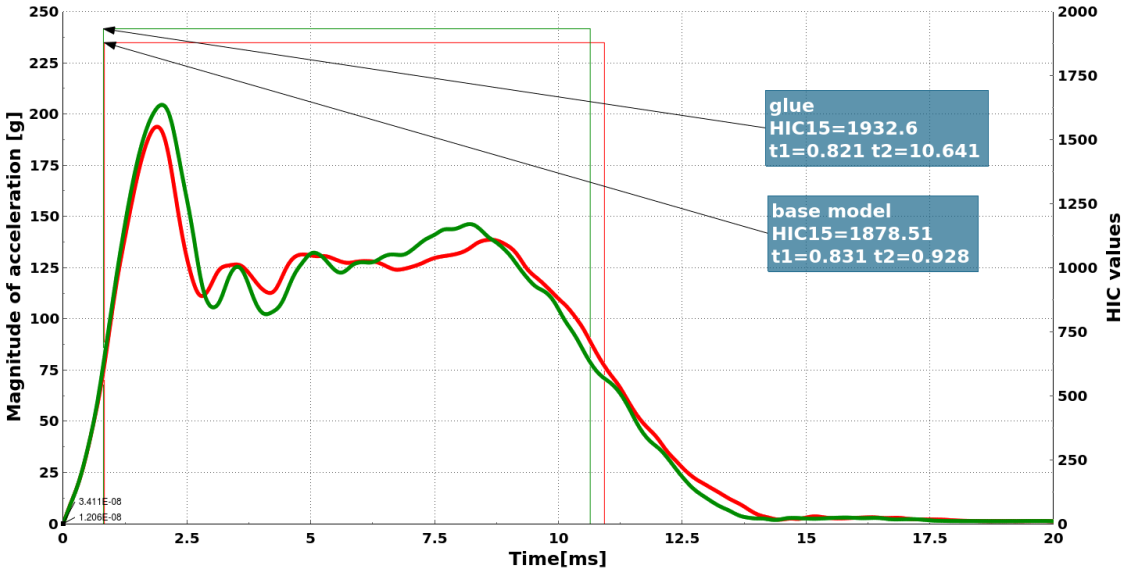

Figure 4-18 – Comparison between the magnitude of acceleration cures of the base model connected via beam spot welds (red) and connected via structural glue (dark green).
The HIC value increased by 2.88%.

4.3 Conclusion regarding the design of the old box testing device

The design and simulation modifications of the old testing device were presented on previous pages. After consultation with the *Porsche AG Research and Development department*, the results from the simulations were used as a base for the construction of the new testing device.

The conclusion and suggested design adjustments are listed below:

- The device will be using eight points system of anchoring of the testing plate assembly.
- The lateral and longitudinal support bars are redundant in term of transmission of loads and do not strengthen the box device robustness. Therefore these structures will not be used.
- To prevent the wrinkling of the testing plate while assembled to the frame, all fixture positions should be at the same level. To secure this requirement, the square washers will be welded and then milled off on the same level after manufacturing of the frame.
- The trapeze profiles will be positioned directly onto the upper frame.
- The position of the holes in the upper frame will be adjusted to prevent leaning of the trapeze profiles on the frame edge radius.
- The material of the testing plate and trapeze profile is not yet specified. It will be defined during the future processing.
- The connection between the trapeze profiles and testing plate shall be realized by spot welds only. The use of adhesive bonding does not offer any advantages.
- The number of the middle profiles will be reduced from five to three.

The suggested adjustments in the FE model are following:

- The pre-stress of 32.4 MPa substituting the tied nodes to shell surface contact shall be used in further simulations.
- Modern approach using the Hexa Contact shall be used in modelling of the spot weld nuggets.
- The size of the finite elements will be adjusted from the original length of 20 mm to today´s commonly used 6 mm.

Most of the modifications with a designation of the versions is presented in Annex II. Modifications with insignificant impact were excluded.

4.4 A new design of the box testing device

After the approval of the modifications and adjustments, the new CAD model of the box testing device was prepared by a colleague from *Porsche AG R&D* department. The output in the form of snapshot from CAD software is shown in Figure 4-19.

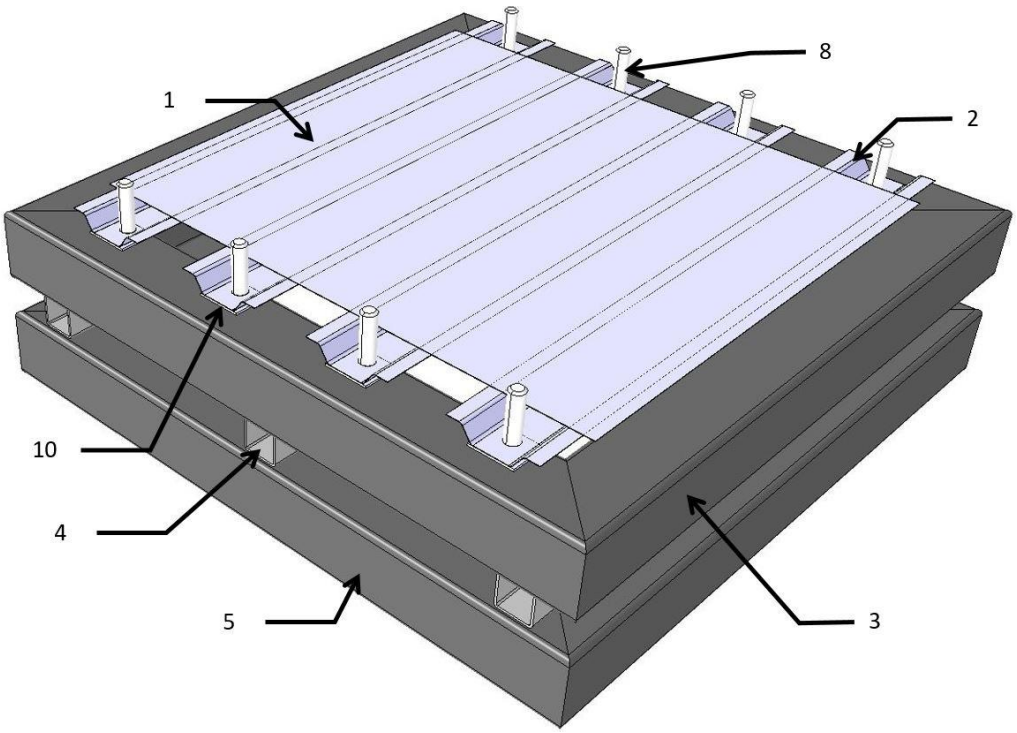

Figure 4-19 – Snapshot from Catia V5 illustrating the new design of the box testing device.

***1** – Testing plate; **2** – Trapeze profiles; **3** – Upper frame; **4** – Middle profiles; **5** – Lower frame; **8** – Threaded rods; **10** – Square washers. Nuts are hidden*

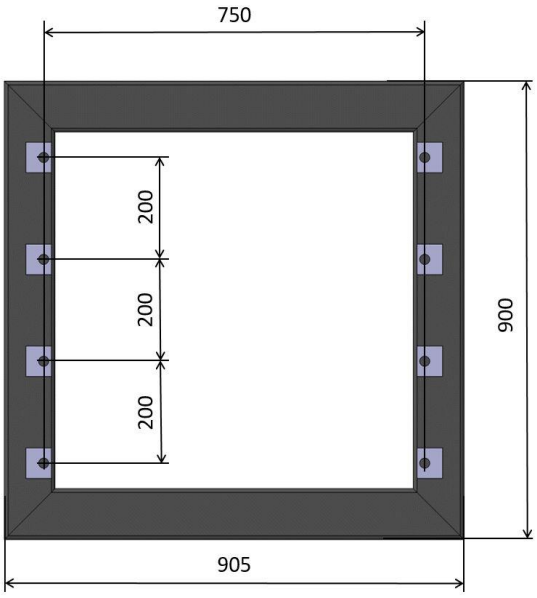

Figure 4-20 – Upper frame dimensions.

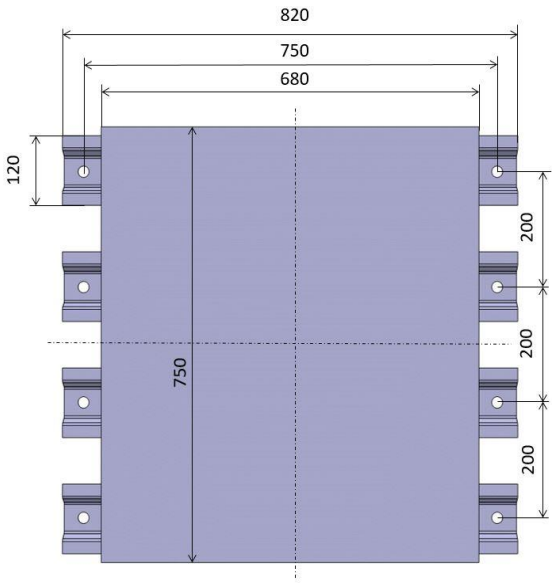

Figure 4-21 – The dimensions of the testing plate assembly.

From the first sigh it is clear that the new design is simpler while maintaining the required functionality. The main difference is the simplicity of structure assembly. The upper section of the threaded rods was reduced in length and now only one pair of nuts is tightening the assembly onto the upper frame. The square nuts are placed underneath the trapeze profiles to ensure levelling and to prevent the wrinkling as described earlier. Finally, the number of the middle profiles was also reduced.

The main dimensions of the frame are shown in Figure 4-20. The frame is welded from square hollow profiles $100 \times 100 \times 4mm$. The middle profiles have dimensions of $100 \times 100 \times 3\ mm$ and are $80\ mm$ long. The square washers are welded to the frame and have $50\ mm$ in width and they are $5\ mm$ thick for future possibility of milling of. The holes in the washers are shifted by $10\ mm$ from the center to the inner edge and are aligned with the frame inner edge radius.

The dimensions of the testing plate and trapeze profiles are illustrated in Figure 4-21.

The testing plate is $0.8\ mm$ thick sheet of metal with the dimensions of $750\ mm$ width, $680\ mm$ length. The dimensions and shape of the trapeze profile will be defined after optimization described in chapter 4.4.3. The default shape of the trapeze profile is the same as in a case of the old box design.

The materials will be discussed later on in chapter 4.4.2. For the first version of the FE model, the material data were taken over from the old model.

4.4.1 Setting up the FE model of the new box testing device

The geometry from CAD data was used as the base for successive FE model. First of all, the thin-walled structures such as frames, testing plates and trapeze profiles were converted into the middle surfaces for subsequent shell meshing process. This step included the adjustment of the geometrical elements such as edge radius and filling the gaps generated by the conversion. With respecting the symmetry of the construction was possible to use tools for work simplification such as multiple instances or *link* and *transform* functions. The main benefit of this functionality is the automatic synchronization of changes between the linked parts. This smart approach allowed us that

only one-quarter of the frames and only one-half of the trapeze profile were geometrically adjusted. The threaded rods and nuts were modelled in similar way but with consideration of the differences in subsequent solid meshing process.

The second step was the generation and adjustment of the finite element grid. With created and linked instances, the task was only to mesh one quarter of the frame and half of the trapeze profile. To achieve the best mesh quality criteria, the build-in function titled *Batch Mesh* with the company loaded scenario was used. Even with this approach, some part of the grid still needed manually adjustments. After that, the mesh was synchronized to the rest of the structure.

The next step was the assignment of the material models and data. On all structures which are assumed to experience the plastic deformation a material model called **MAT_PIECEWISE_LINEAR_PLASTICITY* considering the strain rate effect is used. For the first versions, the material data from the old FE model were used.

The modelling and meshing of the solids required special treatment. The philosophy of the modelling of the contact with solid parts consist of the creation of a solid part skin made of shell elements. The nodes of the original solid part and the nodes of the new shell elements of the skin and are then joined together. The shell elements are then used as a slave surface for *complete vehicle* (*Gesamtfahrzeug*) contact definition.

The next step is a definition of the connections. It is not necessary to imitate the welds connecting the segments of the upper and lower frame because the frames are connected in the corners by topology. The connection representing the corner joint between the middle profiles and frames is achieved via rigid beams as like as in the old model.

Further on it is important to define the contacts between the individual parts. The hexa contact defined as **TIED_SHELL_EDGE_TO_SURFACE* is imitating the spot weld nuggets and is automatically generated while modelling the spot welds connection. Further is set the *complete vehicle* (*Gesamtfahrzeug)* contact. The definition of this contact is **AUTOMATIC_SINGLE_SURFACE*, which is one of the most commonly used contact for crashworthiness applications. [36]

The next step was definition of the pre-stress and gravity load. The pre-stress in the threaded rods is set the same way as for the old model (described in chapter 4.2.1) with a difference that only one cross-section in the location between the nuts has to be created. The pre-stress value and the loading curve are the same as on the old model, thus $32.4\ MPa$ with $1\ ms$ ramp duration. The effect of the gravity is taken into account, hence all elements of the model are loaded by the acceleration of $9.806\ m \cdot s^2$ in the vertical direction.

The boundary conditions of the box testing device are defined by LS-DYNA build-in function called *SPC*. This function assigns a nodal single point constraint boundary condition to the selected nodes. A study on the old box model has been performed to estimate the influence of the boundary conditions on the resultant magnitude of acceleration. From the comparison between the base model constrained by only eight nodes (two nodes for each side of the lower frame) and the modification constrained by each of the bottom surface nodes it is evident that the course of acceleration is identical. Therefore, for the application it is sufficient to constrain only eight nodes of the lower frame bottom surface

The next step for setting the FE model of the box is a setup of database and control cards. Setup of the cards defines, e.g. which results shall be recorded for post-processing, the length of the time step increments in which the next results are computed and termination cards. The database and control cards were not manually edited but were taken from company internal sources.

Finished FE model has to involve the headform impactor for the simulation. This task was fulfilled by including the 4.5 kg adult headform impactor model via include key file provided by the supplier of the headform impactors, *LASSO mbH*. The next key files inserted together with the impactor model were the definition of the contact of the impactor to the target surface and the impact velocity, in our case 40 $km \cdot h^{-1}$. The final step was positioning of the impactor to the desired impact point by using the LS-DYNA *Pedestrian safety* function. The inputs for this function are the definition of the impactor, set of the external parts which shall be tested, the clearance between the impactor surface and impact point and finally the angle of the impact, in our case 65°. After this process, the headform impactor is automatically transformed into the desired position.

At this moment is the FE model of the box testing device with inputted headform impactor is ready for simulation. The figures below are showing the results of the simulation. Figure 4-22 is showing the distribution of stresses in the testing plate assembly while Figure 4-23 is illustrating the magnitude of acceleration course using the CFC 1000 filter. This presented version is considered as a base model of the new box for further modification.

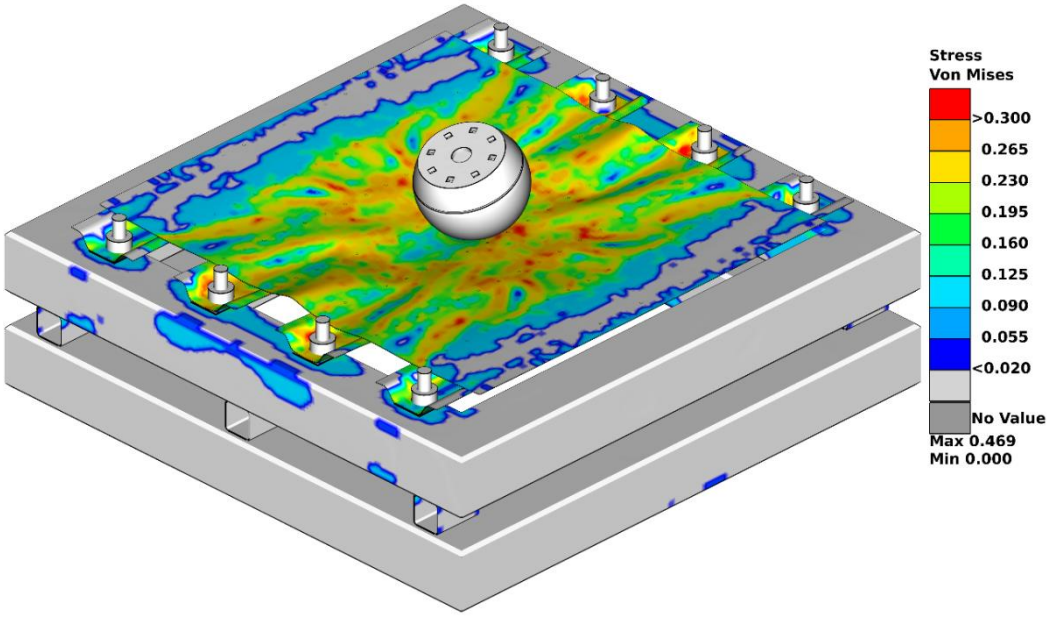

Figure 4-22 – Snapshot of simulation post-processing.

The fringe colors is showing Stress Von Mises in units of GPa.

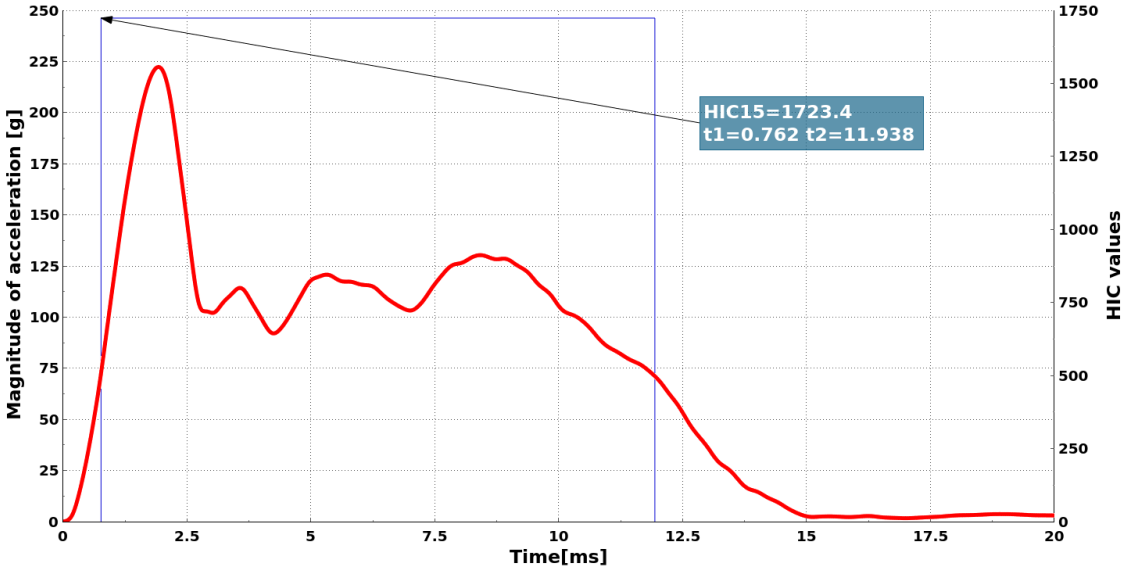

Figure 4-23 – Magnitude of acceleration vs. time history of adult headform impact derived from the new design of box testing device. On secondary axis is shown the HIC value which precise value is shown in the blue text box.

4.4.2 Definition of the testing assembly material

The modification of the material of the old FE model was discussed in chapter 4.2.4 above. In this case, an *EN AW-5042* aluminium alloy was used as a substitute for original steel testing plate and trapeze profile. In this chapter it should be decided if the material for manufacturing of the testing plate and trapeze profile will be steel or aluminium alloy and further on will be specified the definition of the individual material.

All material data for the new FE model were taken over from the old model. Unfortunately, the description of the base steel is lost therefore we need to determine a suitable substitute from the parts will be manufactured. Three material modifications were calculated to investigate the simulation's behaviour regarding the used material. Two of them were concerning the steel and the third modification used the aluminium alloy. We have chosen two steels substitutes, the *HX260LAD+Z* and *HX180YD+Z* from the company internal sources.

The designation *HX* stands for flat products (in our application steel sheets) supplied in rolls. The three-digit number is stating the minimal proof strength[10] $R_{p0.2}$ followed by the designation of the alloying level. The *LA* stands for low/micro-alloy steel whereas the letter *Y* is representing the interstitial free steels. The last two letters are designating the intention for hot-dip galvanizing [42]. Both of these steels excel in weldability and elongation and another of their characteristic is significant strain rate effect. Thanks to their properties, they are suitable for cold forming, therefore they are commonly used in vehicle bodyworks.

The third computed simulation was focused on aluminium alloy. Notwithstanding the fact that this material was rejected as non-suitable substitute in the first phase of optimisation, we have nominated this material to satisfy the complexity of the results. The original steel

[10] Proof strength is equivalent to yield strength for materials with non-linear behaviour where the yield point could not be well defined. The proof strength is defined at 0.2 % strain on stress-strain curve. [50]

testing plate together with the trapeze profiles was substituted by *EN AW-5042* (*EN AW-Al Mg3.5Mn*) aluminium alloy.

The detailed material properties of all materials used in simulations are listed in Table 9. Values were taken from material properties and stress-strain curves displayed in pre-processor. The values were further verified by checking the DIN material standards. [42], [43]

Table 9 – Material properties of used materials

Material	Density $\rho\ \left[\frac{kg}{m^{-3}}\right]$	Young´s modulus $E\ [GPa]$	Proof strength $R_{p0.2}$ $[MPa]$	Tensile strength R_m $[MPa]$	Elongation A_{80} [%]
Base steel	7850	210	144	381	-
HX260LAD	7850	210	273	616	26 – [42]
HX180YD	7850	210	204	564	34 – [42]
EN AW-5042	2650	70	160	286	≥ 18[11] – [43]

The results of the simulations are illustrated in Figure 4-24. From the courses of the curves it is clear, that the HIC values are increasing with improved properties of the material. The summary results are listed in Table 10. It can be stated that the course of steel acceleration curves is almost identical except the offset caused by different yield point and the behaviour in plastic deformation. The course of aluminium acceleration curve is different due to the reason described in chapter 4.2.4. The effort was to get the new course as close as possible to the original acceleration course. In terms of HIC values we want to get closer to the upper limit allowed by the standards. Generally, the HIC values obtained from the box testing device should be in a range achievable by the actual vehicle bonnets

Table 10 – Results of the material simulations. The differences are related to the base model

Material	HIC	HIC difference	HIC difference [%]	a_{max} [g]
Base steel	1723.44	0	0	223.13
HX260LAD	2398.12	+674.70	+39.15	244.13
HX180YD	1933.91	+210.51	+12.21	228.73
EN AW-5042	1403.32	-320.12	-18.57	137.20

From the inspection of the resultant magnitudes of acceleration it is evident that the steel *HX260LAD* is too stiff because of relatively large proof strength. On the contrary, the steel *HX180YD* appears to have similar course as the original even though the HIC values have increased by $+12.21\%$. Although the absolute HIC is greater than maximal allowed value by the standards for vehicle bonnets the usage of *HX180YD* seems justified.

[11] Original length of specimen was $L_0 = 50\ mm$

For the reasons described above it was decided to manufacture the testing plate and trapeze profile from steel *HX180YD*. The problem with slightly larger HIC values will be solved in the next chapter.

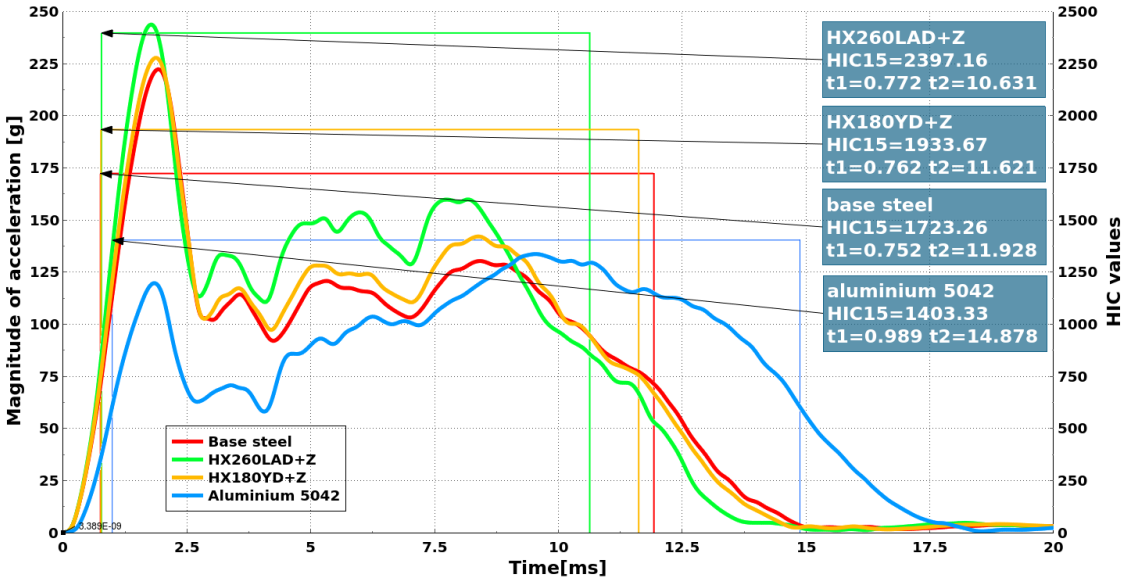

Figure 4-24 – Comparison of different steel materials and aluminium alloy.

The red curve is representing the base steel, the green curve is steel HX260LAD, yellow curve is steel HX180YD and blue curve is EN AW-5042 aluminium alloy.

4.4.3 Modification of the trapeze profile

If we would like to lower the HIC performance to get closer to the standard range we have three options available:

The first option is to choose a more yielding material such as aluminium or steel with weaker mechanical properties. Because the effort has been made to choose a suitable material in the previous chapter this option seems inappropriate.

The second option is to reduce the impact velocity originally set to the value of 40 $km \cdot h^{-1}$. The impact velocity is directly proportional to the resultant acceleration values thus decreasing the initial velocity has a direct consequence on decreasing the HIC values. Because the alternation of the headform impactor´s initial velocity shall be the subject of other future studies, this option was also rejected.

The last option to reduce the HIC values is the modification of the trapeze profile height because dimensions of any profile are proportional to its geometrical cross-section characteristics. In our case, the major type of stress is caused by the bending moment around the lateral axis arisen from headform impact. The geometrical characteristic describing the bending stress is the principal moment of inertia[12] for bending in the principal axis. The moment of inertia is proportional to the height of the trapeze profile, so with the decreasing height, the moment of inertia is also decreasing. According to the well know formula (4.9) [44] for bending stress where M_o is the bending moment, J is the principal moment of inertia for bending and ρ is representing the distance from the principal axis to the location where we would like to investigate the stress, it is obvious

[12] Also known as 2nd moment of area [mm^4]

that with the decreasing principal moment the resultant bending stress is increasing. As a result of increased stress, the yield point is exceeded and the plastic deformation, absorbing the energy, take place. As the kinetic energy of the impactor is absorbed by the deformation, the resultant acceleration and consequently the HIC value is lower than in case of higher trapeze profile.

$$\sigma = \frac{M_o}{J} \cdot \rho \tag{4.9}$$

The original trapeze profile was $20\ mm$ high and its height was reduced by one quarter to $15\ mm$ to lower the acceleration. A new design of the trapeze profile is shown in Figure 4-25. The only difference between the new and the old design is the trapeze height. All other dimension remains the same.

To evaluate the influence of the height reduction the principal moments of inertia of the cross-section characteristics were measured using the Ansa build-in *Cross* module. The original design of the trapeze profile has the principal moment of inertia for bending $J_{20} = 2\ 197\ mm^4$ and the modified design has the principal moment of inertia $J_{15} = 1\ 885\ mm^4$. The complete cross-section characteristics for both profiles are listed in Annex IV and Annex V.

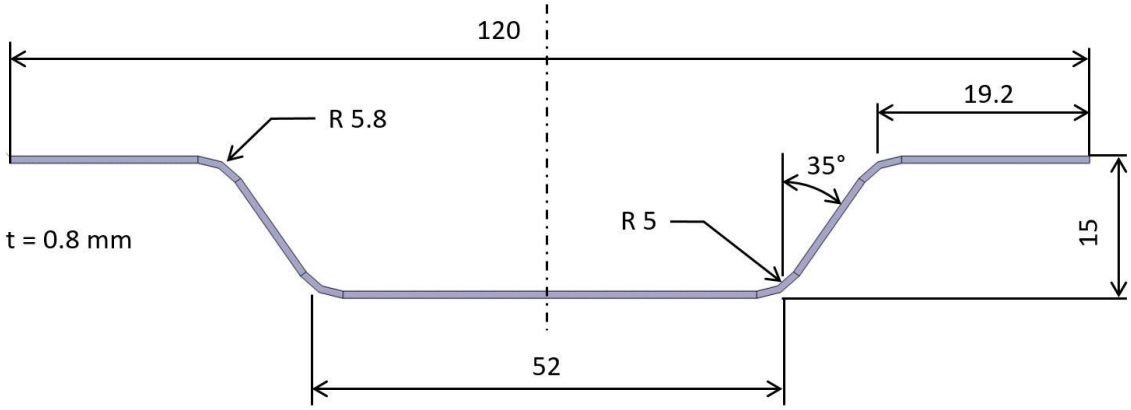

Figure 4-25 – The dimension of the new trapeze profile.

Figure 4-26 illustrates the resultant magnitudes of acceleration of both trapeze profile design variants. According to the assumption, the HIC value has decreased by 14.51 % to the value of $HIC_{15} = 1\ 653$. Because the resultant HIC value is significantly lower than the original and lies in a range achievable by the real bonnet, it was decided to use this modification in the final design of the box testing device.

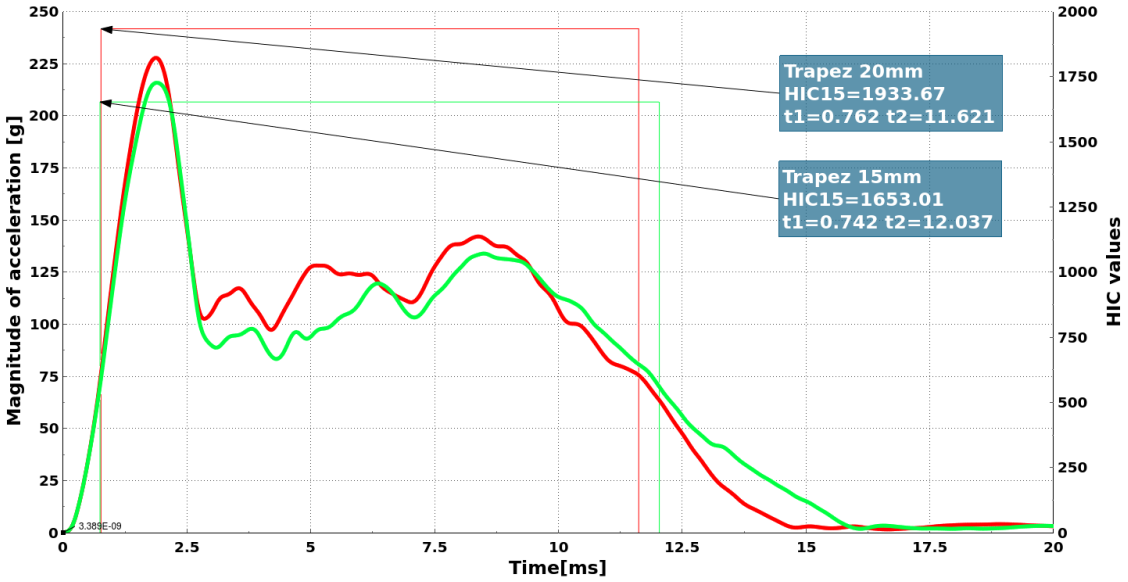

Figure 4-26 – Comparison between magnitudes of acceleration cures of the original trapeze profile 20mm high (red) and adjusted trapeze profile with 15 mm in height (light green). The HIC value is decreased by -14.51%.

4.4.4 Modification of impact velocity

For the reason stipulated in previous chapter, the alternation of impact velocity was not the subject of study. The originally set impact velocity of 40 $km \cdot h^{-1}$ is taken over from *Euro NCAP´s Pedestrian test protocol* [45]. Lower impact velocity of 35 $km \cdot h^{-1}$ is required for pedestrian protection tests according to European Commission´s regulations [13] and [14]. The velocity requirement of the Euro NCAP is more strict because this consortium is testing the vehicle safety using test procedures simulating the accidents in more stricter manner.

The comparison between the two simulations which differs only in the initial velocity is presented in this chapter only to illustrate the influence of the impact velocity. The results are shown in Figure 4-27.

From the chart it is evident, that the maximal peak of acceleration is significantly smaller by nearly 30 g. The rest of the process is almost identical except minor vertical offset. An interesting fact is, that the decrease of the initial velocity by only 12.5% caused the reduction of HIC by almost 22%. The outputs from this simulation are prooving the assumptions described in chapter 2.3.2 concerning the survival rate dependency of pedestrian collision.

Although the impact angle was not particularly investigated in our simulations, we may expect the similar behaviour i.e. that with the decreasing impact angle the resultant HIC values will be also decreasing.

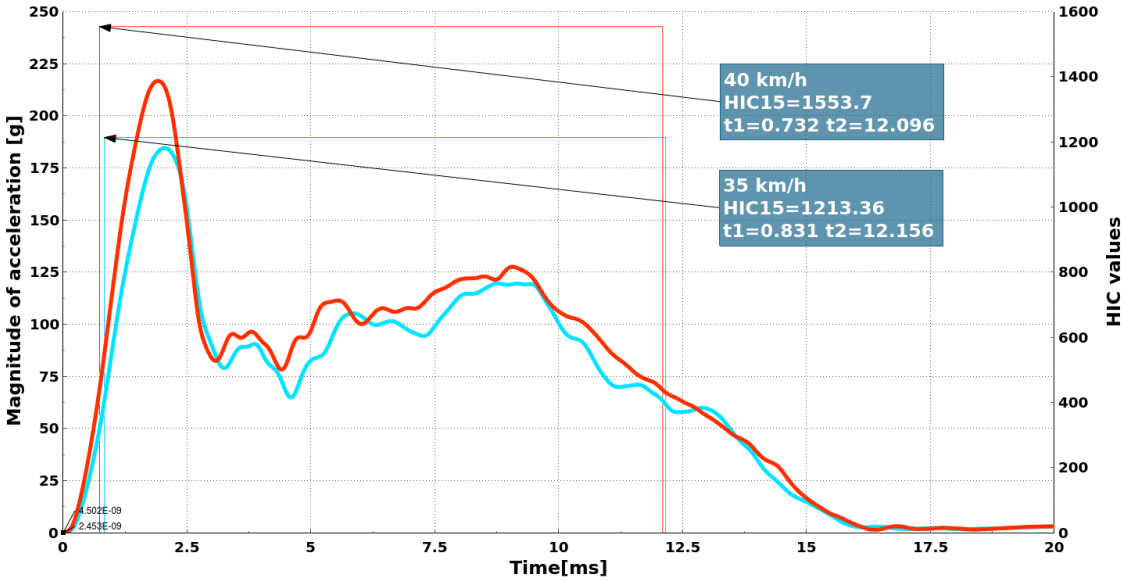

Figure 4-27 – Comparison between acceleration cures of the 40 $km \cdot h^{-1}$ impact velocity (red) and 35 $km \cdot h^{-1}$ impact velocity (light blue). The HIC value is decreased by -21.91%.

4.5 Conclusion regarding the design of the new box testing device

After consultation with colleagues from the *Porsche AG* R*esearch and Development department*, the outputs and recommendation from the simulations were used as base for production of the new testing device.

The number of presented results from the simulations concerning the new design is significantly lesser than in the case of the first phase optimisation because most of the versions were focused on functionality of the simulation and not on the design optimisation process itself.

The conclusion and suggested design changes are listed below:

- The dimensions of the testing plate, trapeze profile and the device frame shall be as illustrated in Figure 4-20, Figure 4-21 and Figure 4-25. The frame of the device shall be manufactured from square hollow profiles 100 x 100 x 4 mm. The middle profiles shall be manufactured from 50 x 50 x 3 mm profiles and will be 80 mm long.
- The testing plates will be cut from the metal sheet and the trapeze profiles will be manufactured on the bending machine.
- The material used for the production of the testing plate and the trapeze profile shall be *HX180D*. It is important, that the testing plate and the trapeze profile ought to be manufactured from the same batch of the material to ensure the same properties. Besides, several tensile tests shall be carried out on 70 x 20 specimens to verify the granted material data entering the simulations.
- After the discussion it was decided, to decrease the spot weld pitch from original 40 mm to 20 mm. A validation simulation was run to investigate the influence of smaller pitch. The HIC difference is only -1.45%, therefore, there is no need to recalculate the whole set of simulations. The difference is negligible.

- To ensure required elevation and to prevent wrinkling of the testing assembly, the square washers welded to the frame will be used. A vertical dimension of each welded washer will be measured on a 3D measuring machine to set an individual height which should be milled of. This shall assure the vertical levelling. The original height of the washers will be $5\ mm$.
- The issue with leaning due to the movement of the holes described in chapter 4.2.2 was checked and passed.
- To assure required pre-stress of $32.4\ MPa$ in the threaded rods a minimal tightening torque of $25\ Nm$ shall be applied while assembling the testing plates to the frame as calculated in chapter 4.2.1.2.

Most of the modifications with a designation of the versions is presented in Annex III. Modifications with insignificant impact were excluded.

After the second phase of optimisation, the design of the device is complete and at this moment is ready for production.

4.6 Production of the new box testing device

The production of the new box testing device started in December 2019 on behalf of the *Porsche AG R&D* department. In the first phase the frame of the device was weld together from hollow square profiles. Painted product with milled square washers is shown in Figure 4-28.

Subsequently the testing plate was spot-welded together with the bent trapeze profiles. In the first stage only twenty specimens was produced (see Figure 4-29) for pivot in-house experiments in the own *Porsche AG's* pedestrian protection laboratory.

In the future it is planned to conduct more experiments in different laboratories – for details see chapter 5. It is required to follow the same technological approaches to ensure the comparability of individual batches of testing specimens.

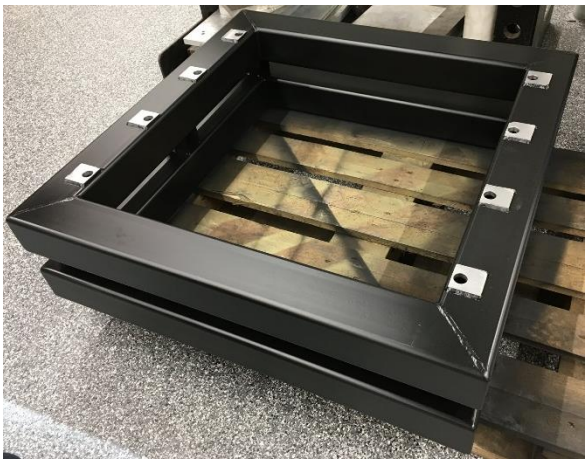

Figure 4-28 – Frame.

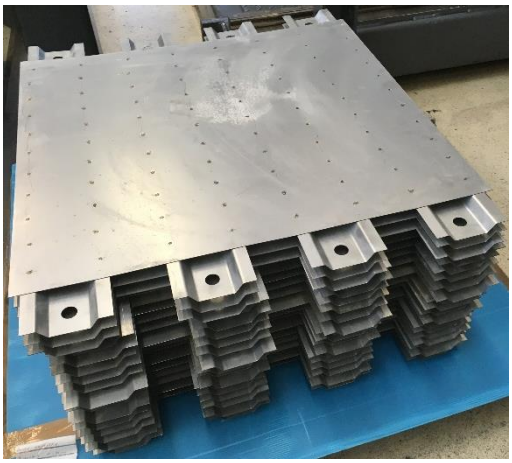

Figure 4-29 – Testing specimens.

5 Box testing device experiments

The main objective of this master's Thesis is to investigate why the same headform impactors are behaving differently when being used for testing in different laboratories. In other words, why are the results of the same experiment different when executed elsewhere? Until now, this problem has been solved only with virtual FEM simulations, which, unlike the real experiments, will always bring the same results if the same initial and simulation conditions are preserved.

The FEM simulations play a key role in contemporary automotive development and, among other things, in crashworthiness application. Over the past years, this approach has become more detailed and precise than ever. Nevertheless, the comparison between the simulations and the real experiments is still a vital part of the FEM model's validification process. To achieve the validification of the model, a series of experimental tests in different laboratories concerning just manufactured box testing device are supposed to be carried out. The box testing device is only an instrument for headform impactors tests because, as described in chapter 4, the usage of real vehicle bonnets would be too expensive and difficult for preparation. Now It is possible to continue with experiments and research to investigate the behaviour of the impactor after the validation process.

The experiments are supposed to be carried out in four different laboratories capable of executing the pedestrian protection tests with both types of headform impactors. The number of laboratories is sufficient to exclude any systematic error from occurring in a specific laboratory. Such error might arise from the way the impactor is propelled, further from data acquisition, evaluation etc. Before the experiments, it will be necessary to define precisely the initial conditions, such as the impact velocity and the impact angle for future comparison.

The first laboratory where the experiments are about to be executed is *the Porsche AG's Pedestrian Protection laboratory* in *Weissach Development Centre.* In the first series of experiments, the batch of twenty already manufactured testing plates shall be proofed by circumstances set in advance. The second set of experiments shall be carried out in an independent laboratory near the *Porsche's Research and Development Centre*. The third laboratory is supposed to be *Audi AG's Pedestrian Protection Laboratory* in Ingolstadt. The last, forth, laboratory where the experiment might be carried out is located in Prague and is under the ownership of the *Faculty of the Mechanical Engineering* of the *Czech Technical University.* This particular laboratory is equipped with a pedestrian protection throwing device, which is described in detail in chapter 6.

If we wish to continue with the experiments, there is a possibility to use another pedestrian protection laboratory located in the Czech Republic. Specifically, it is a laboratory under the Czech department of the *TÜV SÜD,* located near Mladá Boleslav. The last possibility is to cooperate with a pedestrian protection laboratory located in the North Bohemian town of Chrastava.

The first set of experiments in Weissach laboratory was about to begin in the 14th working week of the year 2020. Unfortunately, due to the 2019 – 2020 Coronavirus outbreak and subsequent COVID-19 worldwide pandemic situation, the experiments were postponed indefinitely. At the time of writing this master's thesis (April 2020), it is still uncertain when the experiments will continue. Either way, the post-processing and evaluation of these experiments will be the subject of future research.

6 Pedestrian protection throwing device

These devices are used to perform impactors' tests to assess pedestrian safety of the vehicles. Their task is to accelerate the impactors to the required impact velocity and to define the direction of the flight towards the vehicle front end. The devices could work in different ways and the most commonly used principles to grant the impactor's initial velocity are hydraulic, pneumatic or mechanical. After throwing, it is necessary to continuously acquire the measured data from a sensors located in the impactors. The transfer of the data is often solved via sets of conductors connected in full bridge output. The more expensive sensors and impactors might use wireless connectivity for data acquisition. The impactors are further attached to the frame of the device by a steel security wire, which ensures the restriction of impactor's movement after the rebound of the tested part.

6.1 Juliska throwing device

Another device for performing pedestrian protection tests is located in the Juliska laboratory of the *Faculty of Mechanical Engineering, Department of Automotive, Combustion Engine and Railway Engineering*. This device was assembled according to the design of Ing. Jiří Zejda and on the basis of his master's Thesis *Design of a device for testing the front part of a car using an impactor according to the EEVC WG 17 methodology*. [46] The master's Thesis was written in the year 2003, at a time when pedestrian protection tests were not yet mandatory and there were few testing facilities worldwide, none in the Czech Republic. The design was therefore limited only by the functional and legislative requirements of the EEVC WG17.

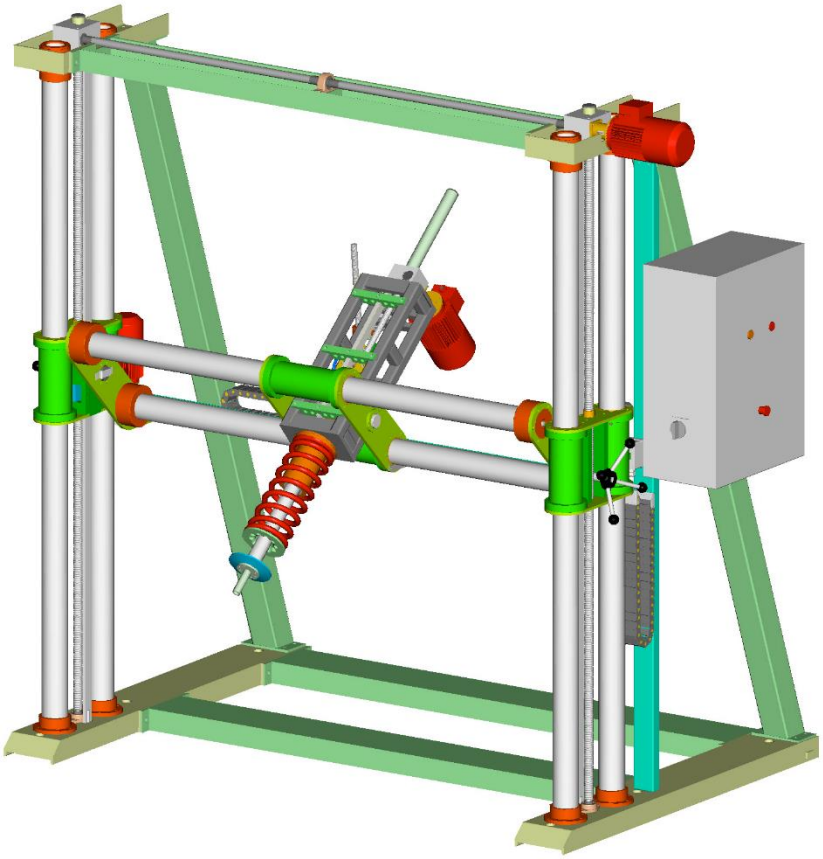

Figure 6-1 – Juliska throwing device. Figure from CAD model. [46]

The arrangement of the device is illustrated in Figure 6-1. The device consists of a large number of components that perform various functions. The description of the functions of all components would go beyond the scope of this master's Thesis, and therefore we will limit ourselves only to the introduction of the most important components. A more detailed description of the device is presented in [46] and [47].

The design of the device consists of a main portal frame which allows movement in a vertical direction and an auxiliary sub-frame used for horizontal movement. The movement in both directions is allowed by electromotors connected to the moving screws and two pairs of guidance rods. A movement in a third direction is supposed to be done by moving the tested vehicle in a longitudinal direction.

The impactors are propelled by a throwing assembly illustrated in Figure 6-2, consisting of multiple parts. The impactor is connected to the impactor's adapter (12) to prevent the impactor from falling out in case of throwing in the top-bottom direction. The adapter is connected by the inner thread to a central rod (9) and by screws to the end plate (11). The coil spring (8) is compressed between the end plate (10) and the spring front (7) to transform its internal potential energy to the kinetic energy of the impactor after throwing. Before the spring is being compressed, it is needed to insert the central rod ending (5) into the pulleys (4) until secured. The compression of the spring is then realized via a moving screw (13), which is extended from the worm gearbox driven by a three-phase asynchronous electric motor (hidden in Figure 6-2).

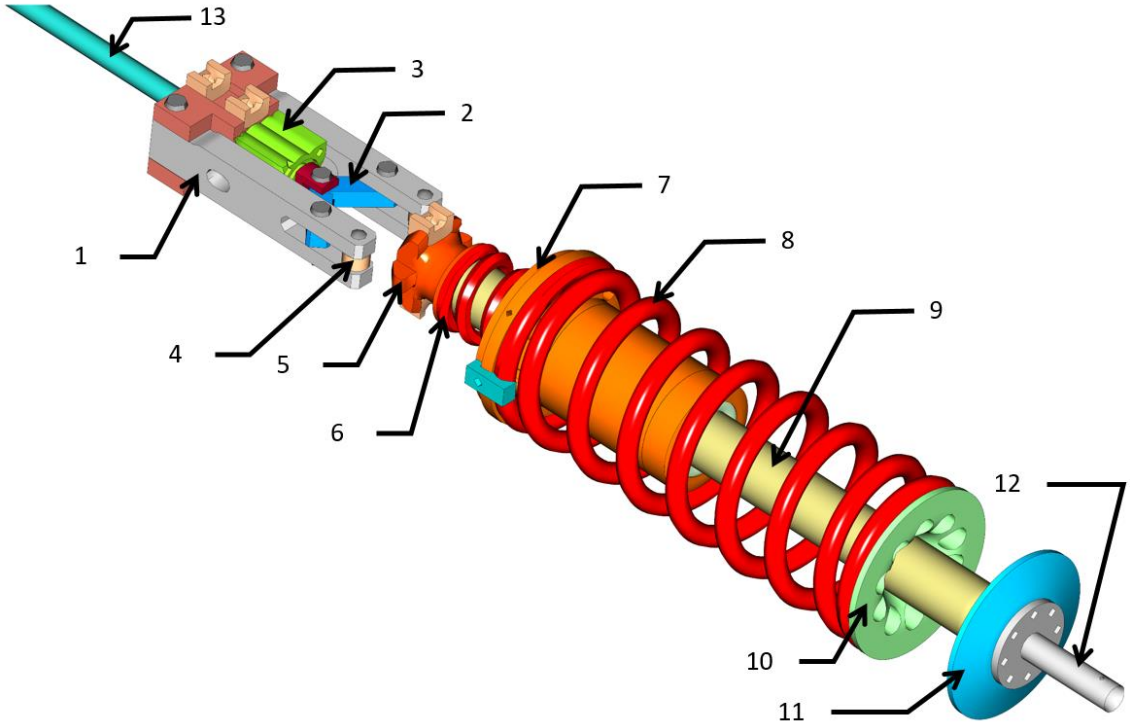

Figure 6-2 – Throwing assembly description. The frame and other entities are hidden.

***1** – Claws; **2** – Claws; **3** – Penumatic cylinder; **4** – Pulley; **5** – Central rod ending; **6** – Damping spring; **7** – Spring front; **8** – Coil spring; **9** – Central rod; **10** – End plate; **11** – End plate; **12** – Impactor's adapter*

The release is performed by an assembly consisting of a pneumatic cylinder (3) which opens the claws (1;2). with its advancing stroke. Afterwards, the pulleys (4) are rolled away from the central rod ending's face (5) to release the spring assembly. The damping spring (6) is used to remove or at least mitigate the consequence of shock weaves rising from the impact.

6.2 Renovation of the Juliska throwing device

The production of the device started at the end of the year 2003 and the device was in operation for a few years after completion. Unfortunately, after some time, the activities around this throwing device declined and the device started to decay.

In the year 2018, the pedestrian protection activities at the CTU *Faculty of Mechanical Engineering* started to increase and the main interest was to renovate and modernize the device to the contemporary standards. The idea was to check the device's functionality, make any necessary design adjustments, and further to equip the device with the present-day measuring sensors. At the time of the device's production, it was not common to acquire big amounts of data because of finical and other reasons. Because of that, some of the physical parameters such as the inclination of the throwing frame or the spring compression were not digitally collected. The reader is referred to see chapter 6.2.4, where all of the sensors used are presented. Another of the required adjustments concerned the attachment of the impactors to the adapter, as described in chapter 6.2.3.1.

The first step was to inspect the electrical installations followed by a revision of the electromotors, and a lubrication of the moving screws, guidance rods, sliding bushes, and bearings. The functionality of all of three electromotors was also checked.

So far, every component and the whole structure of the throwing device seemed functional. Unfortunately, after the first few probationary throws, it became clear that the device was not capable of compressing the spring to the desired amount. This problem will be discussed in the following chapter.

6.2.1 Issue with the central rod ending

While we were trying to compress the coil spring between the spring front and the end plate, the throwing assembly was not able to hold the emerging forces and the shot took place spontaneously and unintentionally. This phenomenon is unacceptable and hinders the correct usage of the device.

The cause of this issue was found in contact surfaces of the central rod ending, which were worn out. The spontaneous rolling away of the pulleys and the subsequent release of the mechanism was due to an imperfection on the surface. The contact surfaces were not perfectly flat because of the age and the contact forces, which were there as a result of the compressed spring. The arrangement of the mechanism is shown in Figure 6-3. The yellow circle indicates the problematic contact surface.

The first and simplest idea of how to solve this issue was to disassemble the mechanism, weld an additional material to prevent the unwanted spontaneous release and regrind the surface.

Unfortunately, these adjustments did not bring the desired effect and the issue with the release was still unsolved. Another way of solving it is presented in the following chapters.

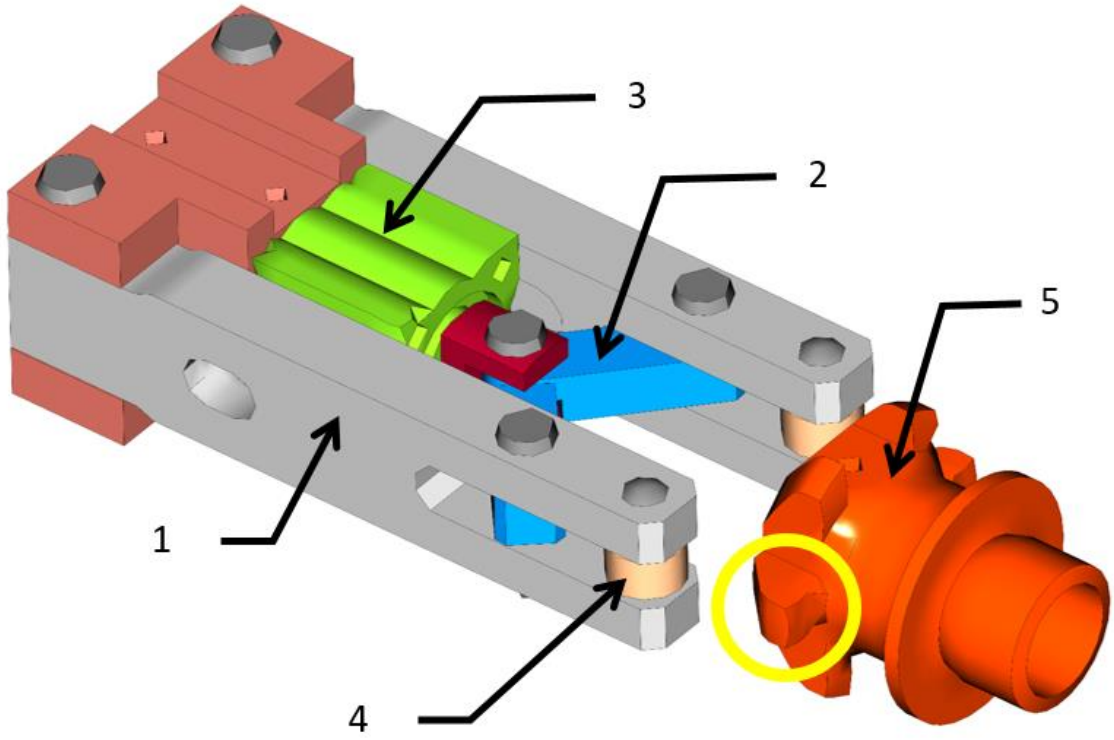

Figure 6-3 – Release mechanism of the throwing device. The yellow circle indicates the problematic contact surface. The numbered items are the same as in Figure 6-2.

6.2.1.1 Pneumatic cylinder

The second approach to prevent the unwanted release involves the pneumatic cylinder (in Figure 6-2, Figure 6-3, number 3). A single-acting, short-stroke pneumatic cylinder *Festo AEVC-40-25-I-P* [46] is used to release the throwing mechanism. The idea consists of replacing the original single-acting cylinder with a double-acting *ADVC-40-25-I-P* pneumatic cylinder from the same model series. The return stroke of the double-acting cylinder holds the claws closed so the pulleys are not able to roll away. The forces from the spring, acting where the pulleys are, were calculated and compared with the datasheet values [48]. Using this assumption, the solution is supposed to be functional. However, there were complications.

The first complication with this solution is the increased financial costs because, with the replacement of the cylinder, it is necessary to equip the device with a second, normally open, 3/2-way solenoid valve *CPE18-M3H-3OL* [49] and to modify the pneumatic circuit, as shown in Figure 6-4.

The second problem with replacing the original cylinder with a double-acting one is a difference in dimension. As stated in the Festo datasheet [48], the width and height of both cylinders are the same. Unfortunately, the length of the double-acting *ADVC* cylinder is 5 *mm* greater than the original single-acting *AEVC* cylinder. Because of this length difference, the piston of the double-acting cylinder will be permanently pushing the claws apart so the pulleys will hold the central rod end farther away from the centre.

The consequence of the length difference is unacceptable. Furthermore, the increased financial expenses are significant. Therefore we have decided to reject this method.

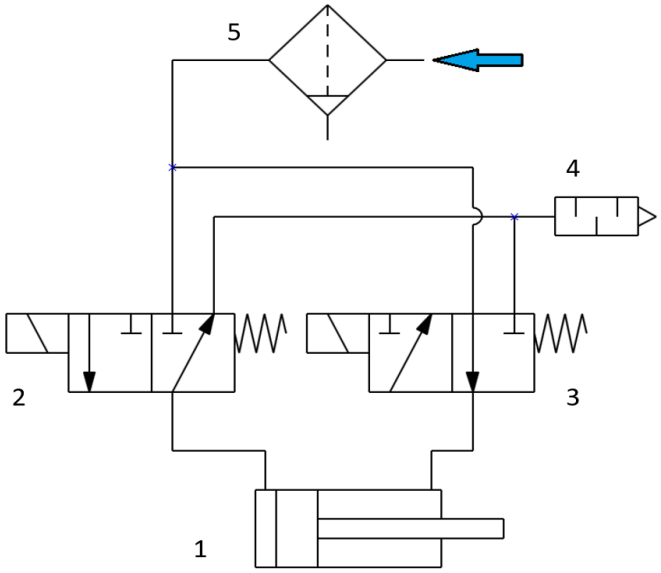

Figure 6-4 – The adjusted pneumatic circuit with the double-acting cylinder.

***1** – Pneumatic cylinder Festo ADVC-40-25 ; **2** – 3/2 solenoid valve CPE18-M3H-3GL;*
***3** – 3/2 Solenoid valve CPE18-M3H-3OL; **4** – Silencer; **5** – Water filter*

The original scheme is composed only of the single acting cylinder Festo AEVC-40-25, 3/2 solenoid valve CPE18-M3H-3GL, a silencer and a water filer.

6.2.1.2 Manufacturing and heat treatment of the new central rod end

The solution to the prevention of the spontaneous release, which was ultimately implemented, consists of manufacturing a new central rod end from material with better mechanical properties and a subsequent heat-treating process to increase hardness of the surface.

Originally, the central rod end was manufactured from *EN E335 (ČSN 11 600)* [46] steel. To increase the end plate stiffness, it was decided to manufacture the new part from *EN C45E (ČSN 12 050)* steel. Unfortunately, due to the age of the device, all of the technical accessory, such as the CAD models or drawings, were lost[13]. Therefore, the dimensions of the old ending part were first measured by a calliper. Subsequently, the new part was manufactured using lathe and milling machines.

After the production process, the newly manufactured part was shipped to an external company for heat treatment. The technology process chosen was nitriding as it is the process with the highest surface hardness after treatment [50].

After the heat treatment, the new central rod end replaced the previous one on the device and a few pilot shots were performed. Now, even when the coil spring is compressed to the maximal limit, the release mechanism fulfils its function. The issue with the spontaneous release is therefore solved and it is now possible to continue with other matters regarding the testing device's modernisation.

[13] The new central rod ending was manufactured at the end of 2019. By then, the drawing and CAD data regarding the throwing device had been lost. Eventually, the CAD data were restored in February 2020. So for the future progress, CAD data were available.

6.2.2 Attachment of the impactors to the throwing device

Another design adjustment that will be beneficial to the device's modernisation and experiment repeatability is a modification regarding the attachment of the impactors to the impactors' adapter (in Figure 6-2, titled 12). The old design was using a toothpick system to prevent the impactors from falling out while preparing the experiments. To understand the mechanism, the reader is referred to Figure 6-5, where the arrangement is illustrated.

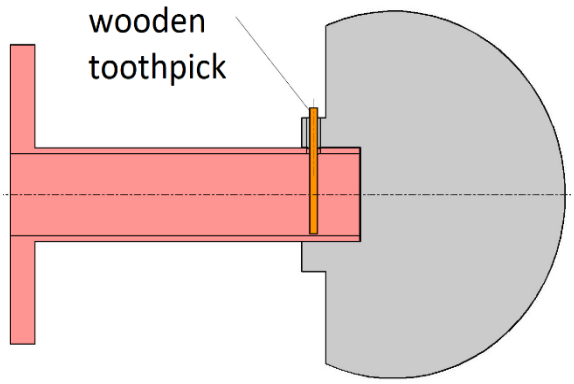

Figure 6-5 – The attachment mechanism using a wooden toothpick [46]

The system consists of a flange with holes for screws welded together with a hollow rod. The impactor is pulled over the rod and secured by a wooden toothpick on both sides to prevent falling out. After the release, the toothpick is broken by the impactor's inertial forces and, from there onwards, the impactor is in the state of free flight.

As expected, this simple solution could be a source of measurement error, because the toothpick could be broken a little differently every time, so the resultant initial velocity might also be different every time.

It was therefore decided to use an electromagnet system as a more contemporary and sophisticated approach to attach the impactor to the device. This decision required a purchase of an electromagnet and a further modification in the design of both the device and the impactors, as described in chapters 6.2.3 and 6.3.1.3.

The first step was to choose an appropriate electromagnet. For security and convenience reasons, it was decided to use a permanent magnetic holding solenoid. The advantage of this electromagnet is that there is no need to charge the circuit in order to have a lasting magnetic field. When the circuit is excited by the electrical current, the magnetic field is neutralized and the held part is freed. Due to this principle, these holding solenoids are preferably used where long holding times are required and the device is switched on for short times only. In our case, this is while the impactors are being thrown.

The product *EPPM-3529-24-020* from company *Selos* [51] was chosen as the most appropriate. The electromagnet is supposed to be mounted via an M5 inner thread. The maximal holding force of this solenoid is $300\ N$, so the maximal weight, which this permanent magnet could hold in a straight vertical direction, is:

$$m = \frac{F}{g} = \frac{300\ N}{9.807\ m \cdot s^{-2}} = \mathbf{30.59\ kg} \tag{6.1}$$

which is far greater than the maximal potential weight of any pedestrian protection impactor.

Although the electromagnet solution is elegant, there are two issues we have to tackle. The first problem is with an impactor's material. As prescribed in regulations (chapter 2.4.4), the impactors are manufactured from aluminium alloy, which, naturally, is not ferromagnetic, so they would not react to the solenoid magnetic forces.

To overcome this problem, a special change in the impactors' design was suggested. See chapters 6.2.3.2 and 6.3.1.3.

The second problem concerns the charging and the neutralisation of the electromagnet's magnetic field. After connecting the circuit to the laboratory's $24\,V$ DC network and charging the permanent magnetic solenoid with a current, the electromagnetic field does not disappear immediately but is gradually weakened by an exponential dependency. This phenomenon is called transient response. The issue is important to tackle because the residual magnetic field might, because of its magnetic forces, affect the impactor during the acceleration process and therefore influence the required initial velocity.

The solution to this problem is to find the electromagnet's transient response rise time, which will be set in a controlling software of the throwing device. When the shot is supposed to happen (the pneumatic valve is opening and the piston of the pneumatic cylinder is advancing), a relay controlling the electromagnet is then switched on in advance (the advance equalling the rise time) to discharge the magnetic field so that the impactors are not affected. The issue is therefore to find the electromagnet's rise time.

Any transient response can be tested on an oscilloscope. To set the rise time, we connected the electromagnet to the source of 24V DC. To investigate the transient response, the power supply was switched on and off via a square wave pulse generator with a switching frequency of $100\,Hz$. The display of the oscilloscope device showed the transient response after every pulse from which it was possible to deduce the rise time, which was approximately $1\,ms$. Taking into account that the compressed spring will accelerate the impactor quite slowly, we can synchronize the moment of the release of the throwing mechanism with the charging of the permanent electromagnet to the same time without any influence on the impact's velocity.

6.2.3 Newly manufactured parts

Because of the assumed modification in the throwing device design, it is necessary to manufacture new parts. The newly manufactured parts are a new adapter for the impactors and a new cover for the old headform, which is available in Juliska laboratory.

These parts were produced by using internal resources and machines of the Juliska laboratory and were based on drawings, which are listed in Annexes.

6.2.3.1 Adapter for impactors

As it was decided to use a new electromagnetic system for the impactor's attachment, it was also necessary to design a new adapter so that we would be capable of mounting the electromagnet to the end plate. The final design is illustrated in Figure 6-6 and the drawing for production is listed in Annex VI.

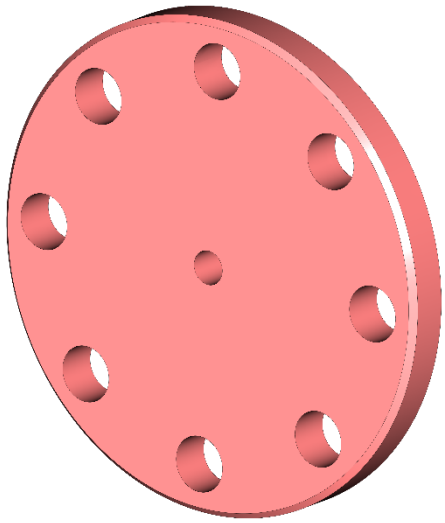

Figure 6-6 – CAD model of a new adapter for impactors.

The adapter is a simple product of a turning process with eight drilled holes for *M8x20* screws. The pitch diameter of the holes is $64\ mm$ and is the same as on the old adapter. The hole in the centre is intended for an $M5x20$ screw, which will hold the electromagnet. For improved assembly ability in the future, it would be convenient if the head of the $M5$ screw would be welded to the adapter, so that it would not be needed to hold the screw by a hex tool on the one side and screw electromagnet on the other. A photo of the finished manufactured part is possible to see in Annex X.

For replenishment purposes, the reader is referred to Annex VIII, where the assembly drawing of the new headform impactor connected via the electromagnetic system is illustrated.

6.2.3.2 New cover for the old headform impactor

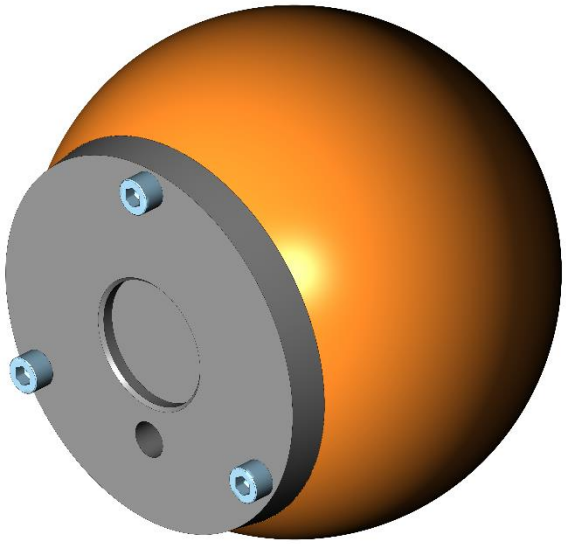

Figure 6-7 – A model of the old impactor with a new steel cover.

One chapter of the Zejda's master's thesis concerning the throwing device [37] concerns the design of the headform impactors which were used for pedestrian protection experiments. For internal purposes, only an adult headform was manufactured in accordance with the out of date standards. The design of the impactor was such as to be able to connect it to the old impactor's adapter via a toothpick mechanism. Because a new system of attachment of the impactor is used, it will not be possible to use this old impactor with the original aluminium cover. For this reason, a new steel cover for the old impactor was manufactured. The CAD model of the old impactor with a new cover is illustrated in Figure 6-7.

The cover is attached to the skull via three $M6x20$ screws. In the centre of the cover there is a cavity intended for the electromagnet and, under this cavity, there is a through-hole for accelerometer cords. One of the disadvantages of the old impactor is the impossibility of fitting the skin on it because the original design of the impactor was not adapted to it.

The drawing of the new cover is listed in Annex VII and the photo of the final manufactured product is shown in Annex XI. For additional information, the reader is referred Annex IX where the assembly drawing of the old headform impactor with the new steel cover is shown.

6.2.4 Electronic sensors and other equipment of the throwing device

One of the tasks concerning the throwing device's modernisation is the selection and mounting of new sensors required for measuring multiple parameters. Originally, the only electronic sensors used within the device were proximity switches for electromotors and an accelerometer in the headform impactor required for the HIC value calculation.

The impact angle was measured by a plumb-bob with an angle scale ruler used as an inclinometer. The initial impact velocity was indirectly determined by a ruler showing the coil spring compression rate which is proportional to the initial velocity by the following formula: [46]

$$v = \sqrt{s\left\{\frac{k}{m}\cdot s + 2\cdot g\cdot\cos(90° - \alpha)\right\}} \tag{6.2}$$

Where v is the initial velocity of the impactor accelerated by the potential energy of the deformed spring, s is the spring's compression rate, k is the spring's stiffness, m is the total weight accelerated by the spring (the impactor with a section of the throwing frame), g is the gravity of the Earth and α is representing the impact angle. The gravity itself might influence the impact velocity and impact angle by altering the impactor's trajectory during the free flight state. The regulations [3], [13] describing the execution of pedestrian protection tests state that this effect has to be taken into account. The reader is referred to a Bachelor's thesis [47] by Jakub Ryška where all the corrections minimizing the effect of Earth's gravity are presented.

The task was therefore to replace these rulers by a digital inclinometer and a proximity sensor, which are both suitable for modern systems of data acquisition. Another advantage of using the electronic sensors is in the simple writing of the recorded parameters directly into the testing protocol via the acquisition software.

6.2.4.1 Measuring the spring compression rate

There are many ways to measure the spring compression. For our application, distance sensors are the most suitable to use. Unfortunately, due to the construction of the device, the space where this sensor could be mounted is very limited. One of the possibilities is to attach the sensor to the frame, which holds the throwing mechanism (see Figure 6-8) and to measure the position difference between the frame and the parts which are about to move when the spring is compressed. For the purpose, a linear magnetic encoder commonly used on the turning machine would be suitable. Unfortunately, after a closer inspection of the frame, it became clear that there was not enough space to fit this sensor.

Another option is to mount the sensor on the front face of the frame and measure the distance to the end plate, which will be equal to the compression rate. The consequent problem of this solution regards the adjustment of the end plate in order to make it suitable for measuring. The solution differs with the particular sensor used.

The original idea was to use a draw-wire displacement sensor, which measures linear movement by using a steel wire. The cable drum with one end of the cable is attached to a sensor element, which provides a displacement-proportional output signal, and the second end of the cable should be connected to the measuring part via an eye. The issue with this sensor is in the attachment of the eye to the end plate and, most importantly, the

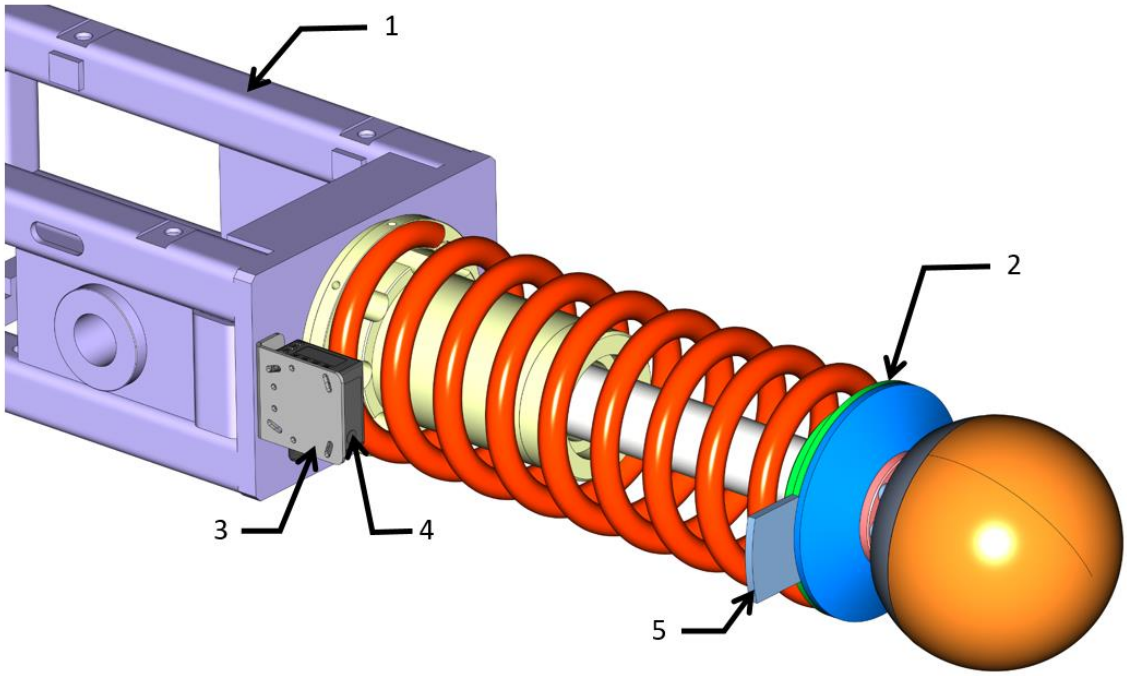

Figure 6-8 – Firing assembly of the sensor attached to the frame.

***1** – Firing mechanism frame; **2** – End plate; **3** – Adapter for sensor attachment;*
***4** – Laser distance sensor* - Banner LE250UQ; **5** – reflecting surface

maximal acceleration of the drum allowed, which will be exceeded many times during the spring release process.

The next option is the usage of a laser distance sensor whose function is based on the triangulation principle. The sensor's laser beam strikes the measured object like a small light dot. The photodiode receiver of the sensor detects the position of this dot. The angle of incidence changes according to the measured distance, and with it also the position of the laser dot on the photodiode. The integrated controlling hardware of the sensor accurately calculates the angle from the position of the laser beam on the photodiode and thereby it is possible to determine the distance to the measured object. [52] The disadvantages of this solution is greater financial expenses and a need for a reflection surface. Another drawback of these sensors is a measurement error, which increases with together with distance.

Multiple companies are manufacturing these types of sensors, but it is important to carefully select a suitable type. First, it was necessary to determine the possible measurement range from the free length of the coil spring and the maximal spring compression rate allowed. According to Zejda's thesis [46], the free length of the spring is 400 mm and the maximal compression of the spring allowed is 190 mm. Concerning the 70 mm length of the sensor, the maximal measured distance possible is $L_{max} = 400 - 70 = \mathbf{330\ mm}$ and the minimal measured distance is $L_{min} = 400 - 190 - 70 = \mathbf{140\ mm}$. The measurement range of the chosen sensor must thus be at least 140 mm to 330 mm.

The first sensor chosen was *Baumer OADM 1317480/S35A*. [53] This sensor has a measurement range of 50 mm to 550 mm and the linearity error at measuring the distance of 350 mm is $\pm 1.5\ mm$ and decreases with decreasing measuring distance.

Therefore, the accuracy would be sufficient. This sensor seemed suitable for our application but, unfortunately, the price of this sensor was above our modernisation budget.

Figure 6-9 – Banner *LE250UQ [54]*

The second, significantly cheaper, option is a sensor from the company *Banner* called *LE250UQ* [54], shown in Figure 6-9. The minimal measuring distance of the sensor is $100\ mm$ and the maximal seeing distance is $400\ mm$, so this sensor is suitable for our purposes. The measurement accuracy is constant $\pm 0.4\ mm$ until the measuring distance of $250\ mm$. Beyond, it linearly increases up to the maximal measurement error of $\pm\ 1.0\ mm$, found at the maximal limit of the measuring range. The output of the sensor is either an analog $4 - 20\ mA$ or $0 - 10\ V$. In accordance with the consequent data acquisition hardware, the analogue voltage output was chosen.

The combination of better accuracy and the approximately three times cheaper price in comparison with the previous sensor makes the *LE250UQ* a perfect choice for our application.

The sensor will be attached to the throwing frame front face via an L-shaped adapter (Figure 6-8, titled 3), which was manufactured in our laboratory workshop. The reflection surface (Figure 6-8, titled 5) was 3D printed in the *Porsche Engineering's* workshop and connected to the end plate (Figure 6-8, titled 2) via an adhesive glue. The only requirement for this glue connection is to resist the inertia forces arising from the throwing process.

6.2.4.2 Inclinometer

Figure 6-10 – IN360A [55]

The next sensor used for advanced controlling of the throwing process is an electronic inclinometer. This device will replace the old plumb-bob ruler. The advantage of using this device is the direct transmission of the impact angle to the analog output signal. For this purpose, an inclinometer *IN360A-115* [55] with a measurement range $0 - 360°$ in one measuring axis and with $\pm 0.20°$ accuracy was chosen. One of the disadvantages of using this sensor is that it would not be using the full range of our laboratory voltage signal input module. This inclinometer has a signal output range of $0.5\ V$ to $4.5\ V$ while our input voltage module has a range of $-10\ V$ to $10\ V$. This problem could be tackled by simply offsetting the output signal to the full module range.

This sensor will be attached to the throwing frame via screws in a position of the formal plumb-bob ruler.

6.2.4.3 Laser pointer for target point location

The next piece of equipment required for correct experiment execution is a laser pointer, which will be pointing at the desired target point location. This equipment is necessary in order to be able to aim at the tested part.

The arrangement of this laser pointer is illustrated in Figure 6-11. The laser pointer (5) itself is inserted into the 3D printed adapter (6) which is mounted to the impactor' adapter (2) via the same $M5$ screw as in the case of the attached electromagnet. The inner thread in the pointer adapter is cut out using a tap tool and the charging cords are pulled out through a hole in the adapter's surface.

The laser pointer, specifically the *Picotronic 70104127* [56], will be charged by two AA 1.5 V batteries, which will be placed in a purchased double AA battery holder (4). This holder will be attached with glue to the 3D printed battery holder adapter (3) which is connected to the impactor's adapter (2) by two $M8$ screws.

For accurate determination of the target point, it is important to ensure concentricity of the laser beam with the longitudinal axis of the spring. This could be done using a longer M5 centric crews and making sure that the contact surfaces between the adapters are even.

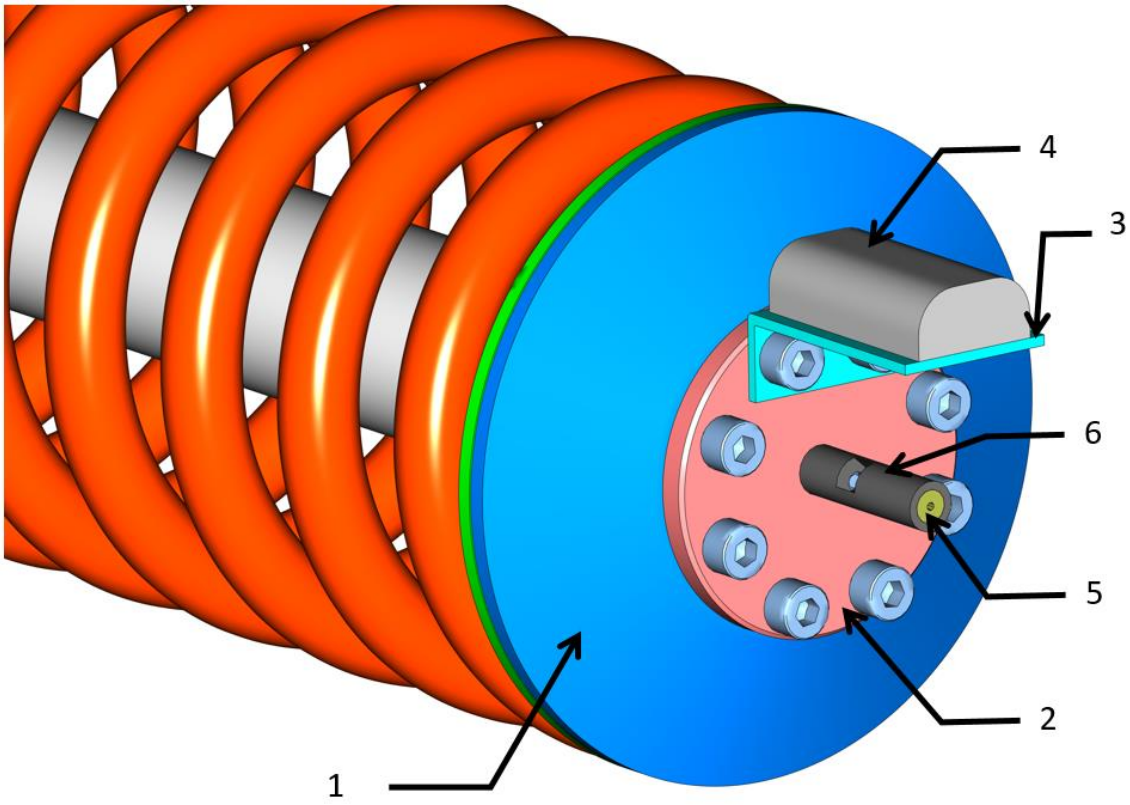

Figure 6-11 – Illustration of the laser pointer arrangement.

***1** – End plate; **2** – Impactor's adapter; **3** – Battery holder adapter; **4** – Battery holder; **5** – Laser pointer; **6** – Laser pointer adapter*

6.2.4.4 Headform accelerometers

While completing the throwing device in the year of 2004, three triaxial accelerometers *Entran EGCS3-D* [57] with ranges of $10g$, $100g$ and $500g$ intended for old headform impactor were purchased for experimental purposes. One of the main advantages of making this sensor suitable for crash applications is its critical damping ratio. In other words, this sensor is capable of damping the oscillations of the seismic mass to protect itself from exceeding the allowed acceleration range. The disadvantages of this accelerometer are higher purchase costs related to critical damping property and its cords, which are firmly connected to the sensor's body.

Unfortunately, while inspecting the $500g$ accelerometer, it was found out that one of the cords was damaged and, therefore, the sensor was not capable of measuring correctly. Due to the firm connection of the cords, it was not possible to repair this corruption and it was thus necessary to purchase a new accelerometer.

Selecting the accelerometer was a difficult task because we were looking for an accelerometer with a critical damping ratio intended for shock (impact) application. The first idea was to purchase the same type as before, but the cost was not acceptable given our project budget.

Figure 6-12 – The 64X-2000-360 accelerometer. [58]

To lower expenses, it was decided to purchase three cheaper, underdamped, uniaxial accelerometers *64X-2000-360* from the supplier *TE Connectivity* [58] illustrated in Figure 6-12. This sensor was chosen on the recommendation of the *Euro NCAP's* Technical Bulletin concerning suitable accelerometers with required damping characteristic for pedestrian protection testing. [59] The range of this sensor is specifically chosen to be $2\,000\ g$ in order to protect the sensor from exceeding the allowed limits while testing some very stiff entities. The limitation of measuring only along one axis is one of the advantages of this sensor because in the case of a defect, only one sensor must be replaced, which is far less expensive than purchasing a new triaxial accelerometer. Although the regulation [13] requires the usage of an accelerometer with the CAC of $500\ g$, we decided to use a sensor with higher CAC because of a recommendation from the *Euro NCAP*. Each of these three sensors will be measuring acceleration along one axis and they will be attached to the headform impactor by a mounting block. See chapter 6.3.1.5 where the design solution is described in detail.

6.2.4.5 Impact velocity measurement and verification

The next requirement for correct pedestrian protection crash test realization is the measurement of the headform impact velocity, which must meet a $\pm 0.2\ m \cdot s^{-1}$ tolerance. Newer, advanced throwing devices use a hydraulic propulsion system with closed-loop control system, which allows perfect speed control during the acceleration process until the free flight of the impactor. The control feedback is provided by an accelerometer mounted on the launcher's piston rod. This system is able to adjust the launching acceleration in real-time. [60]

Unfortunately, the propulsion system of our throwing device is not capable of using the same closed-loop control system so the impact velocity measurement will have to be

executed differently. The accelerometer mounted in the headform measures acceleration during the whole testing period, not only after the impact. Taking advantage of this, it is possible to use the measured acceleration signal and afterwards integrate the acceleration course by time to obtain the velocity vs. time history. Figure 6-13 illustrates a snapshot of the exemplary course of the impactor's acceleration and velocity during the acceleration phase. From the figure, it is evident that the impact velocity was laid down at $35\ km \cdot h^{-1}$.

This system of impact velocity integration seems applicable and the biggest advantage of it is that there is no need to purchase and mount any additional sensors.

Even though the proposed velocity-measurement system is supposed to provide accurate outputs, the results need to be verified. For this purpose, a high-speed camera with an appropriate post-processing software, which would be capable of tracking the headform impactor during the acceleration and free flight phase, will be used. This way, it will be found out whether the described velocity measurement is accurate or not.

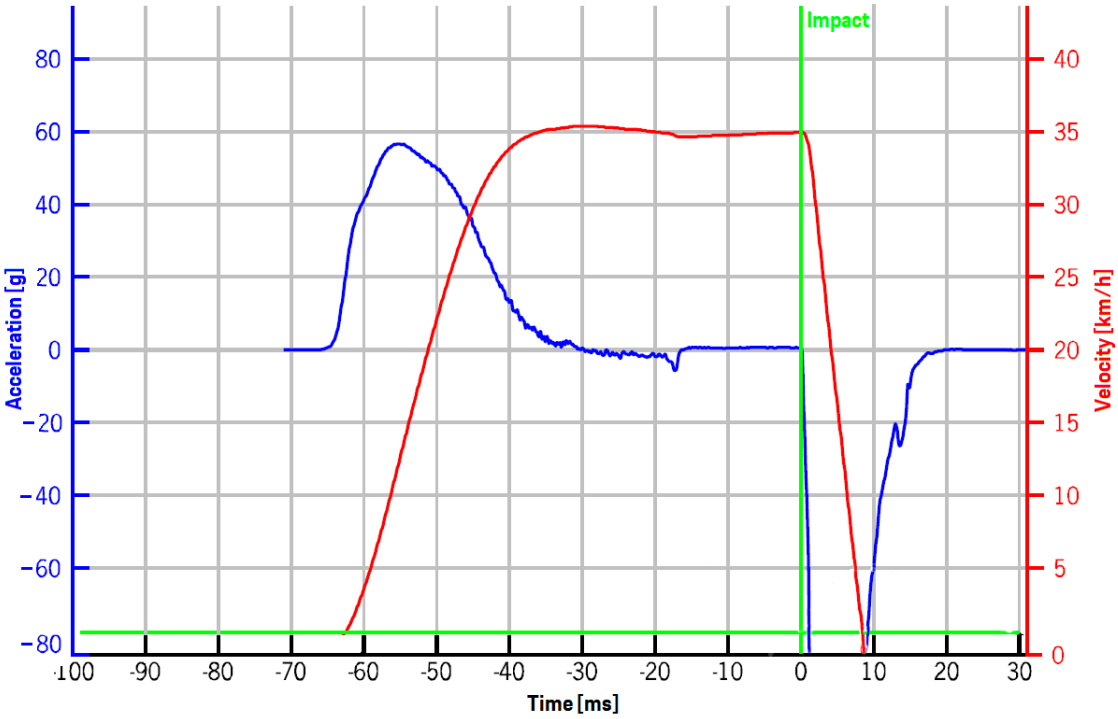

Figure 6-13 – Acceleration and velocity vs. Time history of an exemplary headform test. For the purposes of this chapter, only the first phase of the test is shown.

Another way to verify the impact velocity could be done via an accurate radar gun or by an advanced post-processing process of the standard quality video recording. This approach, proposed in a master's Thesis by Denys Rozumnyi [61], is called Tracking by Deblatting and is based on the observation of the motion blur arising when an object moves across non-negligible distance during the exposure time of a single frame. The motion blur is directly related to the intra-frame trajectory of an object and it is therefore possible to determine the object's trajectory, velocity and acceleration precisely.

6.2.5 Data acquisition

6.2.5.1 Data acquisition hardware

To collect all the measured data, an acquisition system was set up. The basis for acquisition is a four-slot USB chassis *CompactDAQ 9174* [62] from *National Instruments*. In this cDAQ, a *C Series NI-9237* [63] module for recording data from the accelerometers will be inserted. The 24-bit resolution together with the maximal $50\ kS/s$ per channel sampling speed ensure sufficient accuracy of the measurement. The input connectors to this module are the *RJ50* type so the cords from accelerometers must be adjusted accordingly. The next module for recording voltage output sensors is *NI-9205* [64]. The inputs for this module are data recorded from the laser distance sensor and the inclinometer. The sampling rate of $250\ kS/s$ on the 32 single-ended or 16 differential channels of this module will be more than sufficient for our purposes. The charging of the electromagnet and the switching-on of the pneumatic valve in control of the pneumatic cylinder will be performed via a 4-channel *NI-9472* [65] digital output module. Both of these devices have a charging voltage of $24\ VDC$ so the maximal switching voltage of the relay module of $60\ VDC$ will be sufficient.

The outputs from the CompactDAQ will be brought to the laboratory PC for subsequent data acquisition via a NI LabVIEW software.

6.2.5.2 NI LabVIEW acquisition software

To acquire and evaluate the measured data, a LabVIEW task was created by a colleague Ing. Martin Kovář. This software is primarily used for measuring acceleration vs time history from each uniaxial accelerometer and computing the resultant magnitude of acceleration which will be used for subsequent HIC calculation. Secondarily, the software is also capable of time integration of the acceleration signal used for impact speed verification and of recording the spring compression rate and inclination of the device from the appropriate sensors before the throwing.

The user interface of the software is illustrated in Figure 6-14. In the top right corner it is possible to see values from distance and inclinometer sensors and to choose the type of test desired and the headform impactor used. This software is further capable of computing the assumed initial velocity of the impactor according to the formula (6.2). The inputs for this function are the above-mentioned distance and inclination of the throwing frame.

Before executing the shot itself, it is first required to initialize the measurement. This is done by pressing the initialize button in the top left corner. Afterwards, the software will prepare the required files for recording and write the test specification into them.

The second step consists of pressing the start button, which will execute the release of the impactor. Before doing this, the software will discharge the electromagnet in advance to prevent influence from the magnetic force. The last step consists of time integration of the measured data for consequent impact velocity verification. This could be done by pressing the evaluate button.

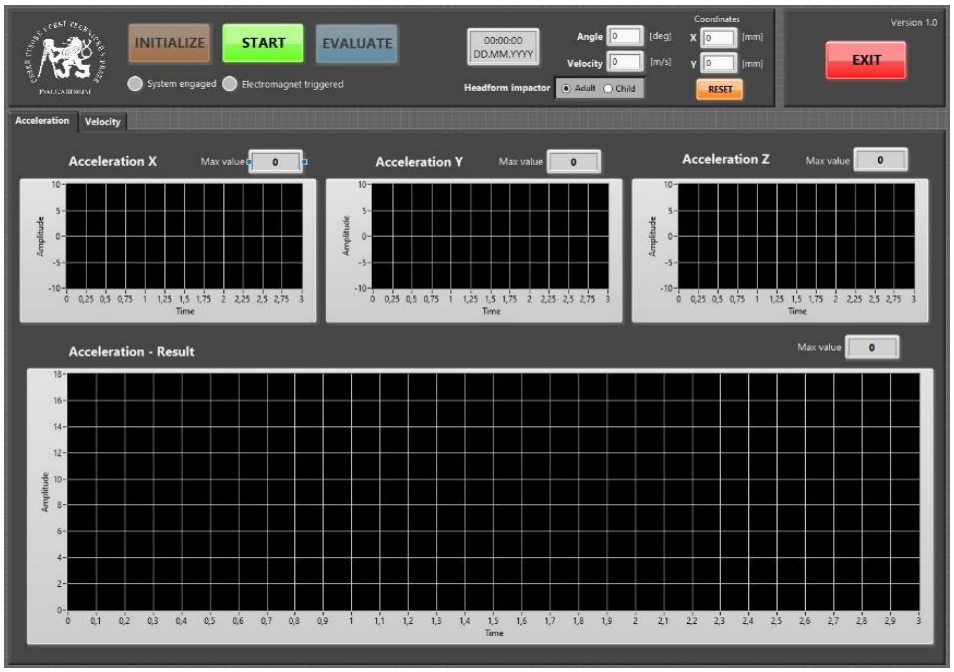

Figure 6-14 – Interface of the LabVIEW acquisition software.

After we obtain the recorded data, it is needed to calculate the HIC values, which is quite difficult. Because of this, the post-processing of the measured data will be probably done within a *DIAdem* software.

6.3 New headform impactors

So far, the device is prepared to perform pedestrian protection tests using only the old adult headform impactor due to a newly manufactured steel cover. To perform experiments with contemporary equipment, it was necessary to purchase or to manufacture new impactors corresponding to the contemporary regulations. [13]

There are multiple suppliers who are selling the crash tests equipment as well as pedestrian protection impactors. The *CTU's Faculty of Mechanical Engineering* asked three manufactures; *Humanetics*, *Cellbound* and *Jasti*. Although it would be an easier solution to simply purchase both the adult and the child headform impactors, to lower costs, it was decided to design and manufacture our own headform impactors using a machining centre located in the laboratory of *Department of Machining, Process Planning and Metrology*. The only part which must still be purchased is artificial skin because the Faculty does not posses the technology for its production. In the first phase, the adult headform impactor was designed. The child headform impactor was designed later.

6.3.1 Design of the adult headform impactor

The supporting document for the new design was *Part V* of the *Annex* of *Commission Regulation No 631/2009* [13] (also see chapter 2.4.4) where the requirements for headform impactors regarding dimensions, physical parameters and functionality are described. The design was performed in CATIA V5 software, using a dimensions parametrisation from an Excel file to optimize the impactor's parameters.

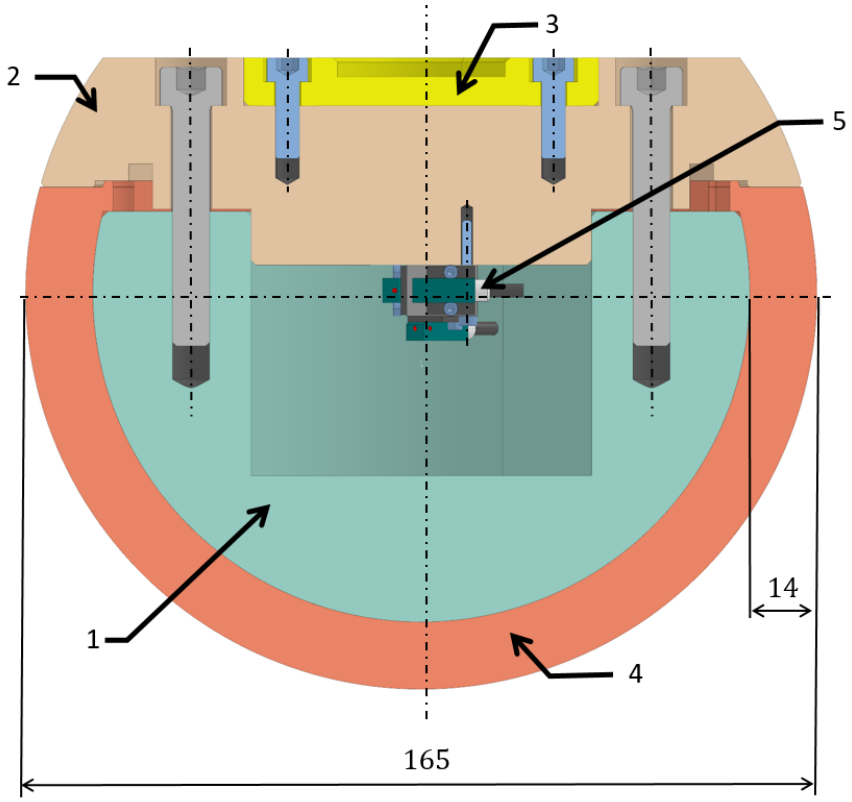

Figure 6-15 – Angled cross-section view of the adult headform impactor.

***1** – Skull; **2** – Cover; **3** – Adapter for electromagnet; **4** – Skin; **5** – Mounting block with accelerometers*

The assembly of the impactor, illustrated in Figure 6-15 consists of a skull, a cover, an adapter for electromagnet, a purchased skin, accelerometers and screws.

6.3.1.1 Impactor's skull

The skull is a spherical object with a diameter of $\emptyset 137\ mm$ made of aluminium with a cut in the rear section. Inside the sphere there is a recess intended for positioning the accelerometers. At the flat surface there are six blind thread holes for screws, which attach the cover to the skull.

The calculated weight of the skull is $1\ 950\ g$, which is almost half the mass of the whole impactor. The snapshot from the CAD software illustrating the design of the skull is illustrated in Figure 6-16.

6.3.1.2 Impactor's cover

The back end of the headform impactor is shown in Figure 6-18 and Figure 6-19. This is the most complicated part of the impactors assembly. The cover is attached to the skull via 6 hexagon socket head cap screws $M8x50$ (*ISO 4762*). The inner crown of holes is intended for attaching an adapter for the electromagnet. The cover is manufactured from aluminium which is not ferromagnetic. As a result, the throwing device's electromagnetic attachment system would not be functional. To solve this issue, an adapter made from steel is mounted to the cover's front recess (see Figure 6-15) via five hexagon $M5x16$ screws. The sixth hole in the recess with a greater diameter than other holes is intended for passing the cords from the accelerometer out of the impactor.

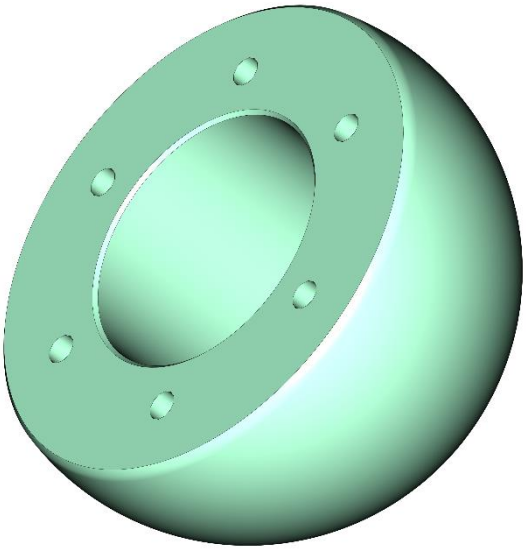

Figure 6-16 – Illustration of the impactor's skull.

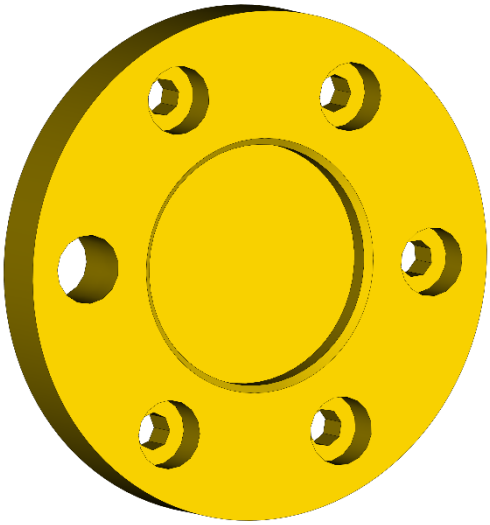

Figure 6-17 – Illustration of the adapter for the electromagnet.

A security steel wire is used to restrict the movement of the impactor after a rebound from the tested part. The wire is placed in the looped groove of the cover and taken out through a hole on the edge. The second end of the wire is attached to the throwing device frame. On the inner surface of the impactor are located two $M2$ thread holes for mounting the block with accelerometers.

The dimensions of the cover are designed in such a way to create pressure on the top surface of the pliable rubber skin. This way, it is ensured that the skin does not slip and is firmly pressed between the cover and the impactor' skull.

6.3.1.3 Adapter for the electromagnet

The design of the adapter for the electromagnet is shown in Figure 6-17. It is a flat round product of a turning process intended to be fit into the recess at the outer side of the cover and connected via five $M5$ screws. On the one side of the adapter there is a recess of a diameter of $\emptyset 29\ mm$ for attaching the electromagnet. Because of this, it is required to manufacture the adapter from a ferromagnetic material. The only not counterbored hole is intended for passing the cords from the accelerometers.

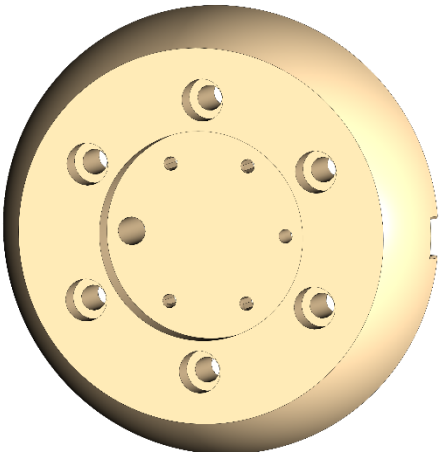

Figure 6-18 – Impactor's cover. Front view.

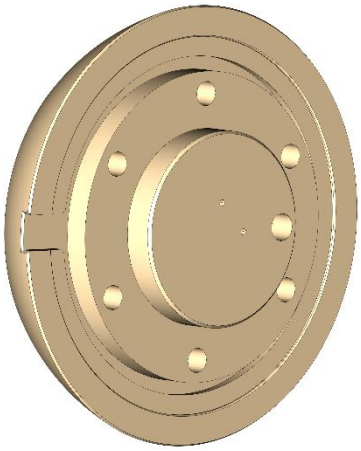

Figure 6-19 – Impactor's cover. Back view.

6.3.1.4 Artificial skin

This is the only part that we are not capable of manufacturing using our own resources. Because of this, it is required to purchase it from an external manufacturer. See chapter 6.3.3 for more details

Because it is necessary to meet the mass requirement of the whole assembly, it is necessary to know the weight of the skin. The topology and the assigned density of the modelled part could be different from the reality so it is not possible to use the CAD data. Therefore, the only reliable way to accurately find the skin mass is to physically weigh the skin after purchase, which weighs $776\ g$.

In order to have the same weight of the skin in the impactor assembly, the assigned density was calculated from the model volume of $662.85\ cm^3$. The density, which was subsequently inputted into the CAD model, is therefore:

$$\rho = \frac{m}{V} = \frac{776\ g}{662.85\ cm^3} = 1.170\ \frac{g}{cm^3} = \mathbf{1\ 170}\ \frac{kg}{m^3} \tag{6.3}$$

6.3.1.5 Mounting block for accelerometers

A steel mounting block is used for attaching the accelerometers to the impactor's cover. This accessory could be purchased together with the accelerometers from the same supplier, but for expenses saving was decided to manufacture this block in the workshop of our laboratory.

This block is a simple prism with dimension illustrated in Figure 6-21 and with two $\emptyset 2.5$ holes for $M2$ screws. Each of the three accelerometers is attached to the block via two $M1.6$ screws. The manufacturing drawing of this part is listed in Annex XII.

*The Commission Regulation No 631/*2009 [13] lies down the requirements for mounting accelerometers to the impactor assembly to ensure accurate measurement. The requirements concerning the location of the seismic mass are:

"*A recess in the sphere shall allow for mounting one triaxial or three uniaxial accelerometers within ±10 mm seismic mass location tolerance from the centre of the sphere for the measurement axis, and ±1 mm seismic mass location tolerance from the centre of the sphere for the perpendicular direction to the measurement axis*."

And the positioning of the accelerometer shall be in accordance with the subsequent paragraph:

"If three uniaxial accelerometers are used, one of the accelerometers shall have its sensitive axis perpendicular to the mounting face A (Figure 2-23) *and its seismic mass shall be positioned within a cylindrical tolerance field of 1 mm radius and 20 mm length. The centre line of the tolerance field shall run perpendicular to the mounting face and its mid-point shall coincide with the centre of the sphere of the headform impactor.*

The remaining accelerometers shall have their sensitive axes perpendicular to each other and parallel to the mounting face A and their seismic mass shall be positioned within a spherical tolerance field of 10 mm radius (in Figure 6-24 illustrated as yellow tolerance field). *The centre of the tolerance field shall coincide with the centre of the sphere of the headform impactor."* [13]

To ensure these legal conditions, strict requirements are laid down for block manufacturing process as is possible to see in the manufacturing drawing in Annex XII. These conditions mainly consist of geometrical tolerance of flatness, perpendicularity and hole positioning.

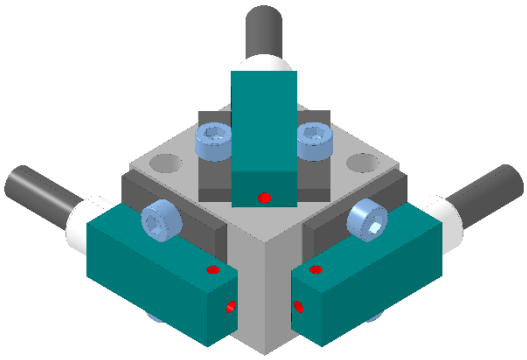

Figure 6-20 – Mounting block for three uniaxial 64x-2000-360 accelerometers.

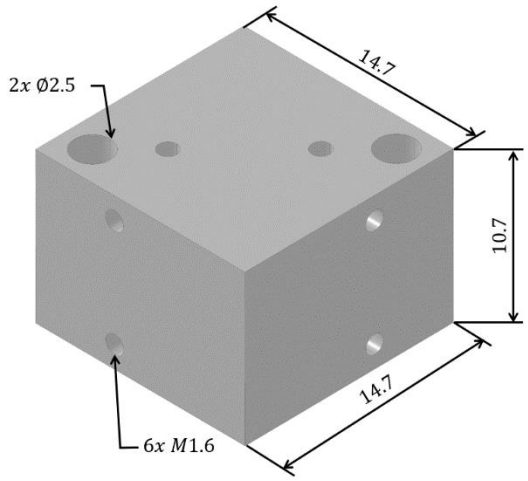

Figure 6-21 – Mounting block with dimensions.

6.3.1.6 Assembly of the adult headform impactor

The final design of the new adult headform impactor is illustrated in Figure 6-22.

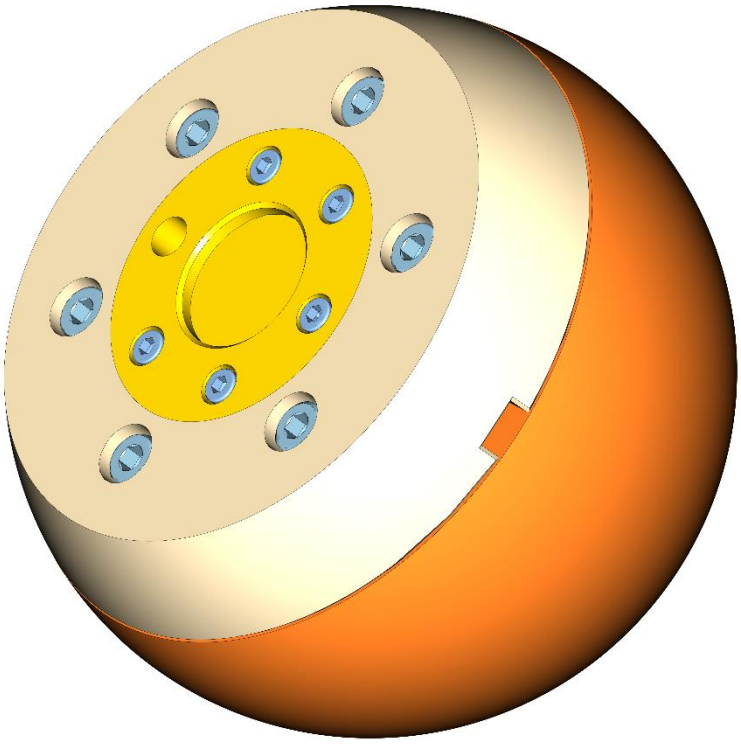

Figure 6-22 – Final design of the adult headform impactor.

Chapter 2.4.4 and Table 3 summarized the requirements regarding the design of the headform impactors. The final weight of the assembly including the accessories (screws, mounting block, accelerometers) is $4.525\ kg$ which lies within the tolerance limits. The weight is optimized slightly closer to the upper limit. In case the weight tolerance is not met, it would be possible to mill or drill off some material to meet the mass limits. The moment of inertia about an axis through the center of gravity and perpendicular to the direction of impact is approximately $0.0108\ kg \cdot m^2$ for both of the remaining axis because of the symmetry of the impactor. The moments of inertia also lie within the tolerance.

The distance between the impactor's center of gravity and center of the skull (in the model, the origin of the coordinate system) also lies in the $\pm\ 5\ mm$ tolerance.

$$d_{COG} = \sqrt{d_x^2 + d_y^2 + d_z^2} = \sqrt{(-0.109)^2 + (-0.018)^2 + 0.019^2} = \mathbf{0.405\ mm} \tag{6.4}$$

The mechanical properties of the assembly are possible to inspect in Annex *XIII*.

The specifications concerning the locations of the accelerometers' seismic masses were also checked. The seismic mass of the accelerometer measured in the direction of impact (direction *x*) is located $7.44\ mm$ from the center of the skull, visible in Figure 6-24, and exactly $0\ mm$ from the remaining two directions (direction *y* and *z*). The seismic masses of the other two accelerometers are located $5.577\ mm$ from the center of the skull in the

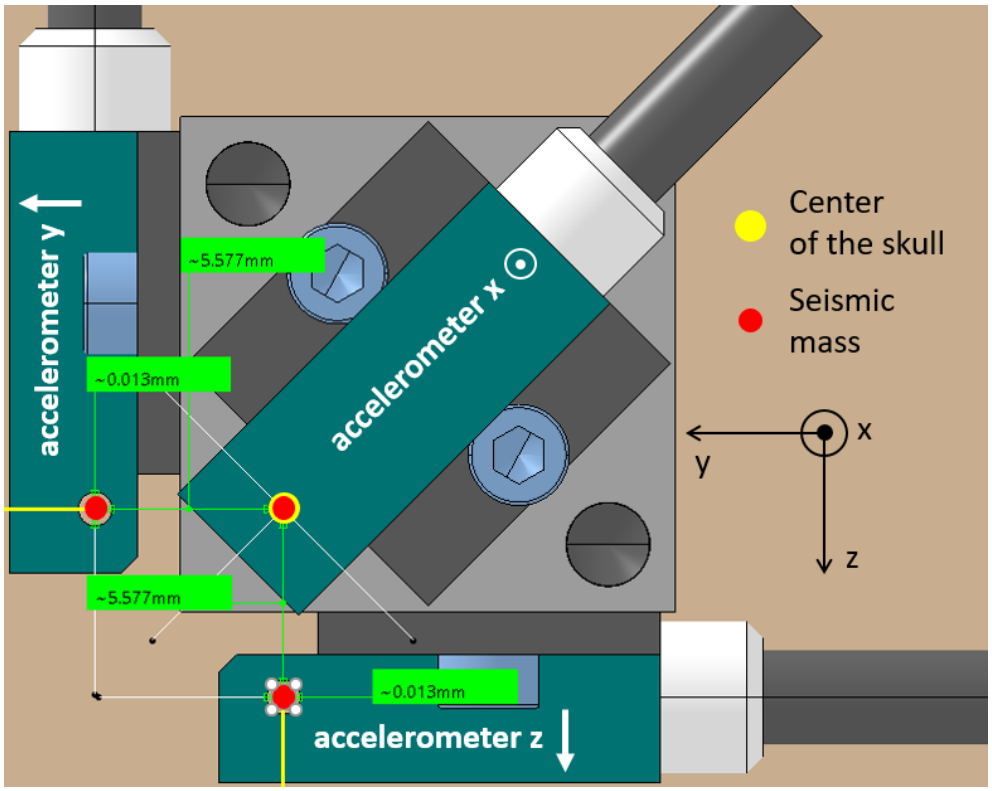

Figure 6-23 – Dimensions between the center of the skull and the seismic masses of the secondary accelerometers. The third dimension (not visible from this view) is 0.050 mm. The arrows indicate the measurement direction.

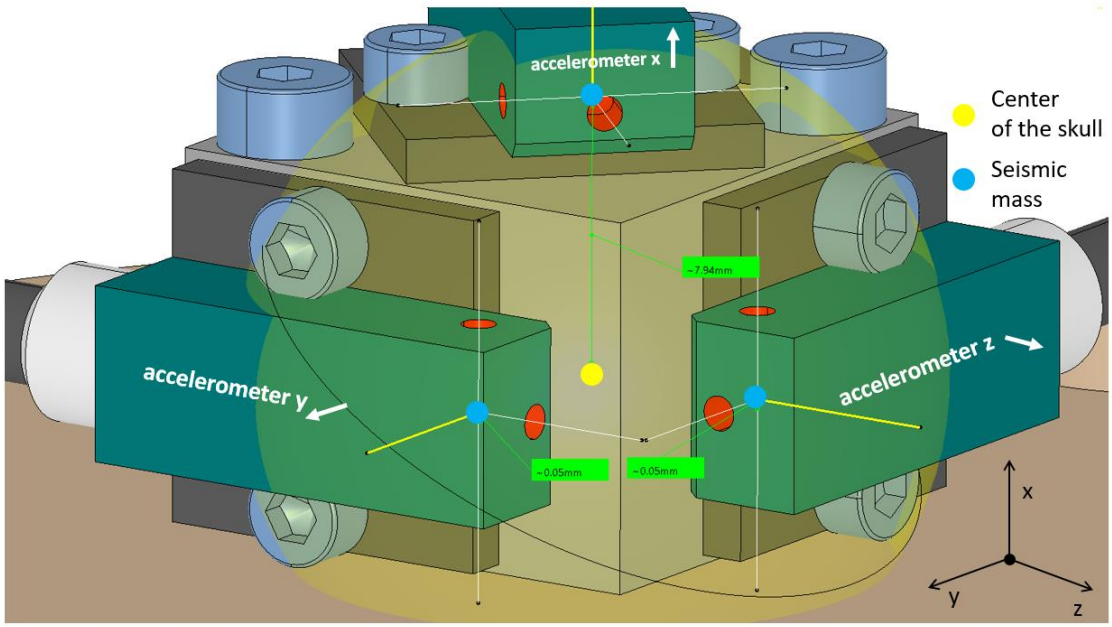

Figure 6-24 – Positioning of the accelerometers in accordance with the center of the skull. The yellow sphere is illustrating the tolerance field for positioning the seismic masses.

direction of measurement, $0.050\ mm$ away from the skull's center in the direction of impact (direction *x*, visible in Figure 6-24) and $0.013\ mm$ in the third direction. The arrangement of the accelerometers is illustrated in Figure 6-23.

The requirements concerning the positioning of the accelerometers were checked using an illustrated spherical tolerance field with a radius of $10\ mm$. The outcome is possible to inspect in Figure 6-24. From the snapshot is visible, that the seismic masses of all three accelerometers are located in the tolerance defined by the regulation.

In both cases, the regulation's requirements concern the positioning of the accelerometers as well as the weight and the moment of inertia fulfilled. Therefore, the new adult headform impactor should be capable of accurate measurement according to the standards.

The performance of the new adult impactor could be verified via an in-house built dynamic drop certification test. This experiment will be a subject of future research.

6.3.2 Child headform impactor

The child headform impactor's assembly is similar to the adult impactor. These two assemblies will use the same artificial skin and adapter for the electromagnet. For these purposes, the design of the skull and the cover are almost the same. The only differences are in height of the cover and the shape of the skull's recess to remove the superfluous $1\ kg$ of the weight difference between the two types.

Another difference concerns the diameter of screws connecting the cover to the skull. Instead of $M8x50$, six $M6x50$ hexagon socket head cap screws are used, again, to save weight. The angled cross-section of child headform impactor is illustrated in Figure 6-25.

The final weight of the child headform impactor assembly including the accessories (screws, the mounting block, accelerometers) is $3.515\ kg$, which lies within the tolerance limits. The weight is again optimized slightly closer to the upper limit for the same reasons. The moment of inertia about an axis through the center of gravity and perpendicular to the direction of impact is approximately $0.0085\ kg \cdot m^2$ for both remaining axis because of the symmetry of the impactor. The moment of inertia also lies in the tolerance field described in Table 3.

The distance between the impactor's center of the gravity and center of the skull lies again in the $\pm\ 2\ mm$ tolerance.

$$d_{COG} = \sqrt{d_x^2 + d_y^2 + d_z^2} = \sqrt{0.457^2 + 0.013^2 + 0.025^2} = \mathbf{0.458\ mm} \qquad (6.5)$$

The mechanical properties of the child headform impactor can be inspected in Annex XIV.

Naturally, the mounting block with a set of accelerometers will be used for both impactors. The positioning of the accelerometers within the child impactor is exactly the same as in the case of the adult impactor. Because of that, it is not necessary to repeat the procedure and it is ensured that the accelerometers are in the correct position.

The manufacturing of the child impactor is supposed to begin after the production process of the adult headform impactor is finished. Subsequently, in-house dynamic certification drop test for evaluating the performance of the impactor with the purchased skin will be performed.

If the new impactor meets the dynamic certification requirements, then it will be possible to manufacture the second, child, impactor. After that, our laboratory will have the basic equipment necessary to conduct the pedestrian protection tests.

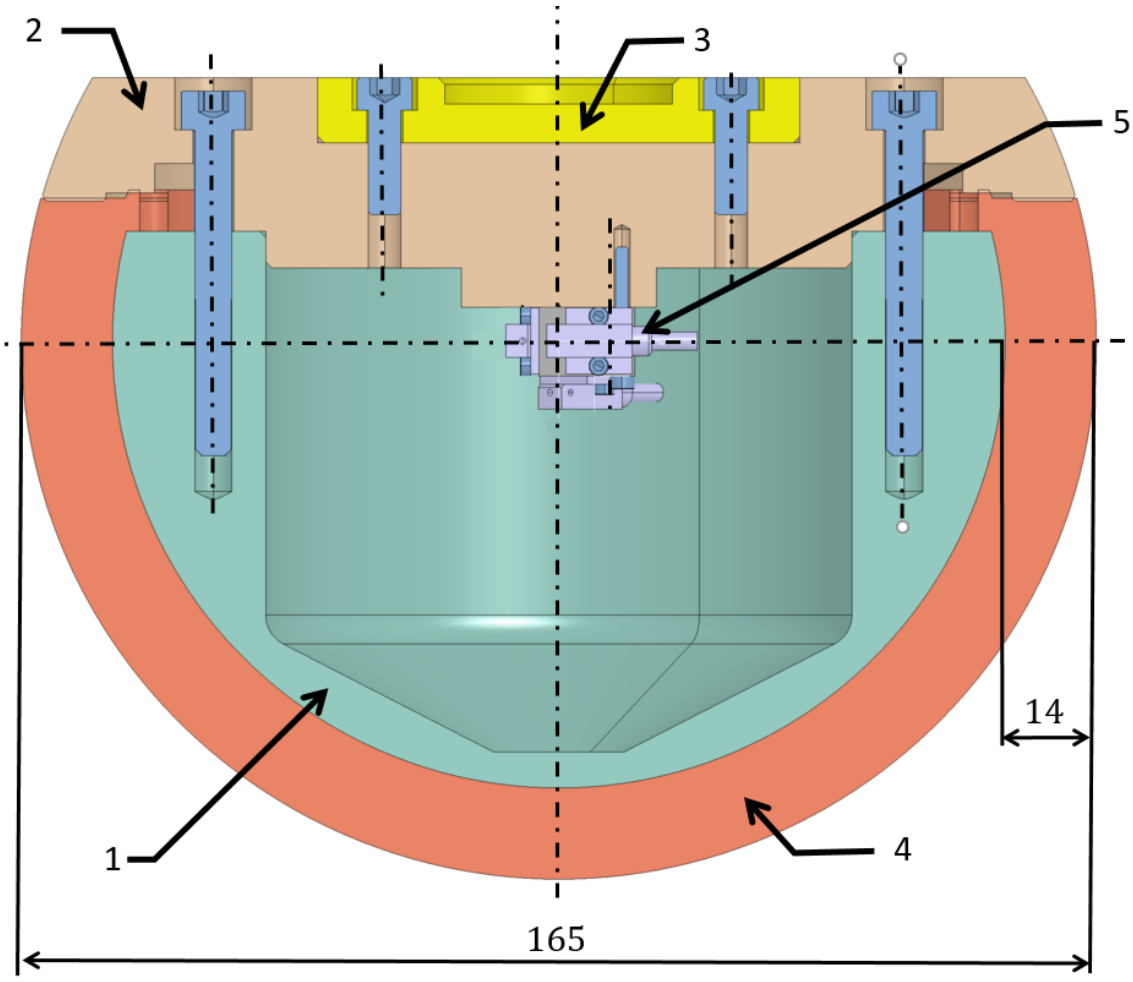

Figure 6-25 – Angled cross-section view of the child headform impactor.

.

***1** – Skull; **2** – Cover; **3** – Adapter for electromagnet; **4** – Skin; **5** – Accelerometers with mounting block*

6.3.3 Skin purchase

Figure 6-26 – Photo of the skin acquired from Cellbound.

Most of the suppliers offering pedestrian protection equipment sell accessories for various impactors. For our purposes, it is required to acquire artificial skin, because it is the only part of impactor's assembly, which we are not capable of manufacturing on our own. To compare and choose the most suitable and least expensive skin, three suppliers were approached.

The most expensive offer came from a Japanese company *Jasti*, followed by the largest manufacturer of the crash application equipment – *Humanetics*. The last supplier contacted with the lowest price was a British manufacturer *Cellbound*. It was therefore decided to purchase the skin from this company.

The skin was shipped together with a certificate of conformity, proving the adequate behaviour in the certification drop test performed by the manufacturer. This certificate also contains the skin's exact weight, which is one of the required inputs for the CAD models of the new headform impactors.

The skin was subsequently used to verify the correct design of the new impactors' CAD models. This was done by putting the skin on the 3D-printed prototype of the adult headform and observing the dimensional compatibility.

6.3.4 3D printing process of the adult headform impactor prototype

Even though the decision to design our own impactor saved great expenses otherwise required for purchasing new impactors from the suppliers, the cost of manufacturing is still not negligible. To avoid repeating the production process due to design errors, a 3D-printed prototype of an adult headform impactor was produced in *Porsche Engineering* Service's workshop. The next purpose of this prototype is to verify the dimensional compatibility between the new impactor's CAD model and the artificial skin purchased. The three parts of the adult headform impactor model were printed on a *Prusa i3 MK3* [66] 3D printer using an FDM (Fused Deposition Modelling) method which is at the moment the most commonly used technology for 3D printing, based on depositing melted printing material in pre-determined paths layer by layer. [67]

The process of producing the 3D-printed part could be divided into a few steps. First, it is important to convert the CAD model to a file type (for example *.stl) which is possible to read with the software responsible for preparing the printing process itself. In our case, we used a software called *PrusaSlicer* from the printer's supplier. A snapshot from this software is possible to see in Figure 6-27. This open-source software sets the required adjustments for printing such as the orientation of the part, material used, the height of the layer, percentage of infill and accuracy of printing. After this, the model is exported to the *G-Code*, which is a coordinate code for the print head. The printing settings for all

of the three parts were set in such a way to shorten the printing time and the orientation of the parts on a printing pad was set such as to use as little support material as possible. The printing layers were 0.2 *mm* thick and the internal infill had a honeycomb shape with fill density of infill of 10%.

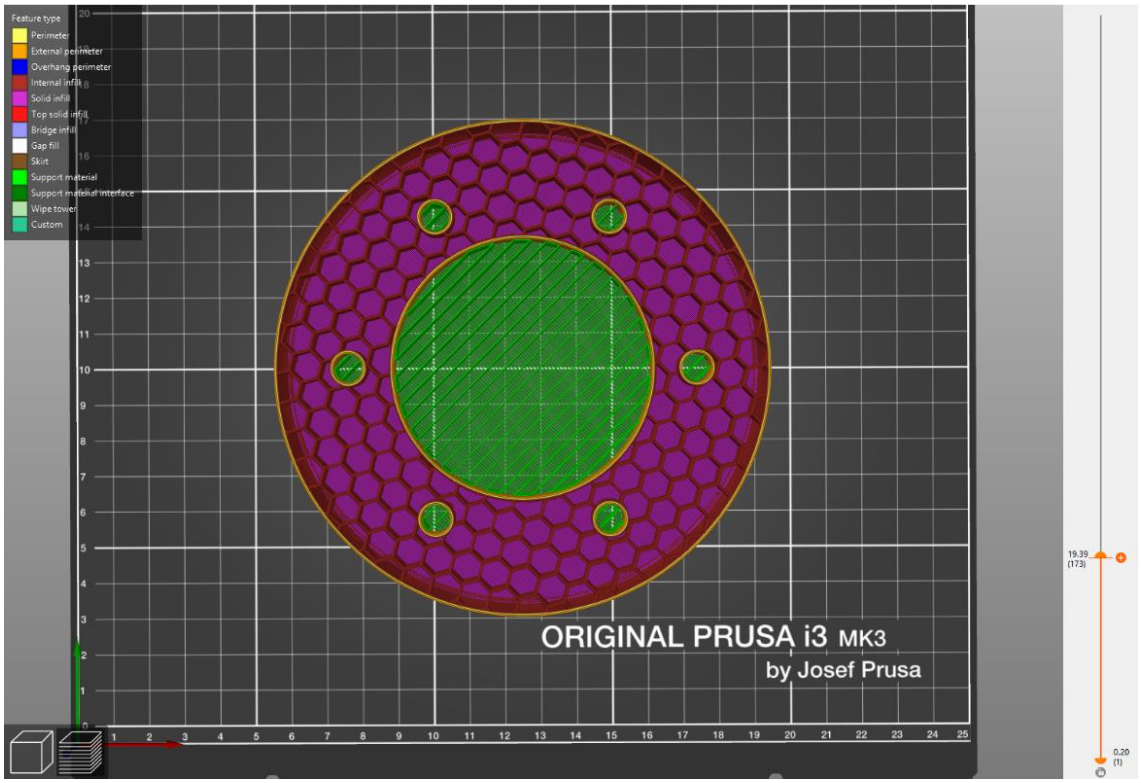

Figure 6-27 – Snapshot from PrusaSlicer software displaying a horizontal cross of the adult impactor skull. The yellow curves represent perimeters, the light purple area represents solid infill on the part's surface, the dark red honeycomb structures represent the internal infill and the green areas show where the support material is.

The chosen material for printing was PLA (polylactic acid) because of its low price and fast curing allowing shorter printing times. The disadvantage of this material, in comparison with other materials for 3D printers, is its poor properties. However, in this application, there are not any requirements for strength or heat resistance.

The result of the printing process is possible to inspect in Figure 6-28 – Photo of all the parts before assembly

Material used	218 *g*	165 *g*	19 *g*
Price	5.46 €	4.13 €	0.49 €

where the assembly of the printed adult headform impactor with purchased skin is displayed.

The total printing times and material expenses are listed in the following Table 11

After the printing process was finished, the inner thread in the cover and the skull was cut using a tap tool. Subsequently, the skin was put on the skull and the adapter with the skull were assembled together with the cover. The result is illustrated in Figure 6-29.

Table 11 – Overview of printing time, material used and price of the printed parts

	Skull	Cover	Adapter for electromagnet
Printing time	$18h\ 25min$	$13h\ 18min$	$1h\ 36min$
Material used	$218\ g$	$165\ g$	$19\ g$
Price	5.46 €	4.13 €	0.49 €

The prototype of the adult headform impactor showed a minor error which had to do with the height of one of the cover's edge. This defect was subsequently removed by a CAD model update. At the moment, the dimensional compatibility of the CAD model of the adult headform impactor together with the purchased skin has been checked. It is therefore possible to continue with the production of the adult headform impactor from aluminium.

The main advantage of this approach to producing the impactor prototype are the low overall expenses (about 10 €) and the possibility to check the CAD model of the impactor in reality. The disadvantages to using 3D printing technology are long production times (all together $33h\ 19min$) and almost no mechanical properties because of material used. Both of these drawbacks are nonetheless negligible.

Figure 6-28 – Photo of all the parts before assembly.

Figure 6-29 – Photo of the prototype with the skin.

6.3.5 Manufacturing of the new headform impactors

The skull and the cover of the new impactors will be manufactured with the assistance of the *Faculty of Mechanical Engineering - Department of Machining, Process Planning and Metrology*. The technology used is supposed to be turning on the *Okuma L200 MY* lathe machine and milling on the *Okuma MU400 II* milling machine.

The material for the production of both parts is aluminium *EN AW-7075* [68], chosen for its excellent mechanical properties, machining ability and corrosion resistance. According to the preliminary estimation, the cost of manufacturing the skull will be approximately 9 600 *Kč* (350 €) and the cover will be 6 200 *Kč* (225 €), both prices include the cost of material and machining time.

Because the parts are supplied to the manufacturer as CAD files, it is possible to design a machining path via the state of the art CAM software. It is thus not required to supply manufacturing drawings because the features of the model are saved in the CAD files.

At the moment (beginning of May 2020), it is not possible to present the outputs from the manufacturing, because the start of production is planned for the end of May 2020.

Conclusion

Passive safety of passenger's cars is a term that has long been discussed among the automotive engineers. Thanks to the latest technologies, ingenious design and a number of assistants, we can say that the pedestrian protection is already at a very advanced level. However, the technical progress in this field has not yet reached such a degree that we could claim that injuries suffered by the pedestrian within the urban collision will not be fatal. It is therefore necessary to continue with the research and development regarding the pedestrian protection.

The first part of this master's Thesis is focused on a presentation of the tested areas related to pedestrian protection, the assessment criteria and the execution of the tests, in order to familiarize the reader with the topic. Unfortunately, due to the development of the European legislation and the Global technical regulations, the performance of the tests together with the criteria will be updated in 2022. Even though the basic principles will remain the same, it is necessary to keep up with the contemporary legislation and to follow the latest news in a field of pedestrian protection.

In the next chapter, the sensitivity analysis of the selected parameters of the headform impactor's FEM model was performed to investigate the cause behind the varying outputs from real experiments. The results show that the damping coefficient and the coefficient of static friction have the largest influence on the resultant acceleration. This analysis is intended as fundamental for future research of the FEM simulation regarding the testing with the headform impactors. Because we are not interested in the behaviour of the vehicle bonnet but rather in the performance of the headform impactors themselves, a special testing device substituting the real vehicle bonnets was presented. The original design of the device's structure was optimised using FEM simulations while preserving the same mechanical response in tests. This device was manufactured at the beginning of 2020 and afterwards was prepared to perform the first set of experiments. Unfortunately, due to the 2020 COVID-19 outbreak, activities with the testing device have decreased and, at the moment, it is expected that the experiments could take place in the summer of 2020.

The last chapter concerns the modernisation of the existing pedestrian protection throwing device located in the Juliska laboratory. The device was not in a functional condition and its equipment was obsolete. Therefore, it was necessary to tackle these functionality issues by manufacturing new parts and subsequently selecting the appropriate sensors for the measured data acquisition. One of the vital pieces of equipment that was necessary to obtain were new headform impactors. To save costs, these impactors were not purchased by an external supplier but were instead designed from scratch and manufactured with our own resources in July of 2020. Although the renovation of the throwing device required a great effort, it has still not been completed as of June of 2020. It is expected that a standard operation of this device will begin in the summer of 2020.

The main benefit of this master's Thesis lies in the establishment of the basics for future research of the headform impactor's behaviour and in manufacturing of the optimised testing device substituting the real vehicle bonnets. Furthermore, the Juliska laboratory will be equipped with a functional pedestrian protection throwing device, with a new set of in-house-made headform impactors.

Literature Review

[1] Mary Ward 1827-1869. *Offaly Historical & Archaelogical Society* [online]. Tullamore: Co. Offaly, 2014 [Accessed 2018-05-09]. Available from: web.archive.org/web/20140116122125/http://www.offalyhistory.com/reading-resources/history/famous-offaly-people/mary-ward-1827-1869

[2] SPARKE, L. MANAGER, ADVANCED ENGINEERING. *VEHICLE SAFETY PAST, PRESENT AND FUTURE*. Holden, 1999. Available from: https://web.archive.org/web/20071008232829/http://www.aesvn.org/resources/new-car-safety.pdf

[3] *Addendum 126: Regulation No. 127: Concerning the Adoption of Harmonized Technical United Nations Regulations for Wheeled Vehicles, Equipment and Parts which can be Fitted and/or be Used on Wheeled Vehicles and the Conditions for Reciprocal Recognition of Approvals Granted on the Basis of these United Nations Regulations*. Revision 3. Geneva: UN Economic Commission for Europe, 2017.

[4] VAŠÍČEK, Michal. CTU IN PRAGUE. *Pedestrian Protection*. Prague, 2017. Available from: Studium - studying materials at Faculty of Mechanical Engineering CTU in Prague

[5] STRAKA, Jan and Jana FABIÁNOVÁ. *Ročenka nehodovosti: na pozemních komunikacích za rok 2018*. Praha, 2019. Available from: https://www.policie.cz/soubor/rocenka-nehodovosti-2018-pdf.aspx

[6] BESIP - MINISTERSTVO DOPRAVY. *Chodci: Dílčí cíl Národní strategie bezpečosti silničního provozu 2011-2020*. Praha 1, 2019. Available from: https://www.ibesip.cz/getattachment/c69c824c-f418-48bf-977f-16ce00384fe1/Chodci.pdf

[7] INTERNATIONAL TRANSPORT FORUM. *Road Safety Annual Report 2019: Czech Republic*. Paris, 2019. Available from: https://www.itf-oecd.org/sites/default/files/czech-republic-road-safety.pdf

[8] MINISTERSTVO DOPRAVY. *Národní strategie bezpečnosti silničního provozu 2011-2020: Národní strategie bezpečnosti silničního provozu 2011-2020 Informace o plnění vroce 2018*. Praha 1, 2019. Available from: https://www.ibesip.cz/getattachment/Pro-odborniky/Narodni-strategie-BESIP/Plneni-strategie/NSBSP-2018-Informace-o-plneni.pdf

[9] Road safety: European Commission sets out next steps towards “Vision Zero” including key performance indicators | Mobility and Transport. *Mobility and Transport* | [online]. Brussel: European Commission, 2020 [Accessed 2020-06-17]. Available from: https://ec.europa.eu/transport/themes/strategies/news/2019-06-19-vision-zero_en

[10] EUROPEAN TRANSPORT SAFETY COUNCIL. *Ranking EU Progress on Road Safety: 13th Road Safety Performance Index Report*. Brussels, 2019. Available from: https://etsc.eu/wp-content/uploads/AR_2019-Final.pdf

[11] Pedestrians: Traffic Safety Basic Facts 2018. In: *European Commission* [online]. Brussels: European Commission, 2018 [Accessed 2020-03-22]. Available from: https://ec.europa.eu/transport/road_safety/sites/roadsafety/files/pdf/statistics/dacota/bfs20xx_pedestrians.pdf

[12] COOKSON, R, D RICHARDS and R CUERDEN. The characteristics of pedestrian road traffic accidents and the resulting injuries. In: *TRL Insight Report: INS009* [online]. Wokingham, Berkshire: IHS, 2011, s. 1-60 [Accessed 2020-03-22]. ISBN 978-1-84608-908-4. Available from: https://trl.co.uk/sites/default/files/INS009.pdf

[13] *COMMISSION REGULATION (EC) No 631/2009of 22 July 2009: laying down detailed rules for the implementation of Annex I to Regulation (EC) No 78/2009 of the European Parliament and of the Council on the type-approval of motor vehicles with regard to the protection of pedestrians and other vulnerable road users, amending Directive 2007/46/EC and repealing Directives 2003/102/EC and 2005/66/EC*. Brussels: European Commission, 2009. Available from: https://eur-lex.europa.eu/legal-content/GA/TXT/?uri=CELEX:32009R0631

[14] *REGULATION (EC) No 78/2009 OF THE EUROPEAN PARLIAMENT AND OF THE COUNCIL of 14 January 2009: on the type-approval of motor vehicles with regard to the protection of pedestrians and other vulnerable road users, amending Directive 2007/46/EC and repealing Directives 2003/102/EC and 2005/66/EC*. Strasbourg: European Parliament, Council of the European Union, 2009. Available from: https://eur-lex.europa.eu/legal-content/EN/TXT/?qid=1592400598881&uri=CELEX:32009R0078

[15] TNO CRASH-SAFETY RESEARCH CENTRE. *EEVC Working Group 17 Report IMPROVED TEST METHODS TO EVALUATE PEDESTRIAN PROTECTION AFFORDED BY PASSENGER CARS*. Delft, Netherlands, 2003. Available from: https://www.google.com/url?sa=t&rct=j&q=&esrc=s&source=web&cd=1&ved=2ahUKEwjKjovns67oAhWJzKQKHfzQDSUQFjAAegQIAhAB&url=https%3A%2F%2Fwiki.unece.org%2Fdownload%2Fattachments%2F4064195%2FGTR9-4-06e.pdf%3Fapi%3Dv2&usg=AOvVaw1Acp_Y2iE5k57qb5ybcsV5

[16] EPPINGER, Rolf, Emily SUN, Faris BANDAK, Mark HAFFNER, Nopporn KHAEWPONG and Matt MALTESE. NATIONAL HIGHWAY TRAFFIC SAFETY ADMINISTRATION. *Development of Improved Injury Criteria for the Assessment of Advanced Automotive Restraint Systems - II*. Washington, DC, 1999. Available from: https://www.nhtsa.gov/sites/nhtsa.dot.gov/files/rev_criteria_0.pdf

[17] MACLAUGHLIN, Thomas, John WIECHEL and Dennis GUENTHER. S.E.A. INC. *Head Impact Reconstruction - HIC Validation and Pedestrian Injury Risk: SAE Technical paper series 930895*. Detroit, Michigan, 1993. Available from: https://saemobilus.sae.org/content/930895/

[18] HAYES, Wilson, Mark ERICKSON and Erik POWER. Forensic Injury Biomechanics. *Annual review of biomedical engineering*. 2007, 9, 55-86. DOI: 10.1146/annurev.bioeng.9.060906.151946.

[19] GAO, Dalong and Charles WAMPLER. Head injury criterion. *Robotics & Automation Magazine, IEEE*. 2010, 16, 71-74. DOI: 10.1109/MRA.2009.934824.

[20] *Advances in Applied Mechanics: Chapter Two - Neuromechanics: From Neurons to Brain*. Elsevier, 2015, , 266 pages. ISSN 0065-2156. Available from: https://www.sciencedirect.com/science/article/pii/S0065215615000034

[21] EEVC: General info & FAQ. *European Enhanced Vehicle-Safety Committee* [online]. European Enhanced Vehicle-Safety Committee [Accessed 2020-03-23]. Available from: http://www.eevc.org/?site=2

[22] *Regulation (EU) 2019/2144 of the European Parliament and of the Council of 27 November 2019: on type-approval requirements for motor vehicles and their trailers, and systems, components and separate technical units intended for such vehicles, as regards their general safety and the protection of vehicle occupants and vulnerable road users, amending Regulation (EU) 2018/858 of the European Parliament and of the Council and repealing Regulations (EC) No 78/2009, (EC) No 79/2009 and (EC) No 661/2009 of the European Parliament and of the Council and Commission Regulations (EC) No 631/2009...* Brussels: European Commission, 2019. Available from: https://eur-lex.europa.eu/legal-content/EN/TXT/?qid=1592400626252&uri=CELEX:32019R2144

[23] *ISO 6487:2015: Road vehicles — Measurement techniques in impact tests — Instrumentation*. 6. Geneva: International Organization for Standardization, 2015.

[24] *SAE J211/1_201403: Instrumentation for Impact Test - Part 1 - Electronic Instrumentation*. 4. Warrendale, PA: SAE International, 2014.

[25] *LS-DYNA® KEYWORD USER'S MANUAL: Volume I*. LS-DYNA R11. Livermore, California: LIVERMORE SOFTWARE TECHNOLOGY CORPORATION, 2018. Available from: https://www.dynasupport.com/manuals/ls-dyna-manuals/ls-dyna_manual_volume_i_r11.pdf/view

[26] NAVE, Rod. Elasticity, Elastic Properties: Bulk Elastic Properties. *HyperPhysics Concepts* [online]. Atlanta, Goergia: Georgia State University, 2016 [Accessed 2020-03-21]. Available from: http://hyperphysics.phy-astr.gsu.edu/hbase/permot3.html

[27] Convert Elastic Modulus Constants (Shear, Young's, Bulk) – My DataBook. *My DataBook* [online]. 2020 [Accessed 2020-03-22]. Available from: http://www.mydatabook.org/solid-mechanics/convert-elastic-modulus-constants-shear-youngs-bulk/

[28] BIRON, Michel. *Material Selection for Thermoplastic Parts: Chapter: 7 Mechanical Properties*. Kidlington, Oxford: William Andrew is an imprint of Elsevier, 2016. ISBN ISBN: 978-0-7020-6284-1.

[29] Overview of materials for Silicone Rubber. *MatWeb Material Property Data* [online]. Blacksburg, VA: MatWeb, LLC, 2020 [Accessed 2020-03-22]. Available from:http://www.matweb.com/search/DataSheet.aspx?MatGUID=cbe7a469897a47eda563816c86a73520&ckck=1

[30] Properties: Silicone Rubber. *AZo Materials* [online]. Manchester, UK: AZoNetwork UK Ltd., 2020 [Accessed 2020-03-22]. Available from: https://www.azom.com/properties.aspx?ArticleID=920

[31] What is the Damping Coefficient of Materials?. *Sorbothane | Innovating Shock and Vibration Solutions* [online]. Kent, OH: Sorbothane, Incorporated, 2020 [Accessed 2020-03-21]. Available from: https://www.sorbothane.com/what-is-the-damping-coefficient-of-materials.aspx

[32] JIMIN, He and Fu ZHI-FANG. *Modal Analysis: Chapter: 6 Modal analysis of a damped MDoF system*. Oxford: Butterworth-Heinemann, 2001. ISBN 978-0-7506-5079-3.

[33] DELADI, Elena. *STATIC FRICTION IN RUBBER-METAL CONTACTS WITH APPLICATION TO RUBBER PAD FORMING PROCESSES*. Enschede, 2006. ISBN 90-77172-22-X.. DISSERTATION. University of Twente. Vedoucí práce Prof. dr. ir. D.J. Schipper.

[34] PERSSON, B. and A. VOLOKITIN. *Theory of rubber friction: Nonstationary sliding*. Jülich, Germany, 2002. Available from: http://juser.fz-juelich.de/record/25870/files/17249.pdf

[35] *LS-DYNA®Theory Manual*. 07/24/19 (r:11261). Livermore, California 9: LIVERMORE SOFTWARE TECHNOLOGY CORPORATION, 2019. Available from: http://ftp.lstc.com/anonymous/outgoing/jday/manuals/DRAFT_Theory.pdf

[36] Contact modeling in LS-DYNA. *LS-DYNA Support* [online]. Stuttgart: DYNAmore GmbH, 2020 [Accessed 2020-03-24]. Available from: https://www.dynasupport.com/tutorial/ls-dyna-users-guide/contact-modeling-in-ls-dyna

[37] LEINVEBER, Jiří and Pavel VÁVRA. *Strojnické tabulky: učebnice pro školy technického zaměření*. Šesté vydání. Úvaly: Albra, 2017. ISBN 978-80-7361-111-8.

[38] Thread Geometry - Metric Coarse. *TR Fastenings* [online]. Trifast plc, 2020 [Accessed 2020-03-25]. Available from: https://www.trfastenings.com/products/knowledgebase/thread-geometry/metric-coarse-standard

[39] ŠVEC, Vladimír. *Části a mechanismy strojů: spoje a části spojovací*. Vyd. 3. V Praze: České vysoké učení technické, 2008. ISBN 978-80-01-04138-3.

[40] MORTENSEN, Jacob. *Friction Analysis of Bolts*. Esbjerg, 2014.. Bachelor project. Aalborg Universitet Esbjerg. Supervior Anders Schmidt Kristensen.

[41] APETAUR, Milan and Petr ŠIMON. CZECH TECHNICAL UNIVERSITY IN PRAGUE. *Basic Mechanics of Car-Body Design*. Prague, 2010.

[42] *DIN EN 10346: Continously hot-dip coated steel flat products - Technical delivery conditions*. Brussels: European Committee for Standardization, 2009.

[43] EN AW-5042: Mechanical Properties. *Total Materia: The world's most comprehensive materials database* [online]. Zürich: Key to Metals AG, 2020 [Accessed 2020-04-15]. Available from: https://search.totalmateria.com/MaterialDetails/MaterialDetail?vkKey=3234184&keyNum=584&type=3&hs=0

[44] MICHALEC, Jiří. *Pružnost a pevnost I.* 3. vyd. V Praze: České vysoké učení technické, 2009. ISBN 978-80-01-04224-3.

[45] Euro NCAP Pedestrian Testing Protocol. In: *Euro NCAP | The European New Car Assessment Programme* [online]. Version 8.5. Leuven: Euro NCAP, 2019 [Accessed 2020-04-24]. Available from: https://www.euroncap.com/en/for-engineers/protocols/pedestrian-protection/

[46] ZEJDA, Jiří. *Návrh zařízení na testování přední části automobilu pomocí impaktoru dle metodiky EEVC WG 17*. Praha, 2004.. Master's Thesis. České vysoké učení technické v Praze.

[47] RYŠKA, Jakub. *Konfigurace zkoušky nárazu hlavovým impaktorem dle EuroNCAP*. V Praze, 2018.. Bachelor's thesis. České vysoké učení technické v Praze. Supervisor Michal Vašíček.

[48] FESTO AG & CO. KG. *Short-stroke cylinders ADVC/AEVC*. Available from: https://www.festo.com/media/pim/748/D15000100121748.PDF

[49] FESTO AG & CO. KG. *Solenoid Valves CPE, Compact Performance*. Available from: https://www.festo.com/net/SupportPortal/Files/10183/CPE_VU_ENUS.pdf

[50] ČIŽMÁROVÁ, Elena and Jana SOBOTOVÁ. *Nauka o materiálu I. a II.: cvičení*. V Praze: České vysoké učení technické, 2014. ISBN 978-80-01-05550-2.

[51] SELOS. *Holding solenoids with permanent magnet*. Trenčín. Available from: https://www.magnety.cz/pridrzne-elektromagnety/pridrzne-elektromagnety-s-permanentnim-magnetem/

[52] Functionality and technology of optical distance sensors. *Baumer - Passion for sensors* [online]. Frauenfeld: Baumer, 2020 [Accessed 2020-05-10]. Available from: https://www.baumer.com/ch/en/service-support/know-how/function-principle/functionality-and-technology-of-optical-distance-sensors/a/Know-how_Function_optical-distance-sensors

[53] OADM 13I7480/S35A | Distance sensors | Baumer. *Baumer - Passion for sensors* [online]. Frauenfeld: Baumer, 2020 [Accessed 2020-05-10]. Available from: https://www.baumer.com/ch/en/product-overview/distance-measurement/laser-distance-sensors-/miniaturized-laser-sensors/long-range-/oadm-13i7480-s35a/p/26232

[54] LE250UQ | LE Series 1 m Range Laser Displacement Sensor. *Banner Engineering* [online]. Minneapolis: Banner Engineering Corp., 2020 [Accessed 2020-05-10]. Available from: https://www.bannerengineering.com/my/en/products/part.91689.html

[55] INCLINOMETER IN360A. *Hohner Automáticos | Incremental & Absolute Encoders* [online]. Breda: Hohner Automáticos S.L., 2020 [Accessed 2020-05-10]. Available from: https://www.encoderhohner.com/product/in360a/

[56] Laserový modul bod Pictronic, 70104127, 0,4 mW | Conrad.cz. *Conrad Electronic - velkoobchod s moderní elektronikou a technikou* [online]. Praha 3: Conrad Electronic Česká republika, s.r.o., 2020 [Accessed 2020-05-10]. Available from: https://velkoobchod.conrad.cz/laserovy-modul-bod-picotronic-70104127-0-4-mw.k817668

[57] TE CONNECTIVITY COMPANY. *Model EGCS3-D Triaxial accelerometer*. 2017. Available from: https://www.te.com/commerce/DocumentDelivery/DDEController?Action=srchrtrv&DocNm=EGCS3_D_Accelerometer&DocType=Data+Sheet&DocLang=English&DocFormat=pdf&PartCntxt=CAT-PPA0066

[58] Anthropomorphy Dummy Accelerometer | 64x Series | TE Connectivity. *Te Connectivity: Connectors & Sensors for Harsh Enviroments* [online]. TE Connectivity, 2020 [Accessed 2020-05-11]. Available from: https://www.te.com/usa-en/product-CAT-PPA0118.html

[59] EURO NCAP. *Technical Bulletin: Damped Accelerometers in Pedestrian Protection Testing*. Version 2.1. 2018. Available from: https://cdn.euroncap.com/media/41784/tb-003-damped-accelerometers-v21.201811141155467810.pdf

[60] *Universal Impact simulation test system: FMVSS 201 - 266, GTR 9 | EEVC WG17 | ECE R12 - R21*. Les Boutries, 2014. Available from: http://bia.fr/upload/site/pdf/PDF2014/BIA_Impact_A4.pdf

[61] ROZUMNYI, Denys. *All-speed Long-term Tracker Exploiting Blur*. Prague 6: Center for Machine Perception, Department of Cybernetics Faculty of Electrical Engineering, Czech Technical University, 2019. ISSN 1213-2365.. Master's Thesis. CTU in Prague. Supervisor Jiří Matas.

[62] CDAQ-9174 - National Instruments. *Automated Test and Automated Measurement Systems - National Instruments* [online]. National Instruments, 2020 [Accessed 2020-05-12]. Available from: https://www.ni.com/en-gb/support/model.cdaq-9174.html

[63] NI-9237 - National Instruments. *Automated Test and Automated Measurement Systems - National Instruments* [online]. National Instruments, 2020 [Accessed 2020-06-10]. Available from: https://www.ni.com/en-gb/support/model.ni-9237.html

[64] NI-9205 - National Instruments. In: *Automated Test and Automated Measurement Systems - National Instruments* [online]. National Instruments, 2020 [Accessed 2020-05-12]. Available from: https://www.ni.com/en-gb/support/model.ni-9205.html

[65] NI-9472 - National Instruments. *Automated Test and Automated Measurement Systems - National Instruments* [online]. National Instruments, 2020 [Accessed 2020-06-19]. Available from: https://www.ni.com/cs-cz/support/model.ni-9472.html

[66] Original Prusa i3 MK3S kit. *Original Prusa 3D printers directly from Josef Prusa - Prusa Research* [online]. Praha: Prusa Research a.s., 2020 [Accessed 2020-06-15]. Available from: https://shop.prusa3d.com/en/3d-printers/180-original-prusa-i3-mk3s-kit.html#

[67] Introduction to FDM 3D printing | 3D Hubs. *3D Hubs | On-demand Manufacturing: Quotes in Seconds, Parts in Days* [online]. 3D HUBS B.V., 2020 [Accessed 2020-06-15]. Available from: https://www.3dhubs.com/knowledge-base/introduction-fdm-3d-printing/#what

[68] LEICHTMETALL. *Features of EN AW-7075: Product data sheet AA7075, EN AW-7075, EN AW-AlZn5,5MgCu*. Hannover. Available from: https://www.leichtmetall.eu/site/assets/files/datenblatt/7075_Produktdatenblatt_A4-en_us-c.pdf

[69] LAWRENCE, Graham. TRL LIMITED. *THE NEXT STEPS FOR PEDESTRIAN PROTECTION TEST METHODS*. United Kingdom, 2005. Available from: https://www.google.com/url?sa=t&rct=j&q=&esrc=s&source=web&cd=1&ved=2ahUKEwiglMrWsa7oAhXNGewKHZDfDXwQFjAAegQIBRAB&url=http%3A%2F%2Fwww.eevc.net%2Ffileuploads%2Fserver%2Fphp%2F%3Ffile%3DESV2005_WG17_05-0379-O.pdf%26download%3D1&usg=AOvVaw2C7jz1_FJ4MroTflyz5cx7

[70] PTAK, Mariusz. Pedestrian safety: A new method to assess pedestrian kinematics: A new method to assess pedestrian kinematics. *Transport*. 2019, **34**, 41-51. DOI: 10.3846/transport.2019.7081.

[71] SEARSON, Dj a Robert ANDERSON. *Implications of easing head impact criteria in pedestrian crash standards*. 2010.

[72] ZANDER, Oliver. BUNDESANSTALT FÜR STRAßENWESEN. *Flex-GTR: Open questions and proposals forACL, PCL and MCL injury thresholds: 7th Meeting of the GRSP Flex PLI Technical Evaluation Group*. Bergisch Gladbach, 2008. Available from: https://www.unece.org/fileadmin/DAM/trans/doc/2009/wp29grsp/teg-078e.pdf

[73] CICHOS, D., D. DE VOGEL, M. OTTO, O. SCHAAR and S. ZÖLSCH. ARBEITSKREIS MESSDATENVERARBEITUNG FAHRZEUGSICHERHEIT. *Crash Analysis: Criteria Description*. Version 1.6.1. Bergisch Gladbach, 2004. Available from: http://web2.uwindsor.ca/courses/engineering/altenhof/92544/crash_functions_descriptions.pdf

[74] SCHMITT, PD and Dr. MUSER. AGU ZÜRICH. *Study on Safer Motor Vehicles for Cyclists in the context of the EU Pedestrian Protection Regulations*. Zurich, 2016. Available from: https://ecf.com/sites/ecf.com/files/ECF_AGU%20ZURICH%20final%20report%20on%20passive%20safety.pdf

[75] UN ECONOMIC COMMISSION FOR EUROPE. *Proposal of amendments to gtr 9 (Pedestrian safety) ECE/TRANS/180/Add.9, Add.9/Corr.1 & 2 and Amend.1: Test area and Measuring point*. Geneva, 2011. Available from: https://www.unece.org/fileadmin/DAM/trans/doc/2011/wp29grsp/GRSP-49-09e.pdf

List of Figures

List of Tables

List of Annexes

Annex I

Verze	Poznámka	Proměnná
V00_00_0000	Původní verze	

Změna parametrů elemet	Sloupec1	ELFORM	KM	MU	MACC [m/s2]	MACC [g]	HIC [-]	HG [J]	ET [s]	ET [min]	Rozdíl MACC	Rozdíl HIC
V00_00_0001	ELFORM 0	0	2.5	0.1	2703	275.63	1068.32	7.561	90	01:30	7.99%	33.96%
V00_00_0002	ELFORM -2	-2	2.5	0.1	2505	255.44	795.629	0	484	08:04	0.08%	-0.23%
V00_00_0003	ELFORM -1	-1	2.5	0.1	2503	255.23	797.489	0	366	06:06	0.00%	0.00%
										MAX	7.99%	33.96%

Změna KM [GPa]		ELFORM	KM [GPa]	MU	MACC [m/s2]	MACC [g]	HIC [-]	HG [J]	ET [s]	ET [min]	Rozdíl MACC	Rozdíl HIC
V00_01_0007		-1	1.8	0.1	2553	260.33	848.105	0	314	05:14	2.00%	6.35%
V00_01_0006		-1	1.9	0.1	2540	259.01	836.199	0	321	05:21	1.48%	4.88%
V00_01_0005		-1	2	0.1	2535	258.50	822.103	0	330	05:30	1.28%	3.09%
V00_01_0004		-1	2.1	0.1	2524	257.38	816.2	0	336	05:36	0.84%	2.35%
V00_01_0003		-1	2.2	0.1	2518	256.76	812.6799	0	343	05:43	0.60%	1.90%
V00_01_0002		-1	2.3	0.1	2512	256.15	804.767	0	359	05:59	0.36%	0.91%
V00_01_0001		-1	2.4	0.1	2505	255.44	796.894	0	359	05:59	0.08%	-0.07%
V00_01_0008	standard	-1	2.5	0.1	2503	255.23	797.489	0	366	06:06	0.00%	0.00%
V00_01_0009		-1	2.6	0.1	2498	254.73	797.489	0	376	06:16	-0.20%	0.00%
V00_01_0010		-1	2.7	0.1	2490	253.91	780.995	0	382	06:22	-0.52%	-2.07%
V00_01_0011		-1	2.8	0.1	2484	253.30	782.794	0	391	06:31	-0.76%	-1.84%
V00_01_0012		-1	2.9	0.1	2483	253.20	773.284	0	395	06:35	-0.80%	-3.04%
V00_01_0013		-1	3	0.1	2474	252.28	767.693	0	400	06:40	-1.16%	-3.74%
V00_01_0014		-1	3.1	0.1	2474	252.28	763.588	0	408	06:48	-1.16%	-4.25%
V00_01_0015		-1	3.2	0.1	2465	251.36	759.978	0	415	06:55	-1.52%	-4.70%
										MAX:	2.00%	6.35%
										Střední hodnota	255.32	
28%										ABS směrodatná odchylk	2.59	
-28%										REL směrodatná odchylka	1.02%	

Změna MU		ELFORM	KM	MU	MACC [m/s2]	MACC [g]	HIC [-]	HG [J]	ET [s]	ET [min]	Rozdíl MACC	Rozdíl HIC
V00_02_0016		-1	2.5	0.01	2788	284.30	962.905	0	378	06:18	11.39%	20.74%
V00_02_0005		-1	2.5	0.02	2742	279.61	926.861	0	373	06:13	9.55%	16.22%
V00_02_0004		-1	2.5	0.04	2681	273.39	892.08	0	373	06:13	7.11%	11.86%
V00_02_0003		-1	2.5	0.06	2617	266.86	850.822	0	369	06:09	4.55%	6.69%
V00_02_0002		-1	2.5	0.08	2557	260.74	820.351	0	367	06:07	2.16%	2.87%
V00_02_0001	standard	-1	2.5	0.1	2503	255.23	797.489	0	368	06:08	0.00%	0.00%
V00_02_0006		-1	2.5	0.12	2460	250.85	765.383	0	369	06:09	-1.72%	-4.03%
V00_02_0007		-1	2.5	0.14	2410	245.75	742.554	0	372	06:12	-3.72%	-6.89%
V00_02_0008		-1	2.5	0.16	2366	241.26	719.403	0	372	06:12	-5.47%	-9.79%
V00_02_0009		-1	2.5	0.18	2333	237.90	699.78	0	373	06:13	-6.79%	-12.25%
V00_02_0010		-1	2.5	0.2	2292	233.72	681.874	0	372	06:12	-8.43%	-14.50%
V00_02_0011		-1	2.5	0.22	2259	230.35	663.683	0	373	06:13	-9.75%	-16.78%
V00_02_0012		-1	2.5	0.24	2221	226.48	647.255	0	371	06:11	-11.27%	-18.84%
V00_02_0013		-1	2.5	0.26	2192	223.52	632.373	0	371	06:11	-12.43%	-20.70%
V00_02_0014		-1	2.5	0.28	2164	220.67	619.16099	0	371	06:11	-13.54%	-22.36%
V00_02_0015		-1	2.5	0.3	2135	217.71	606.951	0	373	06:13	-14.70%	-23.89%
										MAX:	-14.70%	-23.89%
200%										Střední hodnota	246.77	
-90%										ABS směrodatná odchylk	20.78	
										REL směrodatná odchylka	8.42%	

Změna hustoty		ro_Deckel	ro_Kugel	ro_Haut	MACC [m/s2]	MACC [g]	HIC [-]	HG [J]	ET [s]	ET [min]	Rozdíl MACC	Rozdíl HIC
V00_03_0003		2.930E-06	2.441E-06	1.067E-06	2522	257.17	799.738	0	387	06:27	0.76%	0.28%
V00_03_0001	standard	3.071E-06	2.230E-06	1.186E-06	2503	255.23	797.489	0	372	06:12	0.00%	0.00%
V00_03_0002		3.050E-06	2.142E-06	1.305E-06	2489	253.81	786.611	0	351	05:51	-0.56%	-1.36%
										MAX	0.76%	-1.36%
10%										Střední hodnota	255.40	
-10%										ABS směrodatná odchylk	1.38	
										REL směrodatná odchylka	0.54%	

Změna FS		FS	FD	DC	MACC [m/s2]	MACC [g]	HIC [-]	HG [J]	ET [s]	ET [min]	Rozdíl MACC	Rozdíl HIC
V00_04_0007		0.4	0.7	0.001	2361	240.75	728.175	0	376	06:16	-5.67%	-8.69%
V00_04_0006		0.45	0.7	0.001	2409	245.65	754.743	0	376	06:16	-3.76%	-5.36%
V00_04_0005		0.5	0.7	0.001	2448	249.63	766.1	0	376	06:16	-2.20%	-3.94%
V00_04_0004		0.55	0.7	0.001	2469	251.77	779.301	0	376	06:16	-1.36%	-2.28%
V00_04_0003		0.6	0.7	0.001	2482	253.09	788.313	0	375	06:15	-0.84%	-1.15%
V00_04_0002		0.65	0.7	0.001	2493	254.22	792.285	0	376	06:16	-0.40%	-0.65%
V00_04_0001	standard	0.7	0.7	0.001	2503	255.23	797.489	0	374	06:14	0.00%	0.00%
V00_04_0008		0.75	0.7	0.001	2504	255.34	792.333	0	376	06:16	0.04%	-0.65%
V00_04_0009		0.8	0.7	0.001	2504	255.34	794.449	0	376	06:16	0.04%	-0.38%
V00_04_0010		0.85	0.7	0.001	2503	255.23	793.258	0	376	06:16	0.00%	-0.53%
V00_04_0011		0.9	0.7	0.001	2503	255.23	792.695	0	375	06:15	0.00%	-0.60%
										MAX	-5.67%	-8.69%
28%										Střední hodnota	251.95	
-42%										ABS směrodatná odchylk	4.59	
										REL směrodatná odchylka	1.82%	

Změna FD		FS	FD	DC	MACC [m/s2]	MACC [g]	HIC [-]	HG [J]	ET [s]	ET [min]	Rozdíl MACC	Rozdíl HIC
V00_05_0007		0.7	0.4	0.001	2501	255.03	791.437	0	376	06:16	-0.08%	-0.76%
V00_05_0006		0.7	0.45	0.001	2498	254.73	790.993	0	377	06:17	-0.20%	-0.81%
V00_05_0005		0.7	0.5	0.001	2501	255.03	791.583	0	374	06:14	-0.08%	-0.74%
V00_05_0004		0.7	0.55	0.001	2500	254.93	792.14	0	373	06:13	-0.12%	-0.67%
V00_05_0003		0.7	0.6	0.001	2498	254.73	791.401	0	375	06:15	-0.20%	-0.76%
V00_05_0002		0.7	0.65	0.001	2500	254.93	796.026	0	377	06:17	-0.12%	-0.18%
V00_05_0001	standard	0.7	0.7	0.001	2503	255.23	797.489	0	376	06:16	0.00%	0.00%
V00_05_0008		0.7	0.75	0.001	2501	255.03	791.432	0	376	06:16	-0.08%	-0.76%
V00_05_0009		0.7	0.8	0.001	2498	254.73	791.471	0	376	06:16	-0.20%	-0.75%
V00_05_0010		0.7	0.85	0.001	2497	254.62	791.408	0	377	06:17	-0.24%	-0.76%
V00_05_0011		0.7	0.9	0.001	2498	254.70	791.464	0		MAX	-0.24%	-0.81%
21%										Střední hodnota	254.90	
-42%										ABS směrodatná odchylk	0.18	
										REL směrodatná odchylka	0.07%	

Změna DC		FS	FD	DC	MACC [m/s2]	MACC [g]	HIC [-]	HG [J]	ET [s]	ET [min]	Rozdíl MACC	Rozdíl HIC
V00_06_0002		0.7	0.6	0.0001	2500	254.93	791.013	0	385	06:25	0.08%	0.08%
V00_06_0001	standard	0.7	0.6	0.001	2498	254.73	791.401	0	386	06:26	0.00%	0.00%
V00_06_0003		0.7	0.6	0.01	2501	255.03	790.944	0	405	06:45	0.12%	0.12%
V00_06_0004		0.7	0.6	0.1	2501	255.03	791.364	0	393	06:33	0.12%	0.12%
										MAX	0.12%	0.12%
99%										Střední hodnota	254.93	
-90%										ABS směrodatná odchylk	0.12	
										REL směrodatná odchylka	0.05%	

Změna SOFT		SOFT	SOFSCL	MAXPAR	SBOPT	DEPTH	BSORT	MACC [m/s2]	MACC [g]	HIC [-]	HG [J]	ET [s]	ET [min]	Rozdíl MACC	Rozdíl HIC
V00_07_0001		1						2503	255.234967	797.489	0	365	06:05		
V00_07_0002		2	0.1	1.025	3	5	0		0		0	380	06:20		
V00_07_0003									0				00:00		
V00_07_0004									0				00:00		
													MAX	0.00%	0.00%

Annex I – Table of results of the sensitivity analysis.

Annex II

Version	Pre-stress [Gpa]	Specimen Material	Velocity [km/h]	Number of bolts	Fixing directly to frame	Frame width under trapez	Frame grid modification	Welding specimen and trapz	a_max [g]	HIC15	Comment
V01_00_0000_A_65_32	0	Base Steel SIGY 144 Mpa	32	8	NO	100	OLD	CBAR	-	-	Clean version without calculation
V01_00_0000_A_65_40	0	Base Steel SIGY 144 Mpa	40	8	NO	100	OLD	CBAR	-	-	Clean version without calculation
V01_00_0001_A_65_32_8fach	0	Base Steel SIGY 144 Mpa	32	8	NO	100	OLD	CBAR	155.01	1210.05	Clean version calculated
V01_00_0001_A_65_40_8fach	0	Base Steel SIGY 144 Mpa	40	8	NO	100	OLD	CBAR	195.49	1876.66	Clean version calculated
V01_00_0002_A_65_40_4fach	0	Base Steel SIGY 144 Mpa	40	4	NO	100	OLD	CBAR	181.93	956.09	Clean version calculated
V01_00_0003_A_65_40_pre_stress	0.0324	Base Steel SIGY 144 Mpa	40	8	NO	100	OLD	CBAR	182.64	1902.97	Used pre-stress on the thread rods 0.0324 GPa
V01_00_0004_A_65_40_m1	0	Base Steel SIGY 144 Mpa	40	8	YES	100	OLD	CBAR	196.61	2231.83	First modification, length of the thread rods reduced, positioning the trapez directly to the frame - leaning while deformed - higher HIC
V01_00_0004_A_65_40_m2	0	Base Steel SIGY 144 Mpa	40	8	YES	70	OLD	CBAR	193.96	1928.26	Width of the frame reduced to 70mm to simulate movement of the holes to the inner edge
V01_00_0004_A_65_40_m2_v2	0	Base Steel SIGY 144 Mpa	40	8	YES	70	NEW	CBAR	196.61	1927.89	Modification of the mesh grid of the upper frame after movement the elements.
V01_00_0004_A_65_40_m2_v2_alu	0	ALU SIGY 140 Mpa	40	8	YES	70	NEW	CBAR	164.7	1682.21	Usage of the aluminum material from Mr. Soellner
V01_00_0004_A_65_40_m2_v2_alu_v2	0	ALU SIGY 160 Mpa	40	8	YES	70	NEW	CBAR	167.58	1759.05	Usage of the aluminum material from Mr. Vedral
V01_00_0004_A_65_40_m2_v2_glue	0	Base Steel SIGY 144 Mpa	40	8	YES	70	NEW	Structural GLUE	206.61	1932.74	Realization of the structural adhesive joint between trapez profile and testing plate with preserving the hexa contacts
V01_00_0004_A_65_40_m2_v2_glue2	0	Base Steel SIGY 144 Mpa	40	8	YES	70	NEW	Structural GLUE	201.41	1988.76	Realization of the structural adhesive joint between trapez profile and testing plate without the hexa contacts
V01_00_0006_A_65_40_m3_SPC	0	Base Steel SIGY 144 Mpa	40	8	YES	70	NEW	CBAR	194.88	1883.16	SPC to the all nodes of the bottom surface of the frame
V01_00_0007_A_65_40_hexa	0	Base Steel SIGY 144 Mpa	40	8	NO	100	OLD	DYNA SPOT WELD – Hexacontact	203.14	1874.16	Realization of the spot weld between the trapez profile and testing plate instead of old rigid beam connection
For production the following parameters were set: Positiong the specimen directly to the frame. Usage of eight poit anchoring. Using the prestress of 0.0324 Gpa. Usage of hexa contact.											
The material and trapez profile shape will be discused in the future phase boxtest_v2											

Annex II – Table of modification regarding the old box testing device.

Annex III

Version	Pre-stress [GPa]	Material	Velocity [km/h]	Trapez height [mm]	Specimen thickness [mm]	Friction (Gesamtfahrzeug Contact)	Nullshell bolt + nut	Gesamfahrzeug contact Soft1 A	a_max [g]	HIC15	Comment
V01_00_0001_A_65_40	0	Steel Old– SIGY 144 MPa	40	20	0.8	FS 0.15 FD 0.08	old	old	224.86	1657.13	Original version, placement of the impactor via define_transformation
V01_00_0002_A_65_40	0	Steel Old– SIGY 144 MPa	40	20	0.8	FS 0.15 FD 0.08	old	old	222.42	1744.43	Improvement of previous version
V01_00_0003_A_65_40	0	Steel Old– SIGY 144 MPa	40	20	0.8	FS 0.15 FD 0.08	old	old	221.61	1763.3	Placement of the impactor via pedestrian_safety deck
V01_00_0004_A_65_40	0.0324	Steel Old– SIGY 144 MPa	40	20	0.8	FS 0.15 FD 0.08	old	old	220.27	1673.24	Prestress of 0.0324 GPa with preserving the tied_nodes_to_surface_contact
V01_00_0005_A_65_40	0.0324	Steel Old– SIGY 144 MPa	40	20	0.8	FS 0.15 FD 0.08	old	old	210.08	992.54	Prestress without tied_nodes_to_surface contact
V01_00_0006_A_65_40	0	Steel Old– SIGY 144 MPa	40	20	0.8	FS 0.15 FD 0.08	new	new	211.91	1473	New solid part of bolt and nuts. New setting of gesamfahrzeug contact with using SOFT1 and setting A
V01_00_0007_A_65_40	0.0324	Steel Old– SIGY 144 MPa	40	20	0.8	FS 0.15 FD 0.08	new	new	223.13	**1723.4**	prestress 0.0324 GPa, gesamfahrzeug contact SOFT1 setting A
V01_00_0008_A_65_40	0.1	Steel Old– SIGY 144 MPa	40	20	0.8	FS 0.15 FD 0.08	new	new	224.35	1713.76	prestress 0.1 GPa, gesamfahrzeug contact SOFT1 setting A
V01_00_0009_A_65_35	0.0324	Steel Old– SIGY 144 MPa	35	20	0.8	FS 0.15 FD 0.08	new	new	191.11	1340.98	Lowered impact speed to 35 km/h
V01_00_0010_A_65_40	0.0324	Steel Old– SIGY 144 MPa	40	15	0.8	FS 0.15 FD 0.08	new	new	212.31	1480.38	Modified height of trapez profile, reduction from 20 mm to 14.8 mm
V01_00_0011_A_65_40	0.0324	Steel Karel – SIGY 273 MPa	40	20	0.8	FS 0.15 FD 0.08	new	new	244.13	2398.1	Usage of new material data from Karel, SIGY 273 MPa
V01_00_0012_A_65_40	0.06	Alu Old – SIGY 140 Mpa	40	20	0.8	FS 0.15 FD 0.08	new	new	129.71	1365.32	Usage of old aluminum material from Mr. Soellner (without strain rate) SIGY 140 MPa
V01_00_0012_A_65_40_v2	0.06	Alu New – SIGY 160 Mpa	40	20	0.8	FS 0.15 FD 0.08	new	new	137.22	1403.32	Usage of old aluminum material from Mr. Vedral (without strain rate) SIGY 160 MPa
V01_00_0013_A_65_40	0.0324	Steel Old– SIGY 144 MPa	40	20	0.8	FS 0 FD 0	new	new	210.89	1488.83	Removal of friction from Gesamfahrzeoug for evaluation the influence of friction
V01_00_0014_A_65_40	0.0324	Steel Old– SIGY 144 MPa	40	20	0.8	FS 0.15 FD 0.08	new	new	223.02	1750.79	Nodes of the hole restricted to asset the influence of friction
V01_00_0015_A_65_40	0.0324	Steel Soellner – SIGY 206 MPa	40	20	0.8	FS 0.15 FD 0.08	new	new	228.73	1933.91	New steel material from Mr. Soellner. SIGY 206 MPa
V01_00_0016_A_65_35	0.0324	Steel Soellner – SIGY 206 MPa	35	15	0.8	FS 0.1 FD 0.05	new	new – reduced friction coefficient	186.04	1213.36	Version for lowest possible HIC. Low impact speed, new steel material, lower profile height, lower friction coefficients (simulation of better surface finish)
V01_00_0016_A_65_40_v2	0.0324	Steel Soellner – SIGY 206 MPa	40	15	0.8	FS 0.1 FD 0.05	new	new – reduced friction coefficient	216.92	1553.7	Version for comparison of the velocity influence
V01_00_0017_A_65_40	0.0324	Steel Old– SIGY 144 MPa	40	20	0.8	FS 0.1 FD 0.05	new	new – reduced friction coefficient	223.84	1739.34	Reduced FS and FD for assessment of the friction
V01_00_0018_A_65_40	0.0324	Steel Soellner – SIGY 206 MPa	40	15	0.8	FS 0.15 FD 0.08	new	new	216.58	1652.98	Pre final version
V01_00_0019_A_65_40	0.06	Alu Old – SIGY 140 Mpa	40	20	1.15	FS 0.15 FD 0.08	new	new	184.07	1947.71	New testing plate thickness of 1.15 mm
V01_00_0020_A_65_40	0.0324	Steel Soellner – SIGY 206 MPa	40	15	0.8	FS 0.15 FD 0.08	new	new	216.51	1652.98	Final version sent for production
V01_00_0021_A_65_40	0.0324	Steel Soellner – SIGY 206 MPa	40	15	0.8	FS 0.15 FD 0.08	new	new	227.82	1628.93	Pitch between the spot welds is 20 mm instead of 40 mm

Annex III – Table of modification regarding the new box testing device.

Annex IV

CROSS SECTION GEOMETRICAL RESULTS	
NAME	CROSS_5
ID	5
Area A	111.243
Mass center xs	42.607
Mass center ys	-10.8037
Moment of Inertia for bending Ix	8394.2
Moment of Inertia for bending Iy	131816
Moment of Inertia for bending Ixy	4.63842e-11
Angle of Principal axis alfa	-1.5708
Principal Moment of Inertia for bending I1	131816
Principal Moment of Inertia for bending I2	8394.2
Torsional stiffness parameter It	23.7319
Shear center xm	42.607
Shear center ym	-26.213
Warping coefficient at Mass center Cw(s)	3.29948e+07
Warping coefficient at Shear center Cw(m)	1.69544e+06
Gamma Function (ABAQUS) Gamma	-1.66665e-10
Section module in bending x Wx	776.977
Section module in bending y Wy	2196.93
Section module in bending 1 W1	2196.93
Section module in bending 2 W2	776.977
Section plastic module in bending x Wpx	908.339
Section plastic module in bending y Wpy	3379.89
Section plastic module in bending 1 Wp1	3379.89
Section plastic module in bending 2 Wp2	908.346
Shear area A1	17.9108
Shear area A2	67.9481
Shear area A12	0
Shear area Ax	67.9481
Shear area Ay	17.9108
Hydraulic diameter Dh	1.6

Annex IV – Geometrical characteristic of 20 mm high trapeze profile.

Annex V

CROSS SECTION GEOMETRICAL RESULTS	
NAME	CROSS_2
ID	2
Area A	101.22
Mass center xs	56.4069
Mass center ys	-8.09089
Moment of Inertia for bending Ix	4441.03
Moment of Inertia for bending Iy	106346
Moment of Inertia for bending Ixy	0.168681
Angle of Principal axis alfa	-1.57079
Principal Moment of Inertia for bending I1	106346
Principal Moment of Inertia for bending I2	4441.03
Torsional stiffness parameter It	21.5936
Shear center xm	56.4064
Shear center ym	-19.5898
Warping coefficient at Mass center Cw(s)	1.49431e+07
Warping coefficient at Shear center Cw(m)	881638
Gamma Function (ABAQUS) Gamma	-1.98725e-10
Section module in bending x Wx	548.893
Section module in bending y Wy	1885.33
Section module in bending 1 W1	1885.34
Section module in bending 2 W2	548.887
Section plastic module in bending x Wpx	636.664
Section plastic module in bending y Wpy	2885.4
Section plastic module in bending 1 Wp1	2885.4
Section plastic module in bending 2 Wp2	636.672
Shear area A1	11.6537
Shear area A2	66.2323
Shear area A12	0
Shear area Ax	66.2323
Shear area Ay	11.6537
Hydraulic diameter Dh	1.6

Annex V – Geometrical characteristic of 15 mm high trapeze profile.

Annex VI

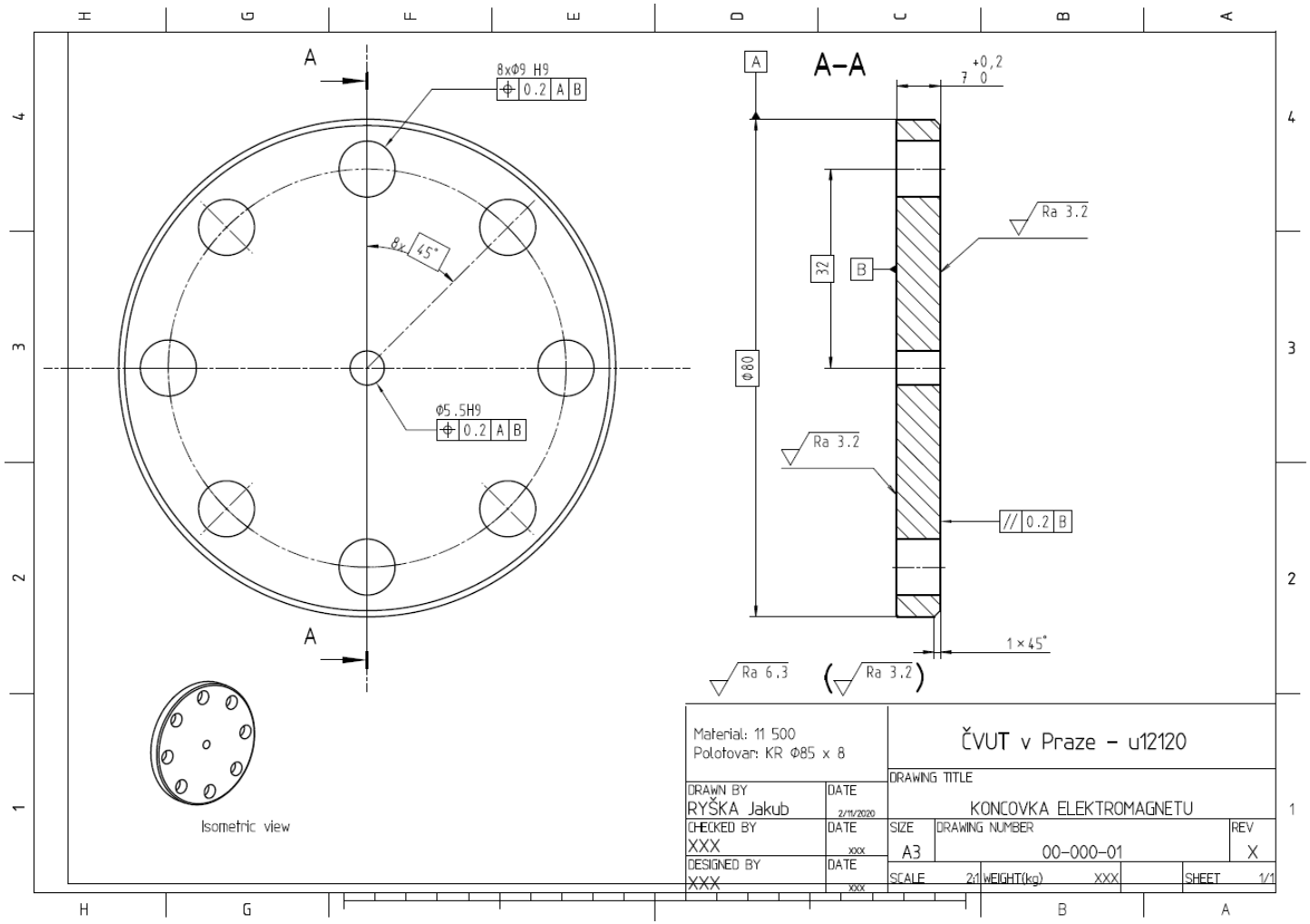

Annex VI – Drawing of the new adapter for impactors.

Annex VII

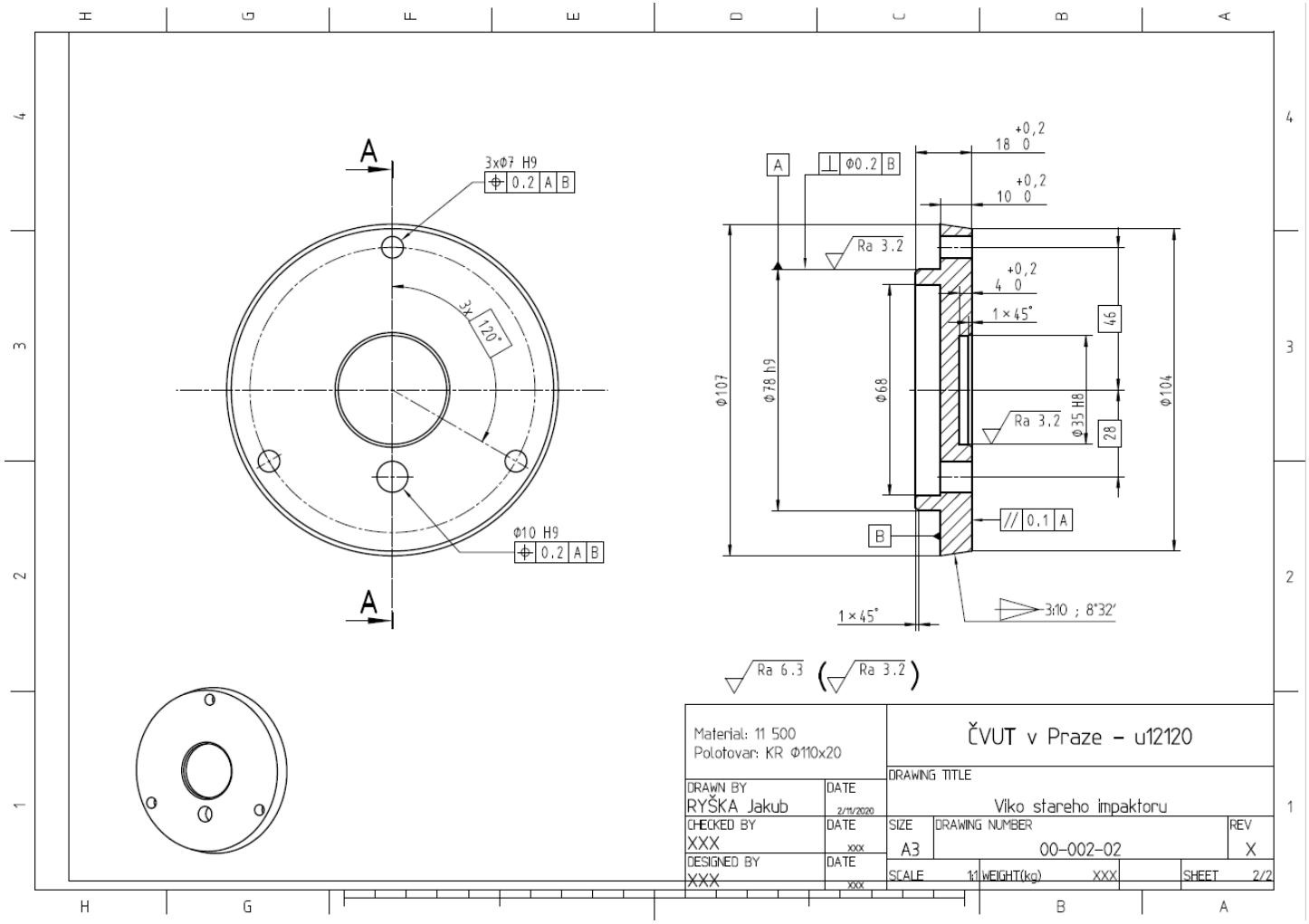

Annex VII – Drawing of the new cover for the old adult headform impactor.

Annex VIII

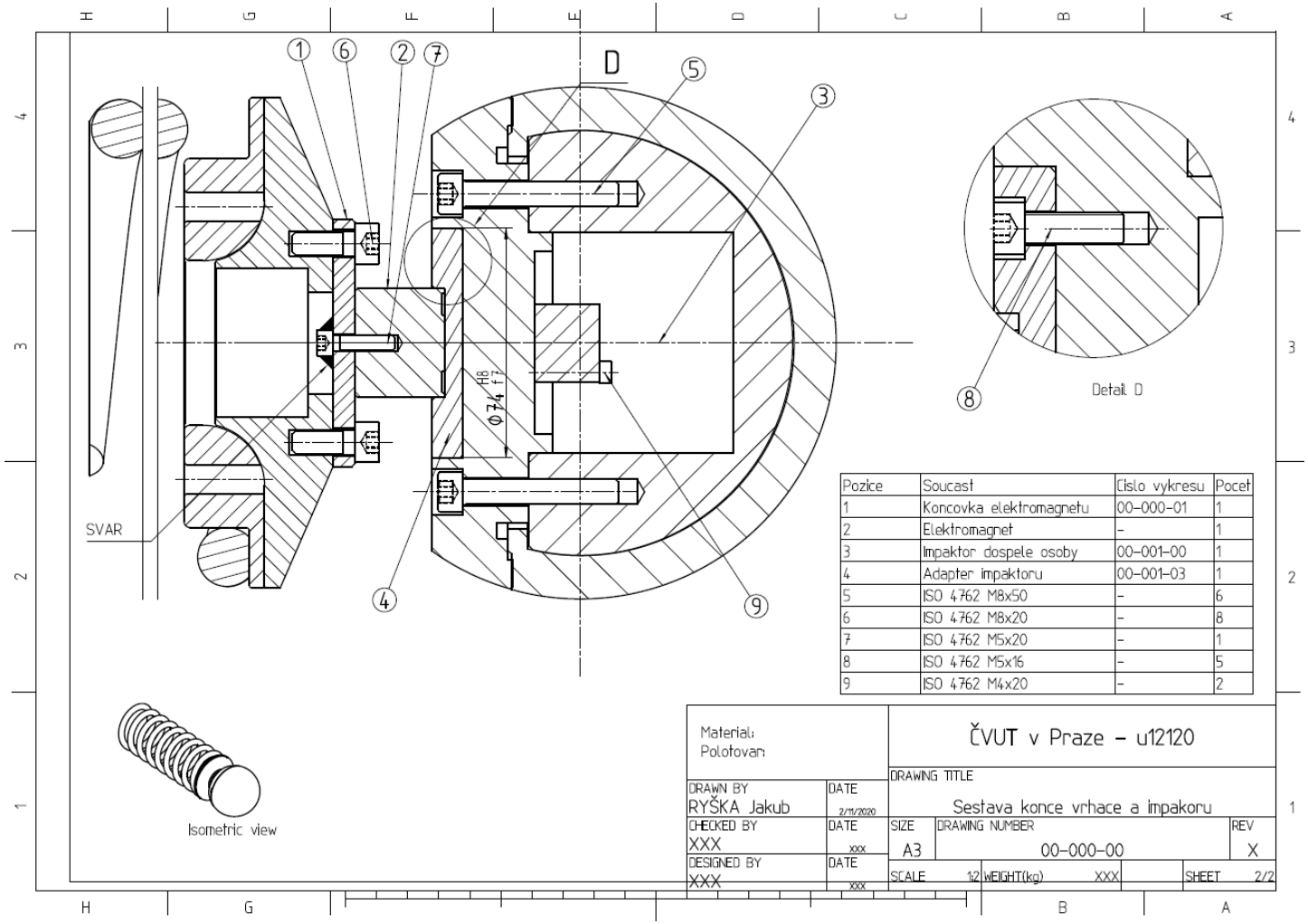

Pozice	Soucast	Cislo vykresu	Pocet
1	Koncovka elektromagnetu	00-000-01	1
2	Elektromagnet	-	1
3	Impaktor dospele osoby	00-001-00	1
4	Adapter impaktoru	00-001-03	1
5	ISO 4762 M8x50	-	6
6	ISO 4762 M8x20	-	8
7	ISO 4762 M5x20	-	1
8	ISO 4762 M5x16	-	5
9	ISO 4762 M4x20	-	2

Material:
Polotovar:

ČVUT v Praze - u12120

DRAWING TITLE: Sestava konce vrhace a impakoru

DRAWN BY: RYŠKA Jakub	DATE: 2/11/2020		
CHECKED BY: XXX	DATE: XXX	SIZE: A3	DRAWING NUMBER: 00-000-00 REV: X
DESIGNED BY: XXX	DATE: XXX	SCALE: 1:2	WEIGHT(kg): XXX SHEET: 2/2

Annex VIII – Assembly of the new headform impactor connected via an electromagnetic system using a new impactor's adapter.

Annex IX

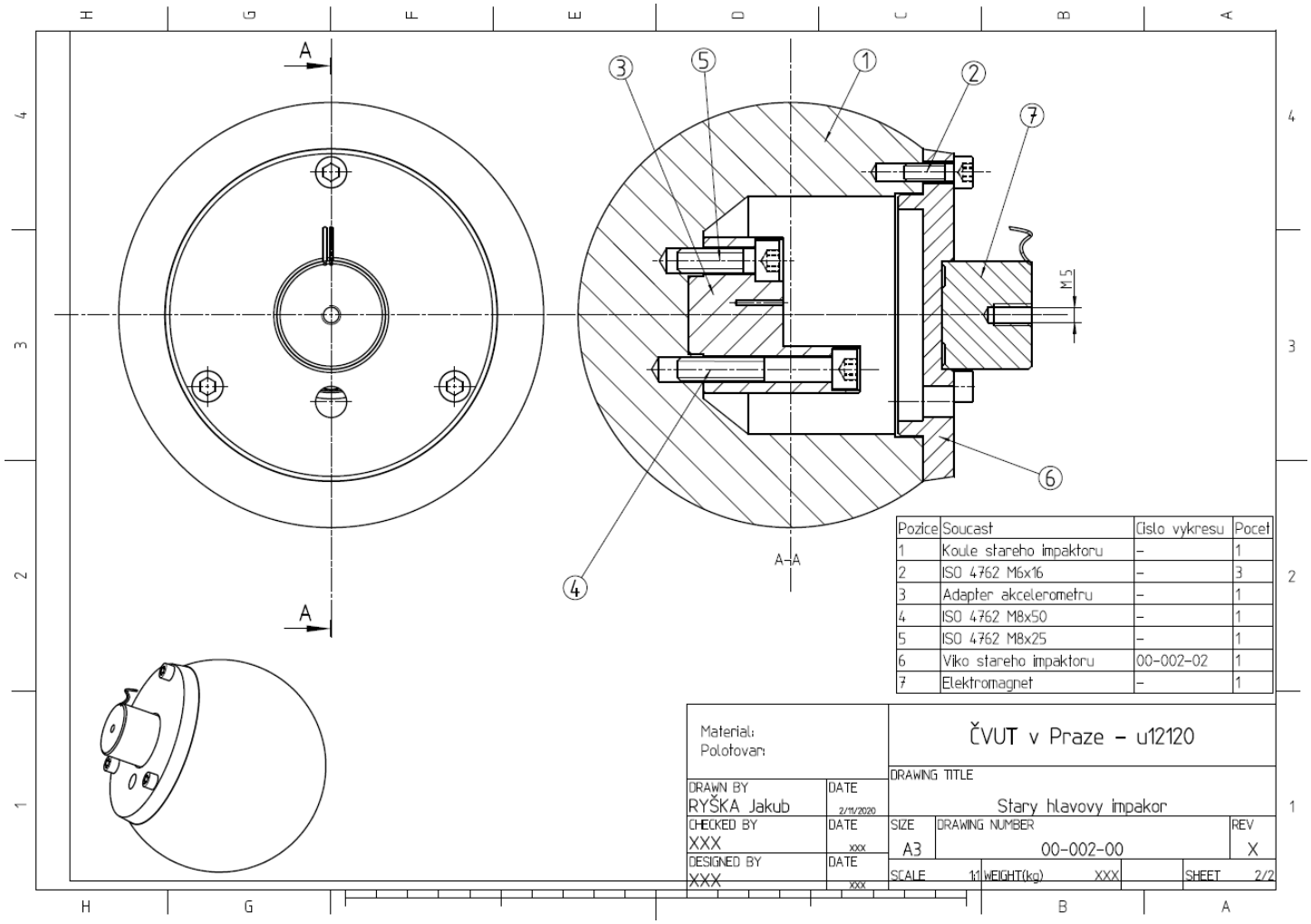

Annex IX – Assembly of the old headform impactor with a new cover suitable for electromagnet.

Annex X

Annex X – Manufactured new impactor's adapter.

Annex XI

Annex XI – Manufactured new cover for the old headform impactor.

Annex XII

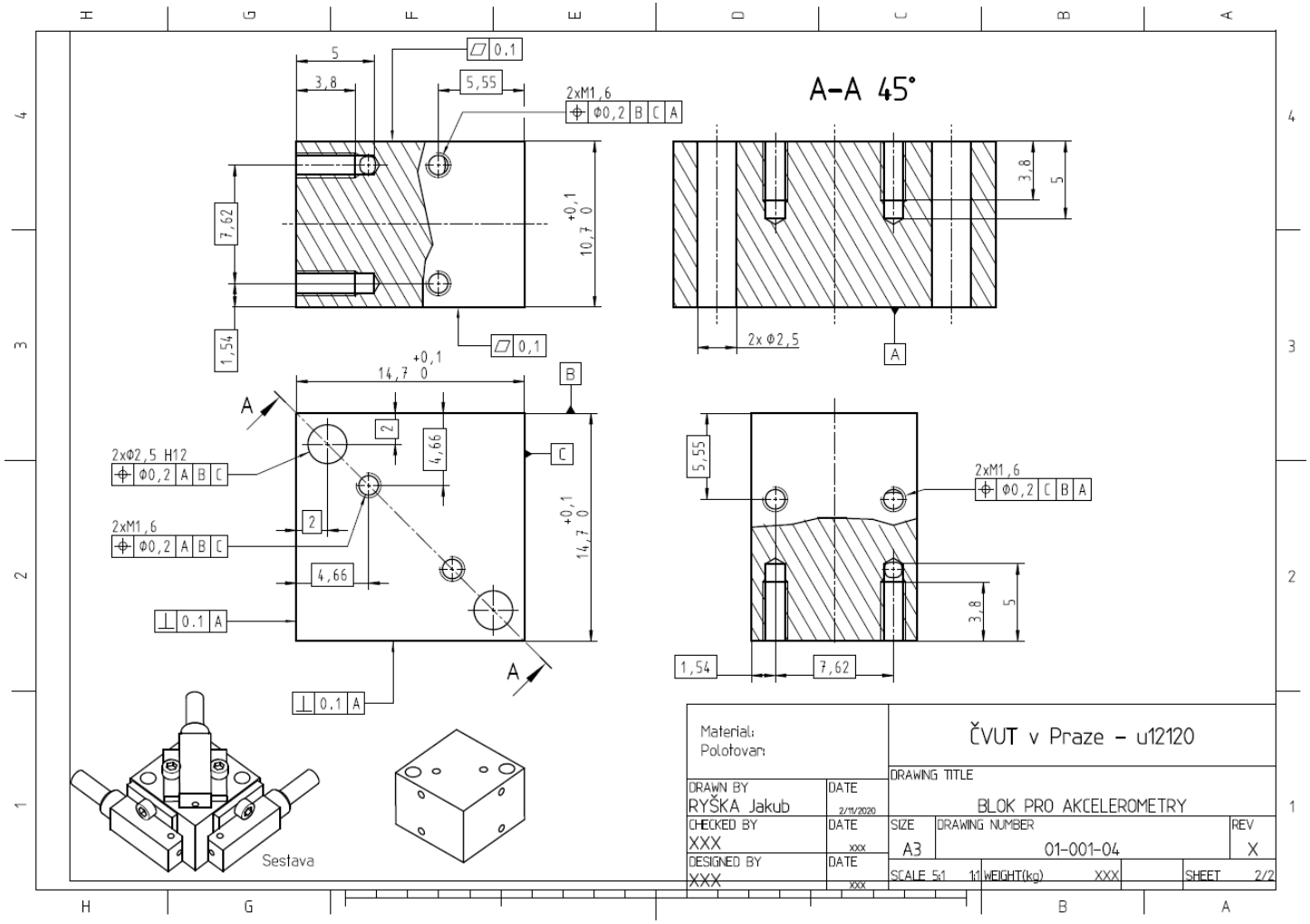

Annex XII – Drawing of the mounting block for accelerometers.

Annex XIII

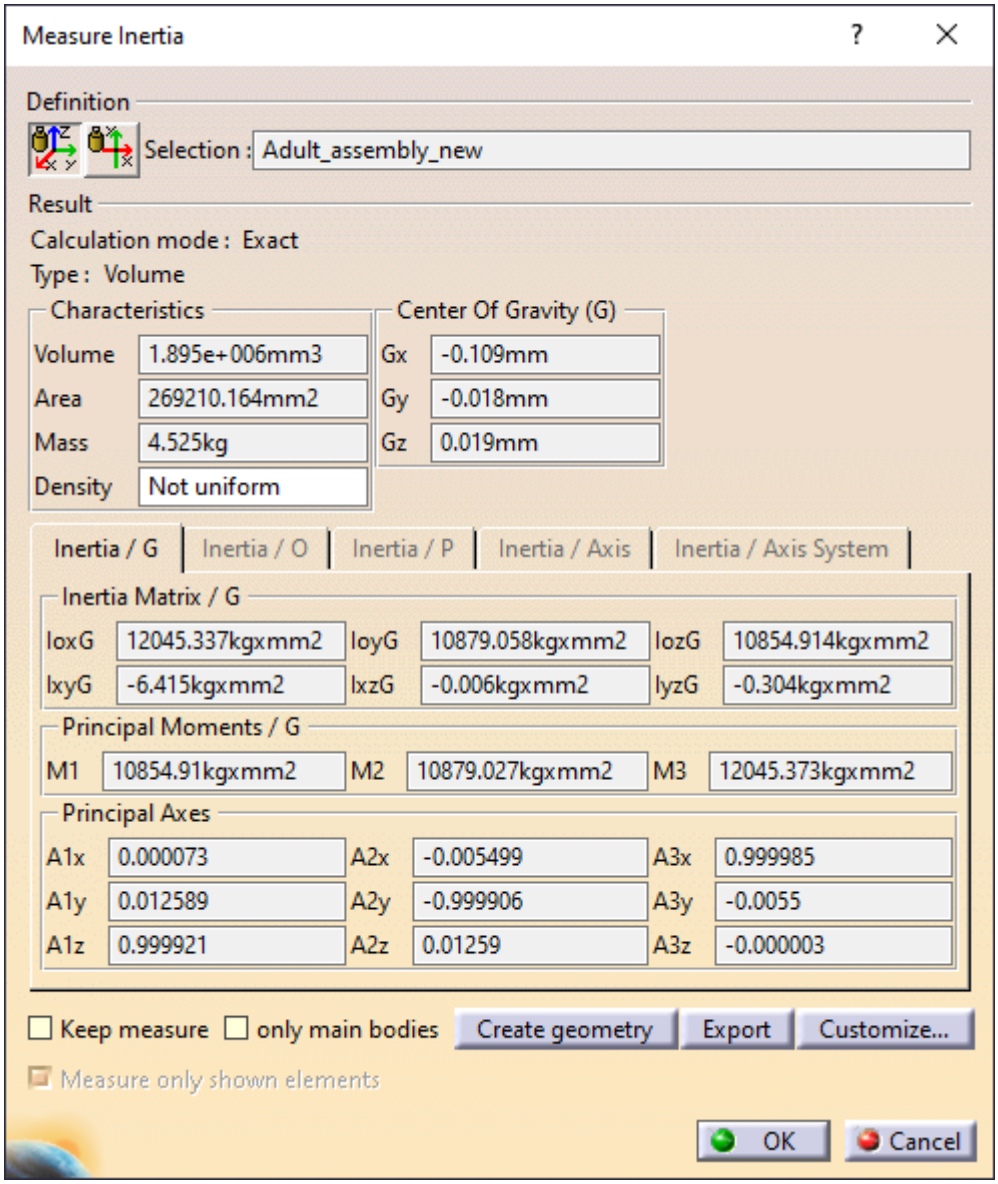

Annex XIII – Mechanical properties of the new adult headform impactor.

Annex XIV

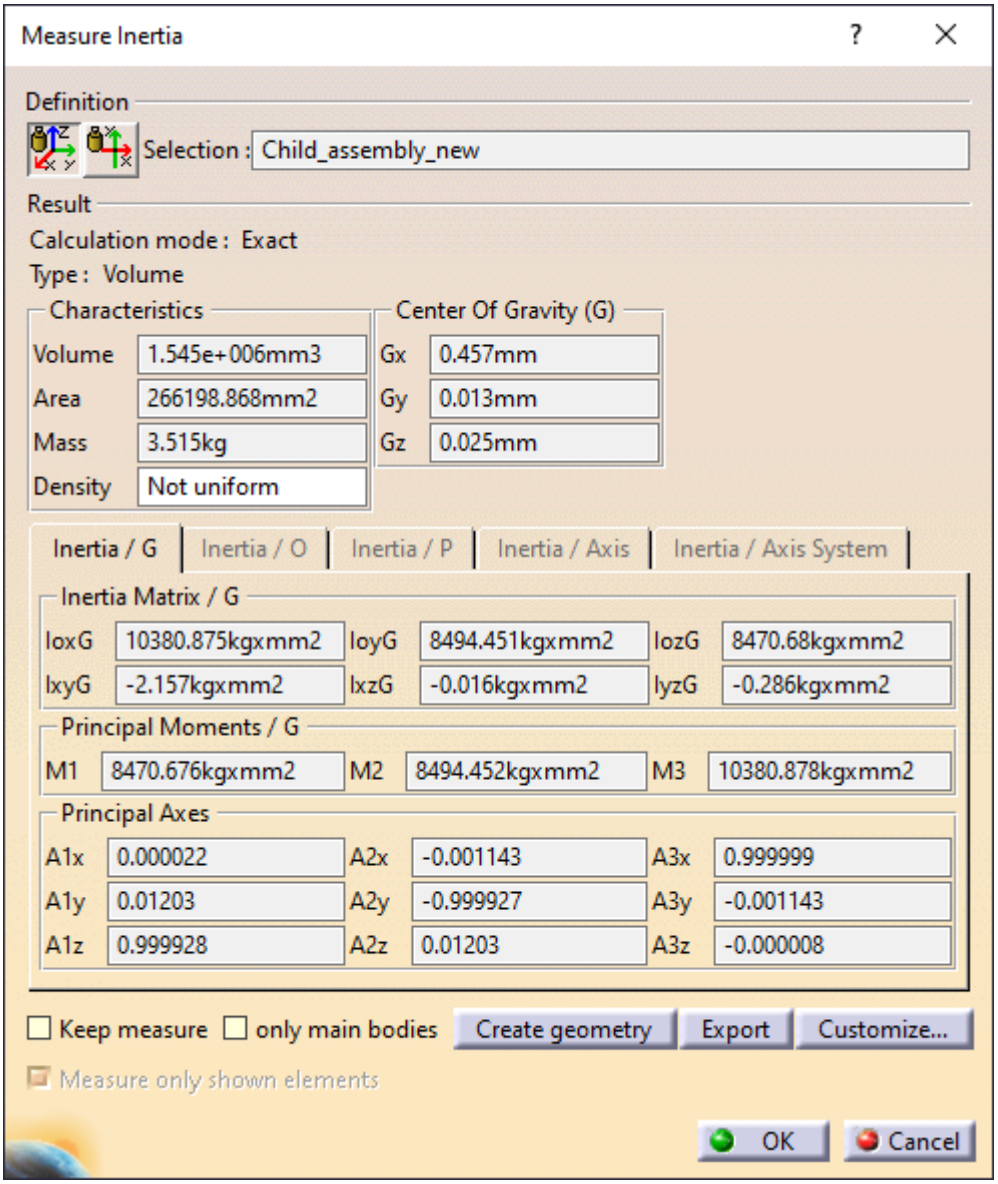

Annex XIV – Mechanical properties of the new child headform impactor.